# MANAGEMENT OF OPTICAL ABSORPTION IN PLASMONIC METAMATERIALS

by

Hossein Alisafaee

A dissertation submitted to the faculty of
The University of North Carolina at Charlotte
in partial fulfillment of the requirements
for the degree of Doctor of Philosophy in
Optical Science and Engineering

Charlotte

2015

Approved by:

Dr. Michael A. Fiddy

Dr. Glenn Boreman

Dr. Greg Gbur

Dr. Marcus Jones

Dr. Ryan Adams

©2015
Hossein Alisafaee
ALL RIGHTS RESERVED

# ABSTRACT

HOSSEIN ALISAFAEE. Management of optical absorption in plasmonic metamaterials leads to more efficient devices at optical and infrared parts of electromagnetic spectrum. (Under the direction of DR. MICHAEL A. FIDDY)

In this dissertation, the main focus has been on the manipulation of optical absorption. That is to either decrease the unwanted losses or increase the desired absorption for specific applications. The approaches have been chosen to provide insightful design of metamaterial structures at optical and near infrared wavelengths. Modeling using equivalent electric circuit theory and numerical simulation using fullwave and scattered wave finite element method are the tools of calculations.

The main focus of low the loss part has been on highly interesting materials in the near infrared such as plasmonic particles of aluminum doped zinc oxide. Solar cells and plasmonic photovoltaics have also been the driving interest to design and optimize the structures for higher efficiency in the next generation of devices.

Successful results have been achieved in the course of this research into plasmonics nanoparticles and also composite nanoantenna-nanowire elements. The results are presented in two different chapters and their sections within. The sections are written to be standalone and provide the reader the flexibility to easily navigate through the basics, methods and results. A list of related publications is available at the end of this document.

# ACKNOWLEDGMENTS

The opportunity to join the doctoral program in optical science and engineering at UNC Charlotte, perhaps has been one of the most important events of my life, which I devoted all my dedication to appreciate the time and support provided with the program by different accomplishments in these few years. During the course of my research at UNC Charlotte, I have been involved with different people who helped me toward the objectives of this dissertation:

First and most of all, I would like to express my deep gratitude for Prof. Michael Fiddy who was the driver and supporter of this research as part of Center for Metamaterial. I had the privilege to meet with him on a routine basis and discuss the details and progress of the work, and learn not only from his immense knowledge and years of experience, but also from his noble personality.

I am also thankful to the committee members, Dr. Glenn Boreman, Dr. Gregg Gbur, Dr. Ryan Adams, and Dr. Marcus Jones for their time and great attitude in reviewing the dissertation material, topic approval and defense meetings.

From the research group of Dr. Fiddy, I was glad to be interacting with nice, smart and hardworking students to exchange comments and discuss the results with them, including Jason Marmon, Daniel Fullager, Max Burnet, Ian Goforth, MyCia Cox, and Christopher Rosenbury. Also, fruitful discussions with Dr. Robert Ingel on the material science aspects of the projects were hugely useful to me.

I had a great support from the members of optics department started long before the first day of my arrival to United States. Dr. Angela Davies, Dr. Faramarz Farahi and

Mark Clayton, they helped me and encouraged me through the early steps of entering the program to the very end. I am very thankful to have them on my side.

My good friends in the department have been also supportive and encouraging in theses yeas: Alexander Bermudez, Mahsa Farsad, Dr. Kenneth Allen, Yangcheng Li, Navid Farahi, Elisa Horwitz, Herminso Villarraga Gomez, Mark Green, Zeba Naqvi, Dr. Mehrdad Abolbashari, and many others.

I would also like to appreciate all the financial support I received including research funding from AFRL and NSF Center for Metamaterial, UNCC Tuition GASP Award, GPSG Travel grants, SPIE travel grants, and OSA travel grant.

Last but not least, I am forever thankful to my parents for their never-ending inspirations.

TABLE OF CONTENTS

# LIST OF FIGURES

# LIST OF TABLES

# CHAPTER 1: INTRODUCTION TO METAMATERIALS AND PLASMONICS

## 1.1. Metamaterials

### 1.1.1. Definition

Metamaterials are manmade artificial structures designed in order to achieve properties not usually found in naturally occurring materials. ‘Meta’ means beyond, and design and fabrication of metamaterials is aimed to obtain responses from the structures which are beyond ordinary case. This response can be in the form of transverse or longitudinal waves, which respectively, are electromagnetic and acoustic waves. In this dissertation, the whole focus is on electromagnetic metamaterials, specifically, in the optical and infrared parts of the spectrum. The response of metamaterials is not only from the intrinsic properties of the materials involved, but also from the shape, size, geometry and orientation of its elements.

### 1.1.2. History

The first appearance of extraordinary (or ‘meta’) response in the materials was the pioneering work of Veselago [1] in 1967, in which he studied the electrodynamics of materials with both permittivity and permeability being negative. He proved that this can lead to propagating waves in a negative index material. Figure 1 shows a demonstration of different properties based on the sign of permittivity and permeability.

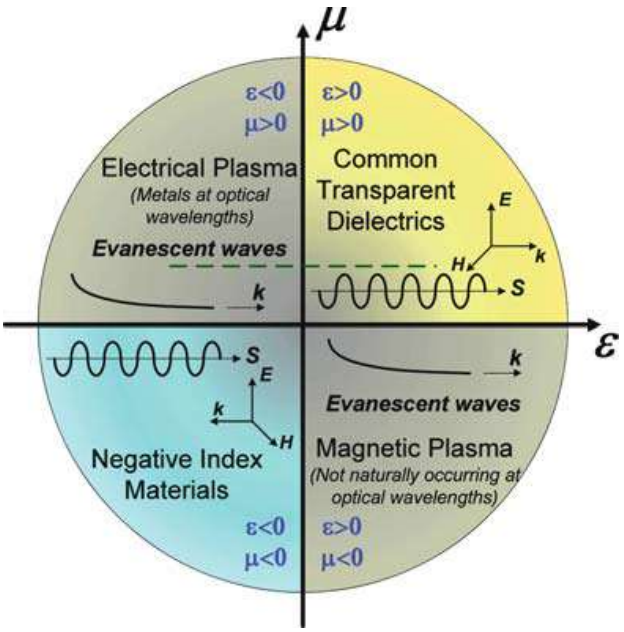


Figure 1: Material properties based on the sign of permittivity and permeability.

### 1.1.3. Applications

There are several properties that can be exploited from the properties of metamaterials. The negative index of refraction was already mentioned. Some of the famous applications of this property include the possibility to achieve superresolution by creating a super lens or a hyper lens.

Another part of the interesting application includes the region with both positive permittivity and permeability but with values close to zero (See Figure 2). This class of metamaterials can be used in many different applications such as ultra-narrow waveguides, or cloaking (Figure 3).

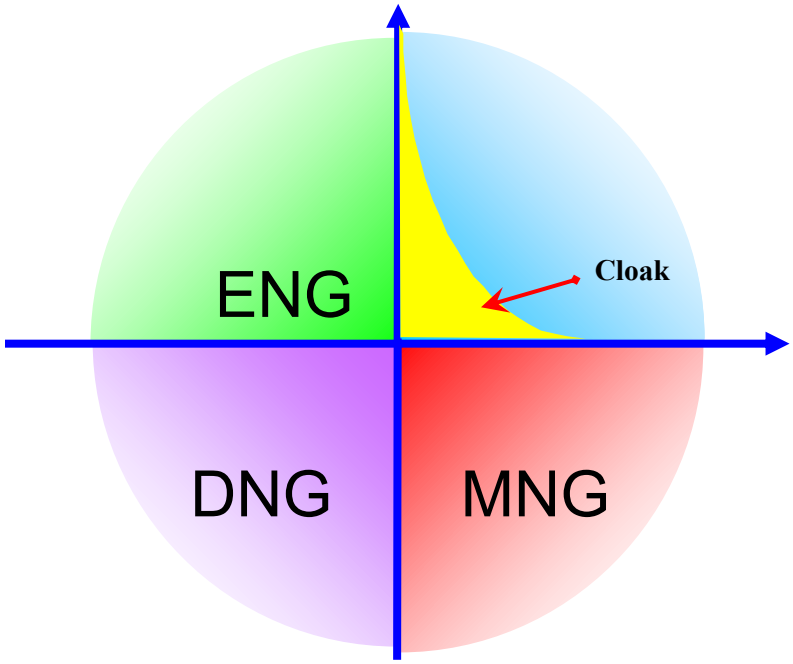


Figure 2: The region of effective cloaking is shown on the chart above with a section of both permittivity and permeability less than unity.

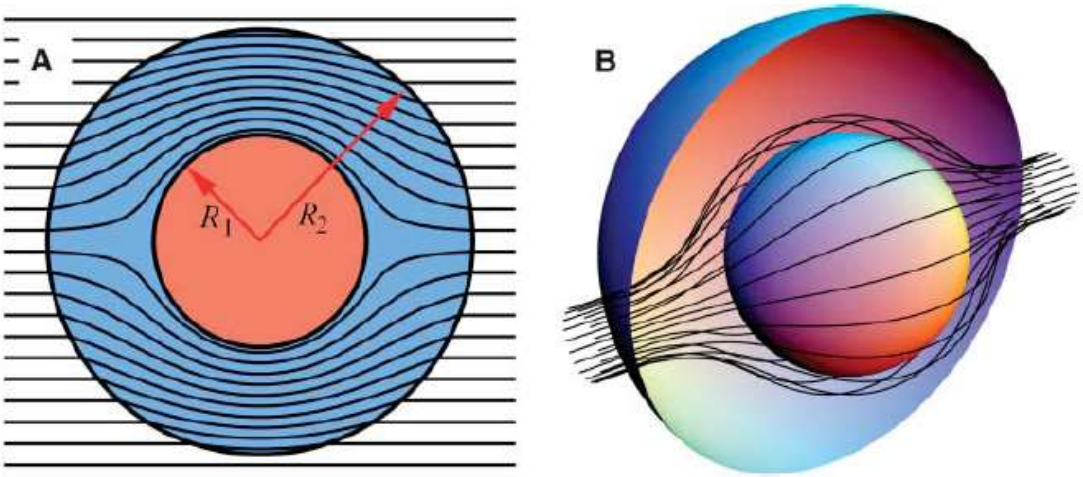


Figure 3: Schematics of cloaking around the object of interest in two and three dimensions.

### 1.1.4. How Does Negative Index of Refraction Work?

The realization of a negative index requires that the material must exhibit both negative permittivity and negative permeability. Negative permittivity can simply be obtained by use of materials with free electrons at frequencies below their plasma

frequency ($\omega_p$). This includes noble metals such as gold and silver. The plasma frequency is defined as:

$$\omega_p^2 = \frac{n_e e^2}{m\varepsilon_0} \ , \tag{1}$$

where $n_e$ is the number density of electrons, $e$ is the electric charge, $m$ is the effective mass of the electron, and $\varepsilon_0$ is the permittivity of free space. Then the permittivity of the material can be obtained by generalized Drude theory:

$$\varepsilon(\omega)' + i\varepsilon(\omega)'' = \varepsilon_{int} - \frac{\omega_p^2}{\omega(\omega + i\Gamma)} \ , \tag{2}$$

where $\Gamma = 1/\tau$, $\tau$ is the mean relaxation time of conduction electrons, and $\varepsilon_{int}$ is a contribution due to interband transitions; it is unity for a perfectly free-electron gas. Some plasma frequencies of various metals are shown in Table 1.

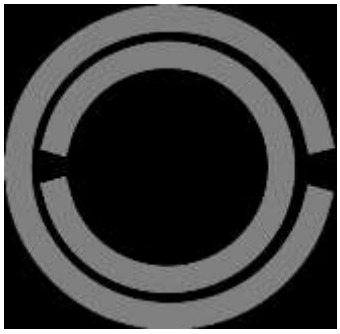

Figure 4: Schematic of Pendry's split ring resonator.

Table 1: Plasma frequency of several metals

| | $\varepsilon_{int}$ | $\omega_p(eV)$ |
|---|---|---|
| Aluminum | 0.7 | 12.7 |
| Copper | 6.7 | 8.7 |
| Gold | 6.9 | 8.9 |
| Silver | 3.7 | 9.2 |

According to Table 1, the permittivity of most of those listed metals is negative in the visible and infrared regions of the electromagnetic spectrum and also at longer wavelengths such as microwave and radio frequencies. The next ingredient to obtain a negative index of refraction is a negative permeability. This was the main requirement to achieve a negative index of refractive until Pendry [2] demonstrated that "microstructures built from nonmagnetic conducting sheets exhibit an effective magnetic permeability, which can be tuned to values not accessible in naturally occurring materials". This was the beginning of the design and fabrication of metamaterials with negative index of refraction. His design solution, called a split ring resonator (SRR), which achieves a magnetic resonance is shown in Figure 4. This design made it possible to combine a wire

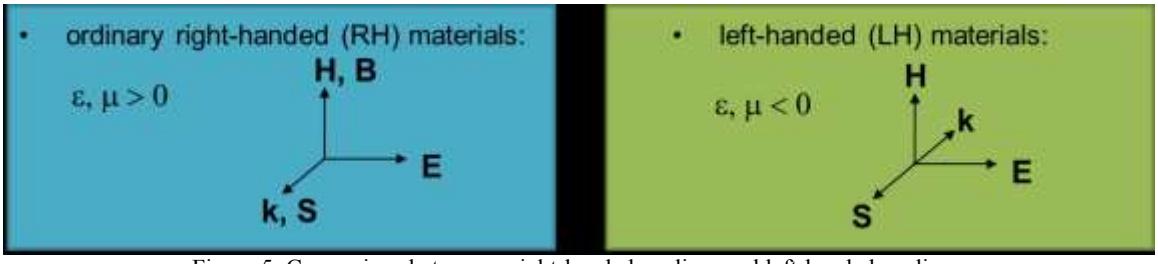


Figure 5: Comparison between a right-handed medium and left-handed medium.

and SRR to both have the permittivity and permeability negative at the same time. This results in a medium with left handed properties in which the pointing vector (***S***) and wavevectors (***k***) are anti-parallel.

When both the permittivity (ε) and permeability (μ) are negative, (for example equal to -1) then the index of refraction can be calculated as shown in (3). Then, based on Snell's law, the refraction angle in such left-handed medium (LHM) will be negative, hence negative refraction occurs (Figure 6).

$$n = \sqrt{\mu\varepsilon} = \left((e^{-j\pi})(e^{-j\pi})\right)^{1/2} = (e^{-j\pi/2})(e^{-j\pi/2}) = e^{-j\pi} = -1. \quad (3)$$

The first experimental verification of the negative index was demonstrated by Smith in 2000 [3,4] at microwave frequency 10.5 GHz and with a refractive index of -2.7 using an array of wires and square SRRs as shown in Figure 7. In each unit or so-called meta-atoms, there is a wire and a SRR, and the whole array is considered the metamaterials structure. The size of the unit cell is much smaller than the wavelength.

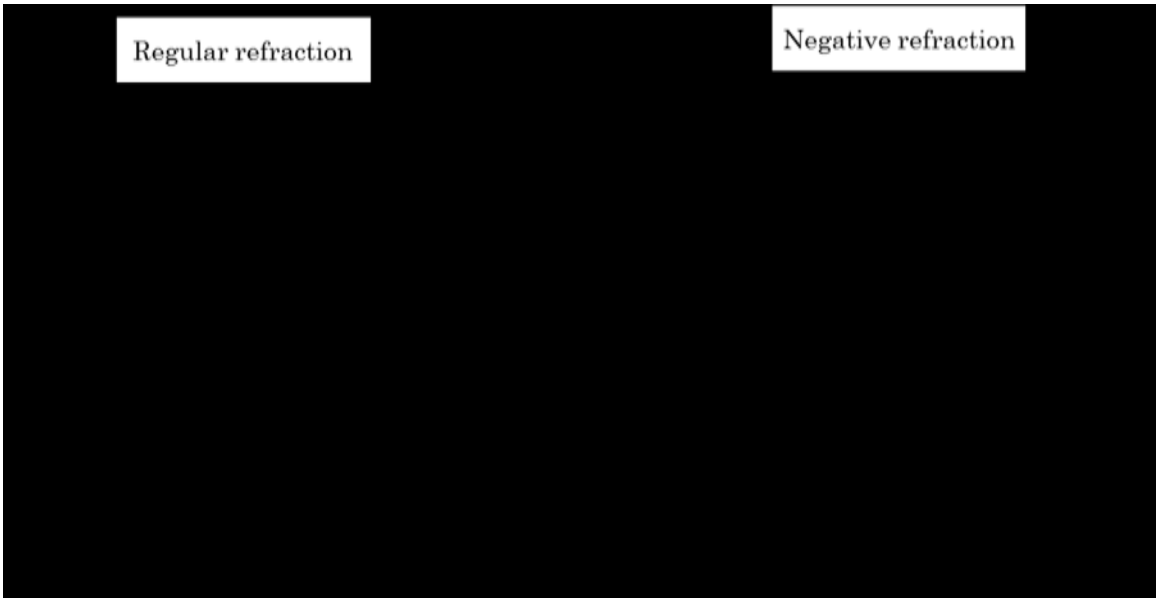


Figure 6: Schematic of positive (regular) and negative refraction in two materials with positive and negative index of refraction.

### 1.1.5. Negative Index or Negative Refraction

As was shown previously, there have been efforts to achieve properties not ordinarily found in nature. One of the properties that can lead to negative refraction is a negative index. It should be emphasized that there is a difference between the two of them. That is, there are other structures that can demonstrate negative refraction through anisotropy or other means, but the structure of a double negative (DNG) metamaterial is such that it provides a resonance point in which the permittivity and permeability are simultaneously negative. It is true that this leads to a negative refraction, but the difference is that for other structures, there could be no simultaneous negative signs for the constituent properties. Actually, they have been also employed later for non-resonant metamaterials

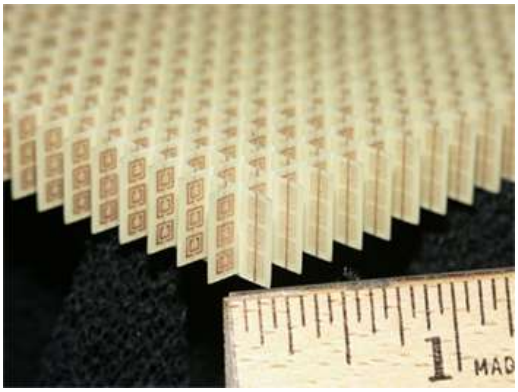

Figure 7: Array of wires and SRRs for microwave frequencies for experimental verification of negative index.

designs, which have some benefits over resonant structures. They will be reviewed later in this dissertation.

## 1.2. Plasmonics

### 1.2.1. Introduction

Plasmonics is the study and application of plasmons. A plasmon is a quantum of plasma oscillation and can be regarded as a quasi-particle since it arises from the quantization of plasma oscillations. In other words, plasmons are collective oscillations of the free electron gas density. When coupled with a photon, plasmons create another quasi-particle called a plasma polariton. The optical properties of metals are affected by plasmons, such that light having frequencies below the plasma frequency is reflected, because the electrons in the metal screen the electric field of the light, and light of frequencies above the plasma frequency is transmitted, because the electrons cannot respond fast enough to screen it. The plasma frequency occurs in the ultraviolet for most metals, which is the reason they shine in the visible range. Copper and gold are exceptions for having electronic interband transitions in the visible range, therefore specific light colors are absorbed, yielding their distinct color. In semiconductors, the

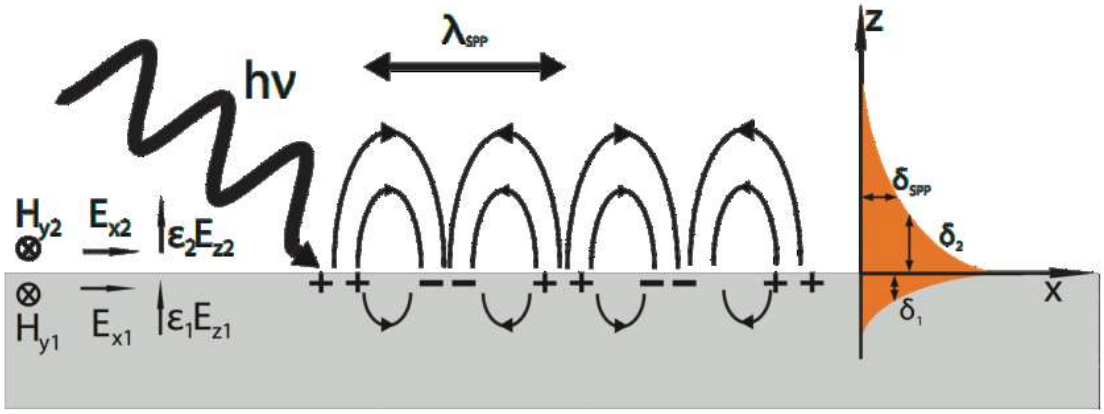


Figure 8: Schematic of surface plasmon polariton excitation

valence electron plasma frequency is in the deep UV which is again why they are reflective.

### 1.2.2. Types of Plasmons

#### 1.2.2.1. Propagating Surface Plasmons

Two most interesting types of plasmons are surface plasmons and localized surface plasmons. Surface plasmons exist at the boundary between two materials with different dielectric function signs, e.g. the surface of a metal exposed to air (Figure 8). They have lower energy than volume plasmons. Surface plasmons were predicted by Rufus Ritchie [5]. These surface plasmons can be excited by photons, which then will be called surface plasmon polaritons (SPP), by use of a prism or grating. To find the excitation condition for SPPs, we consider the electric field of the incident light to be:

$$E = E_0 \exp[i(k_x x + k_z z - \omega t)], \tag{4}$$

where $k$ is the wave number and $\omega$ is the frequency of the wave. The boundary condition and continuity relation imply that:

$$\frac{k_{z1}}{\varepsilon_1} + \frac{k_{z2}}{\varepsilon_2} = 0 \ , \tag{5}$$

and

$$k_x^2 + k_{zi}^2 = \varepsilon_i(\frac{\omega}{c})^2 \ , \qquad i = 1,2 \tag{6}$$

where $c$ is the speed of light in a vacuum, and $k_x$ is same for both media at the interface for a surface wave. The dispersion relation can then be found to be:

$$k_x = \frac{\omega}{c}\left(\frac{\varepsilon_1\varepsilon_2}{\varepsilon_1 + \varepsilon_2}\right)^{\frac{1}{2}} \ . \tag{7}$$

At low k, the SPP behaves like a photon, but as $k$ reaches an asymptotic limit called the "surface plasma frequency", with a shorter wavelength than free-space radiation, then the out-of-plane component of the SPP wavevector is evanescent. The surface plasma frequency is given by:

$$\omega_{SP} = \frac{\omega_P}{\sqrt{(1 + \epsilon_2)}} \ , \tag{8}$$

which for air (ε=1) turns into:

$$\omega_{SP} = \frac{\omega_P}{\sqrt{2}} \ . \tag{9}$$

The SPP propagation length ($L$) is limited due to the absorption in metal and is given by:

$$L = \frac{1}{2k_x^{''}} \ . \tag{10}$$

where $k_x^{''}$ can be calculated from:

$$k_x = k_x^{'} + ik_x^{''} = \left[\frac{\omega}{c}\left(\frac{\varepsilon_1'\varepsilon_2}{\varepsilon_1' + \varepsilon_2}\right)^{\frac{1}{2}}\right] + i\left[\frac{\omega}{c}\left(\frac{\varepsilon_1'\varepsilon_2}{\varepsilon_1' + \varepsilon_2}\right)^{\frac{3}{2}}\frac{\varepsilon_1''}{2(\varepsilon_1')^2}\right] . \tag{11}$$

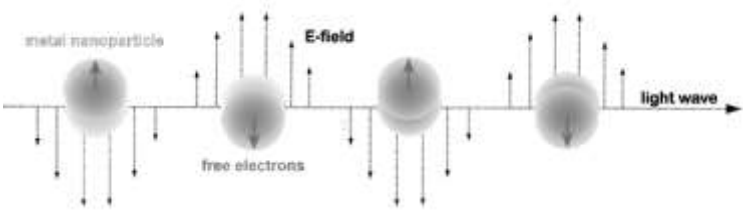


Figure 9: Excitation of localized surface plasmons

#### 1.2.2.2. Localized surface plasmons

When instead of a flat surface, the boundary between the metal and the dielectric is of limited length, such as in a nanoparticle, then the surface plasmons are localized (Figure 9). This is very important and interesting and can benefit from phenomenon since the localization is a very sensitive function of shape, size, material, environment, etc. Surface Enhanced Raman Scattering (SERS) for bio sensing is among the most popular applications for such effect.

# CHAPTER 2: LOW-LOSS LOW INDEX METAMATERIALS

## 2.1. Low-Index Low-Loss Metamaterials of Plasmonic Dimers

Transparent conducting oxides (TCO) are an interesting class of plasmonic materials, which are under intensive study for their use in low-loss metamaterials and a range of applications such as sensing, imaging and transformation optics. In this section, using both the full-wave simulations and an equivalent circuit model for pairs of nanoparticles of aluminum-doped zinc oxide (AZO), the plasmonic effects for low loss low index metamaterials for infrared (IR) applications is studied. The behavior of localized surface plasmon resonances (LSPR) of AZO nanoparticle dimers embedded in a host polymer medium is investigated for different dimer orientations with respect to the incident electromagnetic wave. In doing this, the role of dressed polarizability to enhance and quench the plasmonic effects is also considered. The effects of the nanoparticles relative size and the spacing between them are studied. Understanding these resonances and their dependence on dimer orientations, provides a means to design metamaterials structures for use in the near infrared (NIR) region with epsilon-near-zero (ENZ) properties leading also to low index metamaterials.

In the following, we demonstrate how nanospheres with radii less than 100 nm that are distributed with an average spacing less than their diameter, can result in an effective medium with a refractive index less than one. A full-wave frequency domain finite element method (FEM) in conjunction with an equivalent-circuit model for the nanoscale

dimers in order to describe the spectral response of the bulk low index properties is utilized.

As mentioned in Chapter 1, metamaterials are artificial structures designed and used in various regions of the electromagnetic spectrum from microwave to optical frequencies. Why they constitute an exciting area of research is their promising and exotic list of applications such as negative index [14-17] for super- and hyper-lenses [18,19], invisibility cloaking [20,21], giant chirality [22,23], etc.

A particular class of metamaterials we discuss here are structures with epsilon-near-zero[24,25] (ENZ), or low refractive-index properties, which can squeeze electromagnetic waves into ultra-narrow ENZ channels [26], shape the phase pattern of radiation sources [27], control leaky wave radiation in ENZ waveguides [28], and etc. At a desired wavelength in the optical or IR range, ENZ metamaterials can be synthesized by embedding suitable inclusions, such as metals, in a host medium [29].

Metallic particles exhibit localized surface plasmon resonances (LSPR) [30] which are dependent on size, shape, material and host medium of the particles [31]. At the high frequencies of optical and infrared light, the interband electronic transitions of metals cause attenuation of light [32], which degrades the performance of the plasmonic system for application purposes. A method to compensate for this loss is the use of a gain medium as a host material [33]. However, in the case of metals, the losses are large compared to the available gain. Also for plasmonic applications of metals at infrared frequencies, there is a need for host dielectric materials with high permittivity to satisfy

the requirement of the resonance condition. Therefore, alternative plasmonic materials such as transparent conducting oxides have been proposed [34-36].

Transparent conducting oxides (TCO), such as aluminum doped zinc oxide (AZO) or gallium zinc oxide (GZO), are an interesting class of plasmonic materials, as opposed to metals, which are under intensive study for their use in low-loss metamaterials and a range of applications such as sensing, imaging and transformation optics [37]. Due to their content of free electrons, metallic and TCO nanoparticles can exhibit LSPR, provided that the condition of the resonance is met. It is also demonstrated that the doping of TCOs can be high enough to resemble a metal-like optical properties at NIR frequencies [38]. Among TCOs, AZO is a material with low loss at NIR wavelengths. Nanoparticles of AZO are commercially available and usually used in optoelectronics applications such as in solar cell panels. It is possible to use nanospheres of AZO for making a low-loss low-index metamaterial by embedding them in a suitable host medium via a chemical or physical deposition method or also with self-assembly approaches. To obtain the recipe for fabrication, i.e. the particle's size and spacing, one needs to first design and model the response of such structures.

Here, the design of a low-loss low-index metamaterial structure made of dimers of AZO for IR wavelengths is investigated. That is, a metamaterial structure made of coupled nanospheres of AZO is considered. Then using the LCR method, the properties of coupled AZO particles upon changes in orientation toward light polarization and also interparticle spacing is studied. Further, a full-wave approach will be used to look into the

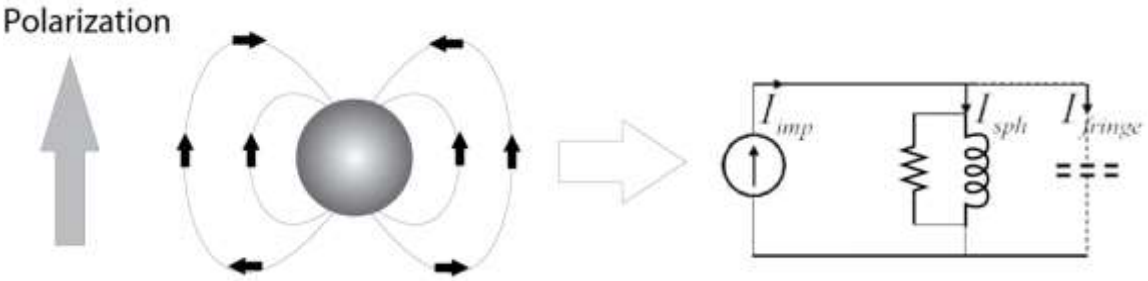


Figure 10: A plasmonic nanosphere with ε <0 , which is equivalent to a nanoinductor and a nanoresistor. Black arrows are representative of fringe dipolar field, and the grey arrow is the polarization direction of incident light. On the right is the equivalent nanocircuit of this plasmonic particle.

electromagnetic behavior of the system. Finally, the bulk properties of the designed structure are retrieved and compared with that of usual effective medium approaches.

### 2.1.1. LCR Approach

In the quasi-static approximation, where the particle size is much smaller than the wavelength of light, it is demonstrated that one can consider the interaction of nanoparticles with light as the response of lumped circuit elements [7]. Depending on the sign of the material's permittivity, the response can be inductive (for negative sign), or capacitive (for positive sign). In both cases, a resistive response can also be considered for the imaginary part of the permittivity. There is then the displacement current that takes the role of electric current in such equivalent circuits, having this unique property that it is no longer confined to conducting wires, but, instead, it flows in the whole space. Except in some specific cases [41], this results in simultaneous parallel and series configurations [42,43], which can open new design approaches, or, in contrast, can limit the prediction of usual designs [44].

The equivalent circuit of a conductive nanoparticle is shown in Figure 10. The circuit is basically comprised of an impressed current generator ($I_{imp}$, Eq.(12)), nanoparticle impedance ($Z_{nano}$ Eq. (13)), and a parallel fringe capacitance of impedance $Z_{fringe}$ (Eq.

(14)) due to the dipolar field, which are described in association with the particle properties. We can find the equivalent voltage as in Eq. (15), which will be on resonance when $\varepsilon = -\varepsilon_0$. The resonance seems to be independent of particle radius ($R$), which is not what happens in reality.

At resonance, the response can be considered to be independent of the particle's radius, too. Corresponding equivalent circuit elements including nanoinductor, nanocapacitor, and nanoresistor can be obtained from Eqs. (16) - (18), with equivalent resistivity $\rho = G^{-1}$.

$$I_{imp} = -i\omega(\varepsilon - \varepsilon_0)\pi R^2 |E_0| \tag{12}$$

$$Z_{nano} = (-i\omega\varepsilon\pi R)^{-1} \tag{13}$$

$$Z_{fringe} = (-i\omega\varepsilon_0 2\pi R)^{-1} \tag{14}$$

$$V = \frac{\varepsilon - \varepsilon_0}{\varepsilon + 2\varepsilon_0} R|E_0| \tag{15}$$

$$L_{sph} = (-\omega^2 \pi R \,\mathrm{Re}|\varepsilon|\,)^{-1} \tag{16}$$

$$C_{sph} = 2\pi R\varepsilon_0 \tag{17}$$

$$G_{sph} = \pi\omega R \mathrm{Im}[\varepsilon] \tag{18}$$

When two nanoparticles are interacting, their overlapping fringe fields change and there will be additional induced dipoles in each particle. The equivalent circuit then needs modification, assuming no higher order resonances are present in the system. Here, we just mention the final results, and the interested reader is referred to the original paper [45] for a detailed discussion. To include the coupling effect between the particles, one

needs to add dependent current sources in the circuit equivalent with a current expression of:

$$I_{12(21),dipolar} = -i\omega\pi\left|E_{12(21)}\right|\left(\varepsilon_{1(2)} - \varepsilon_0\right)R_{1(2)}^2, \tag{19}$$

$E_{12(21)}$ is the field originated from the second (first) sphere, evaluated at the center of the first (second) sphere. They are defined as:

$$\begin{pmatrix} E_{12} \\ E_{21} \end{pmatrix} = \begin{pmatrix} |d|^3\bar{I} & -\gamma_2(3\bar{D} - \bar{I}) \\ \gamma_1(3\bar{D} - \bar{I}) & |d|^3\bar{I} \end{pmatrix}^{-1} \begin{pmatrix} \gamma_2(3\bar{D} - \bar{I})E_0 \\ \gamma_{-1}(3\bar{D} - \bar{I})E_0 \end{pmatrix}, \tag{20}$$

where:

$$\bar{D} = \frac{d}{\bar{d}}\ \frac{d}{\bar{d}}, \tag{21}$$

$$\bar{I} = \begin{pmatrix} 1 & 0 & 0 \\ 0 & 1 & 0 \\ 0 & 0 & 1 \end{pmatrix}, \tag{22}$$

$$\gamma_i = \frac{\varepsilon_i - \varepsilon_0}{\varepsilon_i + 2\varepsilon_0} R_i^3. \tag{23}$$

$\bar{D}$ is the vector that locates the generic position of the second sphere. This equation is completely general for any arbitrary orientation of $E_0$ and $d$. There are, however, two simplified cases as shown in Figure 11; 1) the axis of the dimer is parallel to the polarization direction of the incident light Eqs. (24), 2) the axis is perpendicular to the polarization Eqs. (25).

$$\begin{cases} E_{12} = \dfrac{2\gamma_2(d^3 + 2\gamma_1)}{d^6 - 4\gamma_1\,\gamma_2}\,E_0 \\ E_{21} = \dfrac{2\gamma_1(d^3 + 2\gamma_2)}{d^6 - 4\gamma_1\,\gamma_2}\,E_0 \end{cases} \tag{24}$$

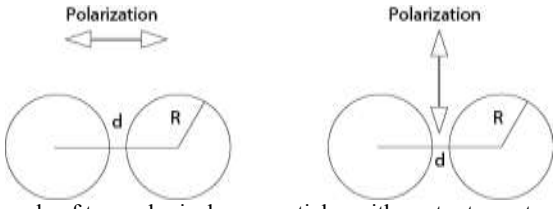


Figure 11: Dimer system made of two spherical nanoparticles with center to center separation of 2R + d. The orientation of dimer axis to the polarization of light is parallel (left), and perpendicular (right).

$$\begin{cases} E_{12} = \dfrac{2\gamma_2(\gamma_1 - d^3)}{d^6 - \gamma_1\,\gamma_2}\,E_0 \\ E_{21} = \dfrac{2\gamma_1(\gamma_2 - d^3)}{d^6 - \gamma_1\,\gamma_2}\,E_0 \end{cases} \tag{25}$$

In the next section, we begin the analysis of particles' interactions and coupling in the dimer structure by evaluating the last two equations.

### 2.1.2. Results and Discussion

As mentioned in previous section, the induced dipoles on each sphere are dependent on the field passing through it. The coupling between the particles is dependent on the separation ($d$), radius ($R$) and $\gamma$ parameter which includes the permittivity values of the particle and the host medium. We studied the two cases of parallel and perpendicular orientation of the dimer axis by evaluation of their corresponding secondary fields ($E_{12}$ and $E_{21}$), which are related to the voltage controlled dependent source (see Eq. (20)). The nanoparticles are considered with a spherical shape and identical radii in each dimer. Their material is assumed to be AZO. The host medium is air. Since the frequency dependence of the material's permittivity is not included in Eq. (20), it is necessary to study these changes directly by manually varying the value of $\varepsilon$. Moreover, due to the variation of the materials' loss (ascribed to the imaginary part of $\varepsilon$) over the frequency range, different cases of loss are also considered in the calculations. We study the effects of dimer separation on the secondary fields. The maximum separation is assumed to be as

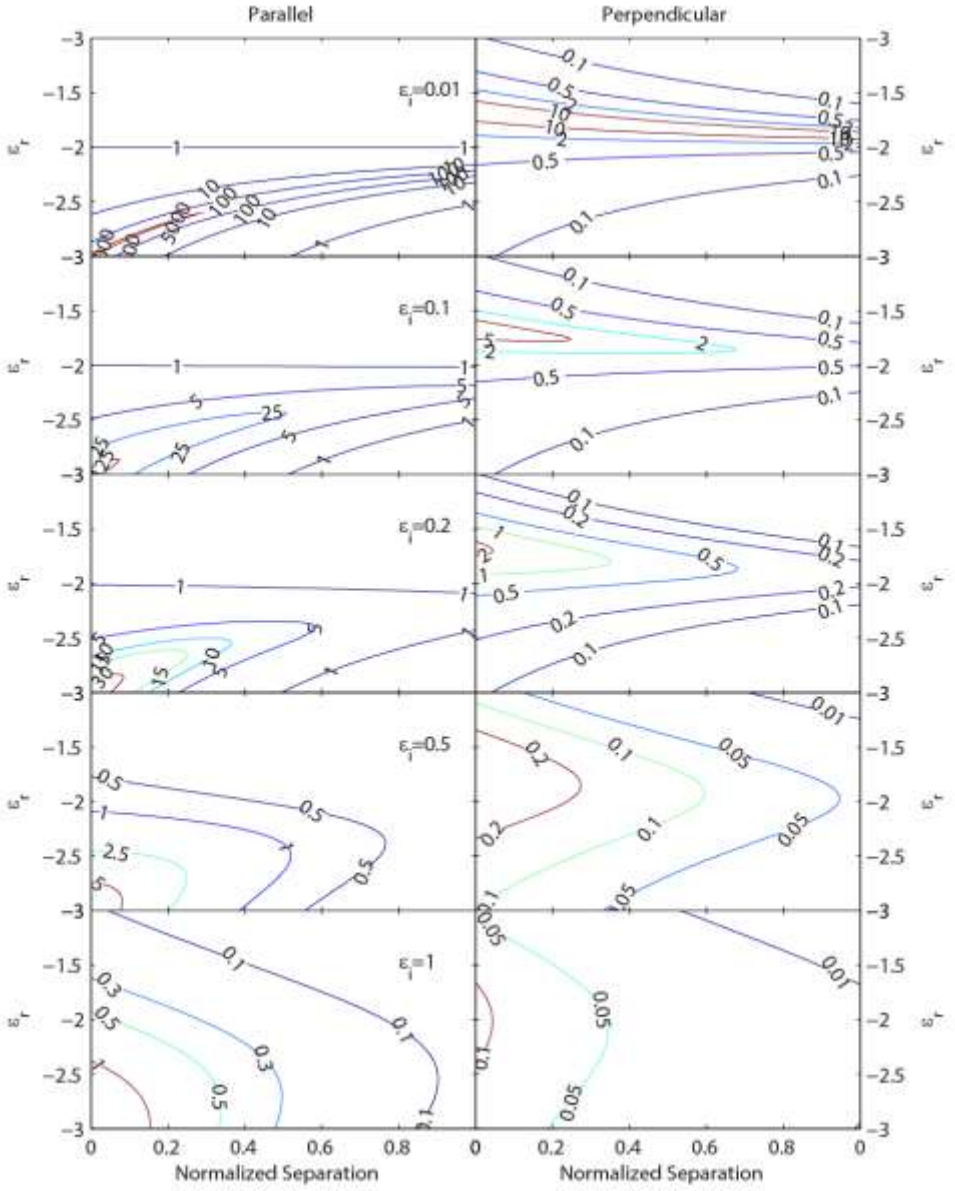


Figure 12: Contour plots of $|E|^2$ for parallel (left column) and perpendicular (right column) orientations of dimers. The $|E|^2$ is calculated as the distance between two spheres is changing from 0, the touching limit, to 1, in units of R. The vertical axis accounts for changes of real part of permittivity ($\varepsilon_r$) due to spectral response of nanoparticles. Also, each row from top to bottom adds to the loss term, represented by imaginary part of permittivity ($\varepsilon_i$).

large as a radius of the particle, and the minimum separation is zero. The results of our study are shown in Figure 12.

Having analyzed the behavior of contours shown in Figure 12, important aspects of the results can be found as follows. Figure 12 (left/ right) shows the values $|E|^2$ for parallel/perpendicular orientation. The resonances in each orientation have different magnitudes and also different properties along the vertical axis which is the real part of the permittivity. That is, the parallel dimer has a pronounced resonance compared to the perpendicular case, which, in general, is more than one order of magnitude. However, it can be observed that for the case of perpendicular orientation, the resonance band is extended to be almost constant over a wide range of separations, while the resonance seems more localized at smaller separation values for the parallel case. But, it should be noted that the resonance magnitude for the parallel case is larger than the case of perpendicular one even when the dimer separation is very large. Another point to be made is the location of the resonance in the parallel case, happens at ε values smaller than those of perpendicular case. We need to recall that the resonance for a lossless material occurs when $\varepsilon = -2\varepsilon_0$. These changes in the location of the resonances can be translated to red-shift and blue-shift of LSPR due to coupling in parallel and perpendicular cases, respectively. The last result from the plots in Figure 12 can be thought of as the obvious broadening in the resonance with increase of the losses. It is also observable that as the losses are higher, the peak value of the resonance degrades severely, hence the Q-factor of the dimer structure decreases significantly.

These studies, which are based on classical electrodynamics, show enhanced field localization as the separation approaches to zero. However, we need to point out that there are other studies based on quantum approaches demonstrating different results

when the separation is close to zero [46]. We have neglected the latter type of study because the particle proximity we are going to study in this work is larger than the limits of the mentioned quantum approach.

Comparing the magnitude of parallel and perpendicular resonances in Figure 12 implies that we can safely neglect the perpendicular orientation coupling and only consider the parallel one for further calculation of bulk properties.

This occurs because of the role of dressed polarizability, which is defined as the ratio between the enhanced dipole moment and the incident field. That is, for the parallel orientation, we have an enhanced dipolar response, while for perpendicular orientation the dipolar response is quenched (recent analytical treatment of dressed polarizability for dimer structures can be found in the literature [47]). Thus, we can assume a bulk structure composed of dimers with their axes parallel to the polarization of light. That is, we are now able to decompose a structure made from random embedding of nanospheres into a dimer based structure for computation of its bulk properties.

This follows because we can consider every two nanospheres with a separation less than their diameter as a dimer parallel to the light's linear polarization, which is schematically illustrated in Figure 13.

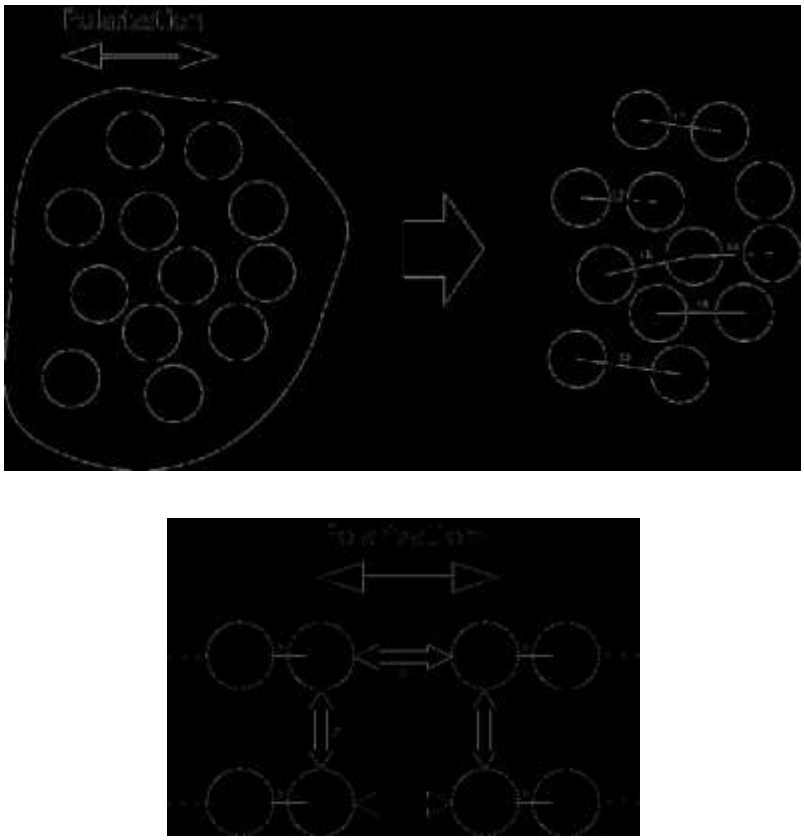

Figure 13: Decomposition of a random placement of nanoparticles into dimers with parallel axis to the polarization of light. The dimers have various separations due to randomness of the structure. At the bottom, the randomly positioned dimers are arranged into an ordered array structure for ease of computations.

To calculate of bulk properties, we need to consider arrays of such dimers and take into account the interparticle coupling. However, since the adjacent spacings between dimers are again somewhat random, it is then necessary to study each case separately and then take the average of all the individual arrangements. Figure 14 (left panel) shows the main framework to study different arrangements with a fixed radius of 50nm for AZO nanospheres. It can be seen that as the lateral separation in the y direction ($\Delta y$) decreases, there is a blueshift in the response of the metamaterial structure. This is consistent with the results of LCR approach. Moreover, since we need to examine the effect of dispersion in radius on the bulk optical constants, a similar study of arrays but with different radii

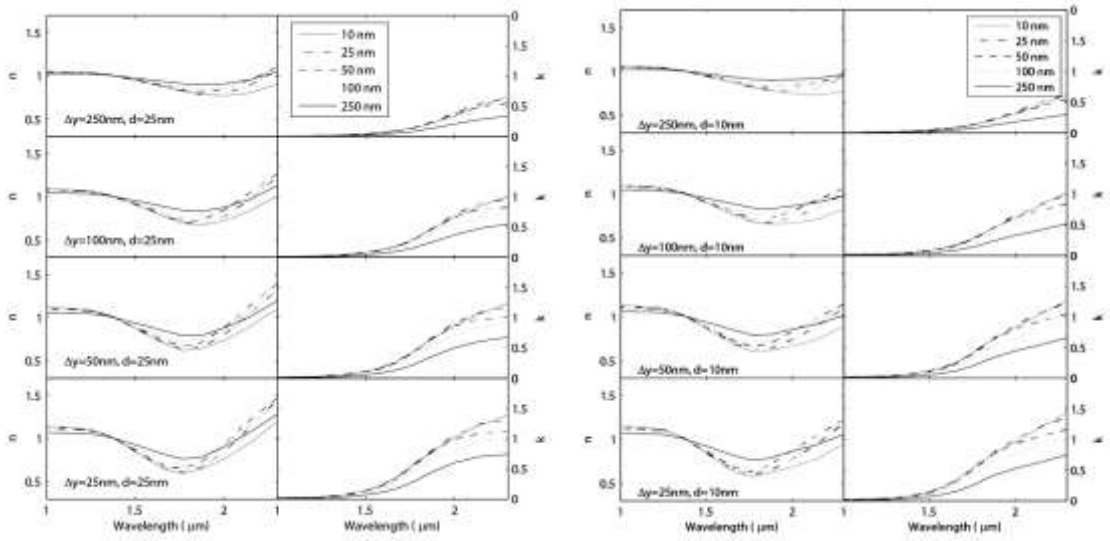


Figure 14: (left) Plots of optical constants retrieved for array of dimers with fixed separation (d = 10 nm) but variable inter-dimer distance in x and y directions. The radius of all nanospheres is R = 50 nm. (right) Retrieved n and k for dimers with different radius and fixed separation.

has been carried out, with the results shown in the right panel of Figure 14. Furthermore, we considered three different dimer separations (*d*) of 5nm, 10nm and 25nm to take into consideration most of the randomness in the final fabricated metamaterial layer. For each case, the lateral spacing in *x* and *y* directions, Δx and Δy, respectively, are variables in the range of 10nm to 250nm. The resulting plots (Figure 15) are representative averaged optical constants for a random structure made from dimers having certain separations.

Regarding simple effective medium theories (EMT) to calculate the permittivity of bulk structure, it is possible to use the Bruggeman mixing rule for getting an idea of what could be predicted. The main factor in determining the effective permittivity of such metamaterial structures is the filling factor (*f*). In our study, the maximum filling factor is about 1/2 for Δx = 0 and Δy = 0. If we use the Bruggeman mixing rule (Eq.(26)), with $f_1 = f_2 = 1/2$, which is the maximum packing density, then the lowest 'effective' refractive index would be $n$=0.8, $k$= 0.65 at 2μm.

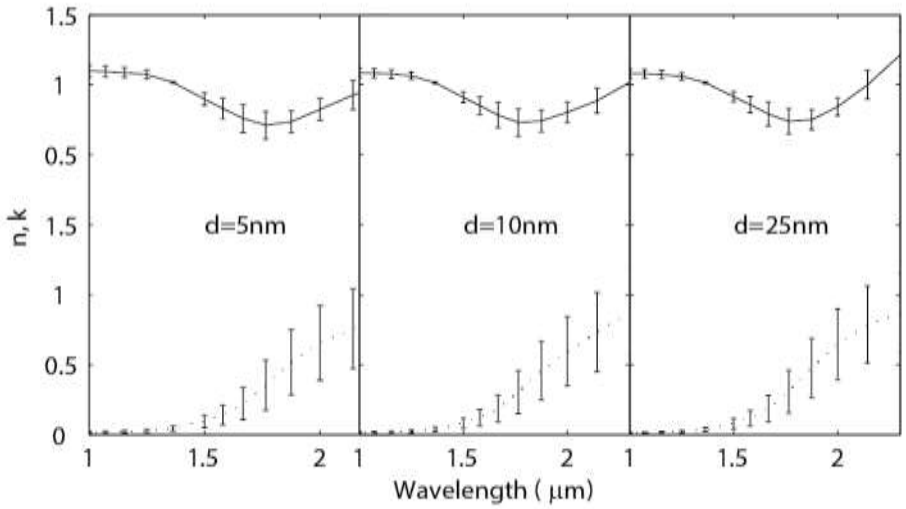


Figure 15: Retrieved optical constants (*n,k*) for the dimer arrays having three different separations 5nm, 10nm, 25nm. Each plot is obtained by averaging optical constants retrieved from an array of dimers with varying separation between its dimers in x and y directions.

$$\varepsilon = \frac{1}{4}\Big\{(3f_1 - 1)\varepsilon + (3f_2 - 1)\varepsilon_0 \pm \sqrt{[(3f_1 - 1)\varepsilon + (3f_2 - 1)\varepsilon_0]^2 + 8\varepsilon\varepsilon_0}\Big\} \tag{26}$$

If we define the figure of merit (FOM) for low-index metamaterials as $1/nk$, we find FOM = 1.9 from Bruggeman EMT. However, as we have seen from rigorous full-wave simulations, the optical constants of the dimer structure can provide much better FOM such as a value of 4 for the case with $\Delta x = 25nm$, $\Delta y = 25nm$. This not only is more than twice the value predicted from EMT, but also the occurrence of the lowest index wavelength is blue-shifted. The reason behind such a difference is most likely due to the plasmonic effects that are ignored in the Bruggeman formula. This means that the approach we used for achieving the spectral response of such low-index metamaterial structures is more accurate compared to conventional methods.

For fabrication of such metamaterial structures, self-assembly approaches can be used in which nanoparticles of AZO are coated with several types of organic ligands; oleic acid, hexadecylamine (HDA), dodecanethiol (DDT) and octadecylamine (ODA). The -SH,-NH2, and COOH functional groups of these ligands are expected to adsorb onto the surface of the AZO nanoparticles. The ligands surrounding the nanoparticles would allow for the adequate spacing between nanoparticles which would create the desired scattering phenomenon.

In summary, a low-loss low-index metamaterial structure comprised of dimers of AZO for use at NIR wavelengths has been studied. The effects of dimer separation, radius, and dimer arrangement are studied with the help of equivalent circuit theory and also fullwave simulations. We obtained an average low-index band with acceptable values of figure of merit, defined in the paper. We demonstrated that the localized plasmonic effects of AZO nanoparticles have important effects on determining and distinguishing the effective bulk optical constants compared to conventional averaging methods.

## 2.2. Polarization Insensitivity in Epsilon-Near-Zero Metamaterial from Plasmonic Aluminum-Doped Zinc Oxide Nanoparticles

In this section, we investigate the optical characteristics and polarization insensitivity of an ENZ metamaterial structure comprising AZO nanoparticles (NPs) hosted by a medium of ligands. By the use of an equivalent circuit model for the pairs of NPs, or dimers, and also of fullwave simulations, we studied the response of this self-assembled metamaterial for near-infrared applications. Considering the coupling of localized surface plasmons, we demonstrated the dominance of a certain dimer configuration and then applied this result to the whole medium as a simplifying approximation for a random

structure. The subsequent results showed polarization insensitivity and also a general redshift in the plasmon resonance of the structure.

### 2.2.1. Introduction

As previously discussed, metamaterials [14-19] are artificially designed structures having their building blocks smaller, usually by a factor of 5 to 10, than the operational wavelength ($\lambda_0$). Therefore, the size dependence of the optical and spectral properties of such structures are distant from those of the photonic crystals (size $\approx \lambda_0$) or of the effective media (size $\ll \lambda_0$). Their properties can be engineered to differ from ordinary materials found in nature. For example, a negative index of refraction [15,16] has been predicted and demonstrated experimentally, with potential applications as super- and hyper-lens [17-19]. Epsilon-near-zero (ENZ) [24,25] metamaterials are among the most interesting classes of artificial structures which constitute an exciting area of research with promising and exotic applications. They can be exploited to squeeze electromagnetic waves into ultra-narrow ENZ channels [26], to shape the phase pattern of radiation sources [27], to control leaky wave radiation in ENZ waveguides [28], etc. The majority of the ENZ metamaterials are anisotropic and their response changes with polarization of the incident light. This is mainly due to the physical and chemical fabrication methods for highly ordered structures, and which are subject to our design approaches. Therefore, a flexible design leading to a choice of simpler fabrication procedures is always preferable since it will be cost effective. According to this, we investigate the design of self-assembled ENZ metamaterials, and show theoretically that this method of fabrication can provide interesting optical properties such as polarization insensitivity. The results could

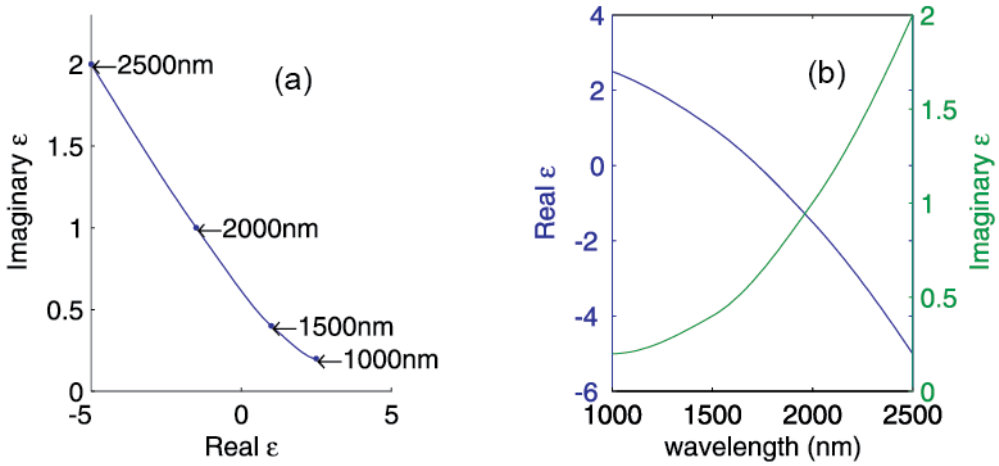


Figure 16: The mapped dielectric function (a) and the spectra (b) of an aluminum-doped zinc oxide (AZO) thin film with 3.0 wt% Al (Ref. 37).

be significantly useful in deciding on the method of fabrication, and also to shed light on the optical behavior of random plasmonic structures.

Since ENZ metamaterials can be synthesized by embedding suitable inclusions in a host medium [29], we employ plasmonic NPs of AZO as a suitable candidate, for the sake of many interesting applications at NIR wavelengths [34-36]. AZO NPs provide localized surface plasmon resonances (LSPRs) that can be incorporated into the metamaterial's response to significantly increase the effectiveness of light-matter interactions. For the self-assembly of such a metamaterial, NPs of AZO can be coated with several types of organic ligands such as oleic acid, hexadecylamine, dodecanethiol, and octadecylamine. The −SH, −NH2, and COOH functional groups of these ligands are expected to adsorb onto the surface of the AZO NPs. The surrounding ligands ensure adequate spacing between NPs, and form the host medium as well.

### 2.2.2. Methods and Results

We use a lumped circuit model [7,45] to approximate the complex interactions of NPs in a random self-assembled structure. Each plasmonic NP can then be modeled by an inductor, a resistor, and a capacitor. We simplify the complicated structure into building blocks made from particle pairs, or dimers. Each dimer is composed of two spherical NPs of the same radius ($R$) and a center-to center spacing $d$. The axis connecting the centers of two NPs in a dimer defines its orientation. The internal interactions with each NP of the dimer are modeled by adding a voltage controlled current source to the circuit, which is proportional to the induced field from the other NP. In the two extreme cases, where the dimer is oriented parallel or perpendicular to the polarization of the incident light, the induced fields are [45]:

$$E^{\perp}{}_{12(21)} = \frac{2\gamma_{2(1)}\left(d^3 + 2\gamma_{1(2)}\right)}{d^6 - 4\gamma_1\,\gamma_2}\,E_0 \tag{27}$$

$$E^{||}{}_{12(21)} = \frac{\gamma_{2(1)}\left(\gamma_{1(2)} - d^3\right)}{d^6 - \gamma_1\,\gamma_2}\,E_0 \tag{28}$$

where $E_{12(21)}$ is the field originated from the second (first) sphere, evaluated at the center of the first (second) sphere, $\gamma_i = \frac{\varepsilon_i - \varepsilon_0}{\varepsilon_i + 2\varepsilon_0} R_i^3$, $\varepsilon_i$ and $\varepsilon_h$ are the permittivity of the inclusions (AZO here) and the host medium, respectively. We ignore the effects of substrate, if one is present or required.

The model exploits a quasi-static approximation, assuming a particle size much smaller than the wavelength. Thus, it ignores any retardation effects and frequency dependence. To compensate for the latter, we have mapped the wavelength range onto the permittivity

of the AZO (Figure 16), as there is a one to one equivalent value of permittivity for every wavelength of interest. We calculate the fields using Eqs.(27)-(28) and vary the spacing between the NPs, *d*, and show the mapped permittivity results in Figure 17, for both parallel and perpendicular orientations. The plots show a few interesting facts. They show the shifts of spectral features to the blue or red with respect to an isolated NP represented by the horizontal line (also in Figure 18) when the dimer is oriented perpendicular or parallel, respectively. One can also find the shift of spectral peak to the case of isolated NPs (no coupling) when the spacing is increased enough to be off the dipolar field action zone. The main result is that the parallel dimers have an enhanced induced field due to a pronounced resonance which is larger about one order of magnitude compared to the quenched fields in perpendicular dimers. Under such conditions, where the spacing within the dimer is approximately less than half the radius (25nm here), the perpendicular response can then safely be neglected. This fact is also demonstrated in the field pattern shown as the inset of Figure 18, where we have obtained the scattering and absorption cross sections of the two dimer orientations using fullwave computations. The perpendicular dimer's NPs can be reassigned to two new parallel dimers. Therefore, the response of the random structure can be approximated with dimers all parallel to the polarization of light, which is still a dipolar response as their radiation patterns (depicted in Figure 19) show no significant difference in the dipolar field emission. This opens the possibility to view the structure as a polarization insensitive ENZ metamaterial, since we can reassign all NPs to the parallel dimers according to the polarization of light. In other words, whenever a different polarization is incident on the structure, there will be parallel

dimers exhibiting the majority of the response [Figure 20(a)], and we are justified in decomposing the structure made from random embedding of nanospheres into parallel dimers. This concept is illustrated in Figure 20(a).

The analysis stated above could be very useful in simplifying the study of plasmonic random structures. As a matter of fact, it has been demonstrated [66] that random aggregates of plasmonic particles show a red-shifted LSPR, and what we have just provided is a proof of the physical mechanism associated with this effect. However, there is still a need to obtain the refractive index of such a random structure.

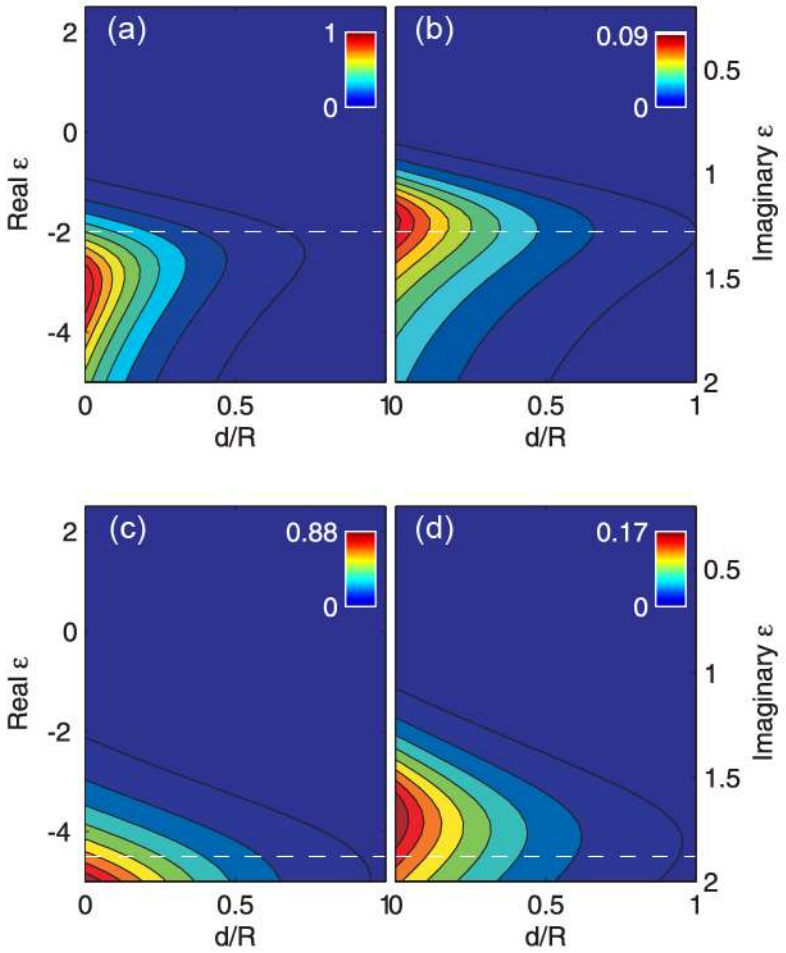


Figure 17: Induced fields in dimer nanoparticles (NPs) for two different hosts: air (a, b), ligands (c, d). Left and right panels show the parallel (a, c) and perpendicular (b, d) orientations, respectively. The horizontal line depicts the LSPR condition $\varepsilon_i = -2\varepsilon_h$.

In order to do this, the computational fullwave method is used to extract the S-parameters of the structure and then a common index retrieval method [9,10] is applied to find the real part and imaginary part of the permittivity, permeability, and refractive index. Since, the complex interactions of the ENZ metamaterial are now greatly simplified using dimer building blocks, it is then only necessary to study the interaction between the dimers for obtaining the bulk properties. For this purpose, an infinite array of dimers can be created in the computational environment by employing the Floquet

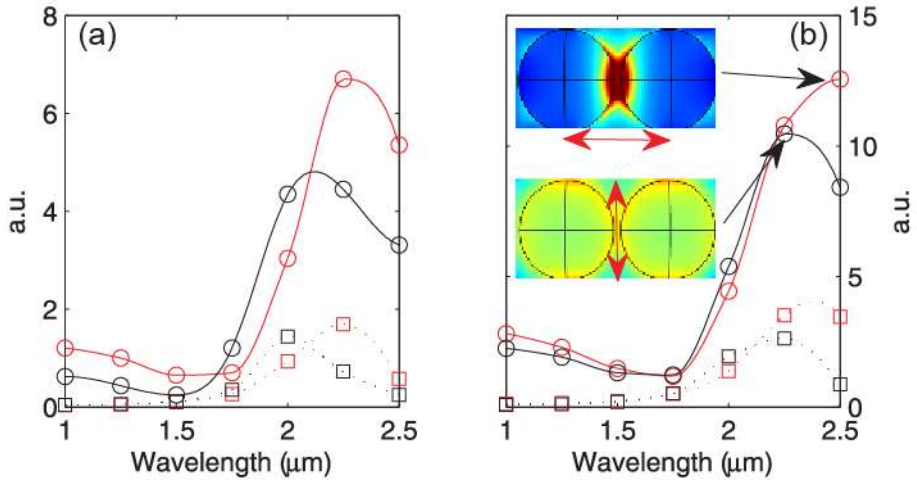


Figure 18: Scattering (solid curves) and absorption (dotted curves) spectra of AZO nanoparticles (NPs); (a) for a single spherical NP of radius 50 nm in the air (black) and in the ligand host (red), (b) for dimers oriented perpendicular (black) and parallel (red) to the polarization of light in the ligand host. Inset shows the electric field distribution at peak scattering frequency.

boundary condition onto a unit cell which is composed of only one dimer. This method simulates a medium from a thin layer of dimers with the thickness equivalent to the diameter of the NPs. Then the bulk properties are obtained by averaging the retrieved refractive index over various dimer arrays with different spacing that will be limited to the particle size [39].

As is obvious from the refractive index retrieved for the random plasmonic metamaterials [Figure 20b], the ENZ band is located in the vicinity of 2.2 μm, which is just at a shorter wavelength than the associated LSPR. This opens the opportunity to artificially blueshift the ENZ band by increasing the doping of aluminum in AZO to spectrally tune the optical properties to the telecommunication wavelengths at 1.5 μm [AZO can be doped high enough to resemble metal-like optical properties in the NIR (Ref. 38)]. Also, as the averaging procedure suggests, there is also a control mechanism over the total loss of the ENZ metamaterial, which can be manipulated in favor of

different applications. That is, we can simply increase or decrease the spacing between the dimers for a tunable loss. This can be done by controlling the amount or the type of ligands used for the self-assembly process. The loss is of main importance when dealing with the applications and it is another reason why AZO is a better candidate over noble metals. Metallic NPs also exhibit LSPR which are dependent on the size, shape, material, and host medium of the particles [31]. But, at the high frequencies of optical and NIR, the interband electronic transitions of metals cause a high attenuation for light [32],which degrades the performance of the plasmonic system for application purposes. It is inefficient, particularly at NIR frequencies, to compensate for this loss by the use of a gain medium [33] since the losses are larger, comparatively, and also there is still a need for high permittivity host dielectric materials to satisfy the plasmonic resonance condition. AZO can be considered a diluted metal, and when it is used in the form of NPs instead of a layer, its response is even more diluted because of the host medium occupying the rest of the space.

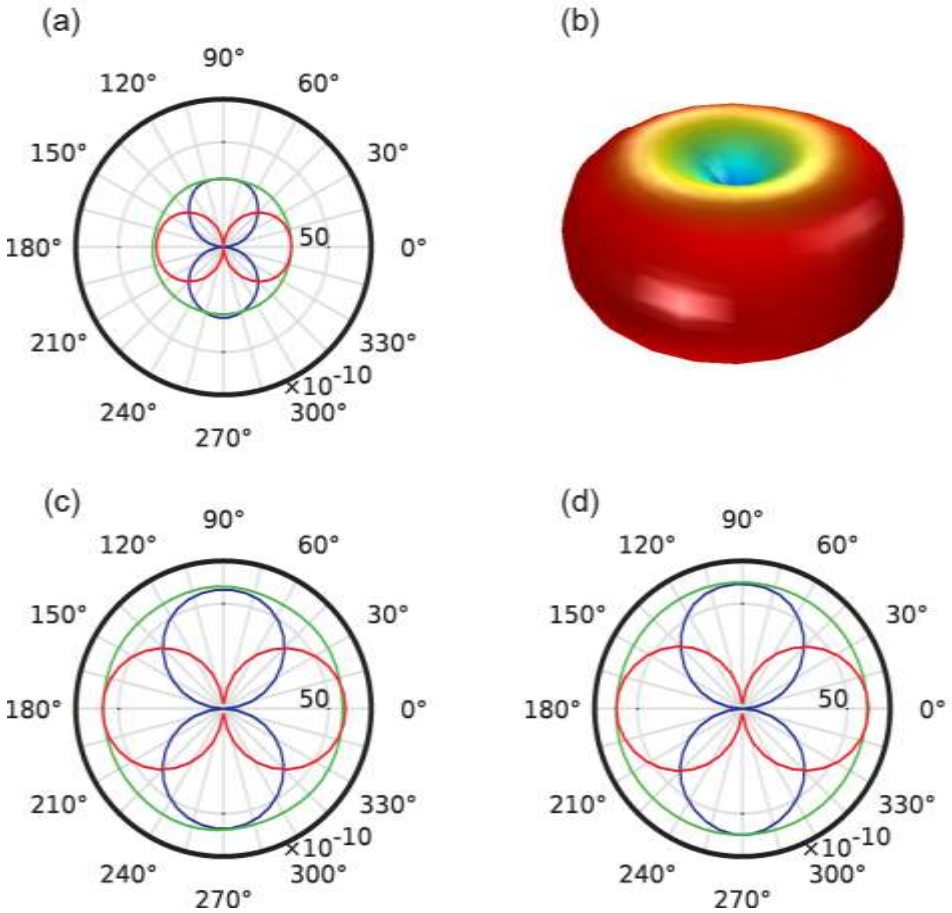


Figure 19: Radiation patterns of single AZO NP (a), parallel (c), and perpendicular (d) AZO dimer obtained by fullwave computations. In (b), a three-dimensional radiation pattern is illustrated that much identically corresponds to the dipole resonance emission of each of the cases (a),(c), and (d).

For a comparison with simple effective medium theories (EMTs) to calculate the permittivity of the bulk structure, we use the symmetric Bruggeman mixing rule [Eq. (29)]. Then, the sole factor in determining the effective permittivity of such metamaterial structures will be the filling factor (*f*). In our study, the maximum filling factor is about ½, which is the touching limit. Then the effective permittivity of the structure can be obtained by [40]:

$$\varepsilon = \frac{1}{4}\Big\{(3f_1 - 1)\varepsilon + (3f_2 - 1)\varepsilon_0 \pm \sqrt{[(3f_1 - 1)\varepsilon + (3f_2 - 1)\varepsilon_0]^2 + 8\varepsilon\varepsilon_0}\Big\} \quad (29)$$

with $f_1$ and $f_2$ as the filling factors of AZO and the host, respectively. A quick calculation based on increasing $f_1$ from 0.1 to about 0.5 is depicted in Figure 20c. It is obvious that using the regular EMTs that are not adapted for plasmonic particles, these cannot provide an accurate response of the structure. The EMT underestimates the losses, since the enhanced light-matter interaction due to plasmonic resonance is simply ignored. For the refractive index, the accuracy for the wavelength of the lowest value is not in agreement with the fullwave simulations. It is also worth mentioning that one may use a recent, but complicated, EMT approach adapted to plasmonic NPs (Ref. [47]), which includes the effects of dressed polarizability due to the interparticle interactions.

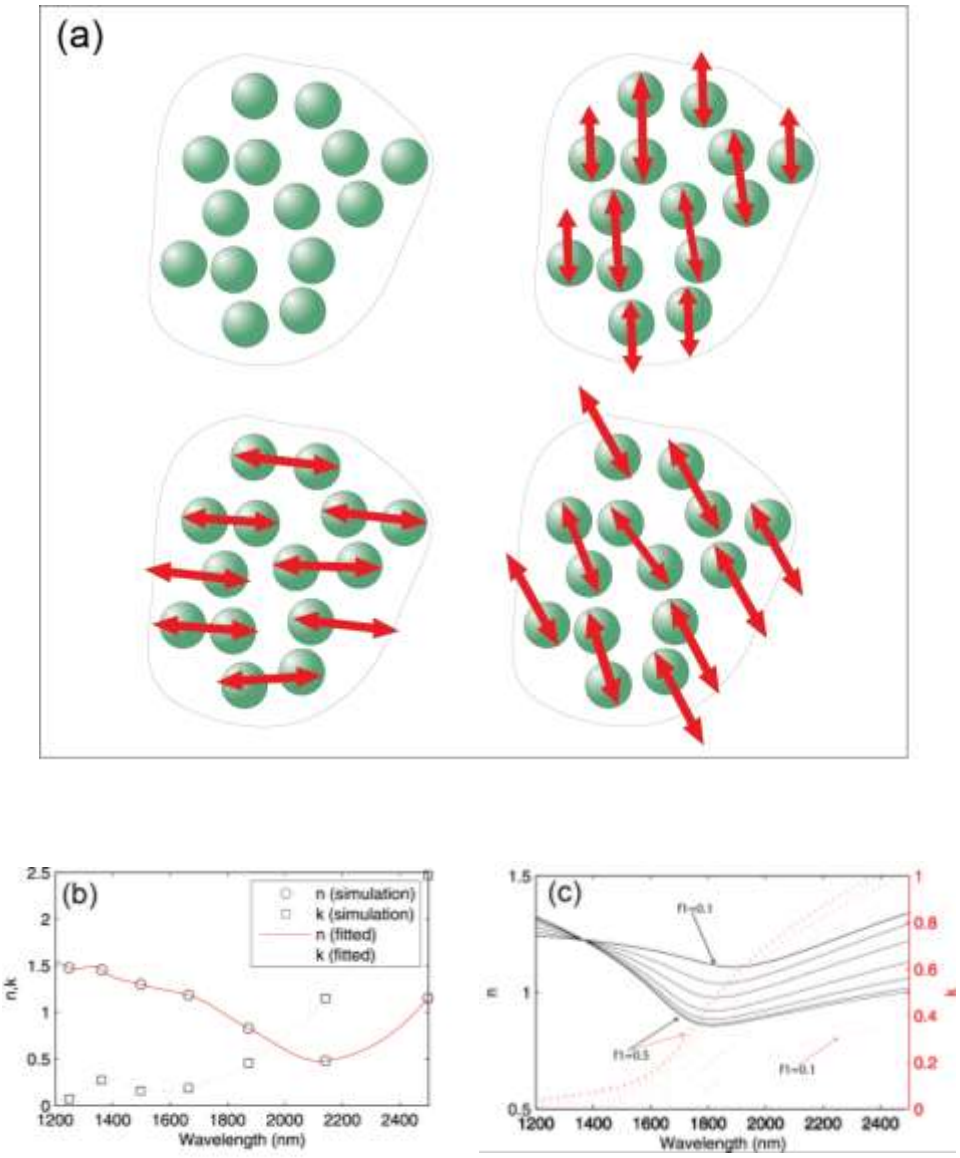


Figure 20: Demonstrations of polarization dependent orientation of dimers in three different configurations (a). Retrieved refractive index of a random layer of epsilon-near-zero metamaterials comprised of 50 nm AZO spherical NPs (b). Results of symmetric Bruggeman effective medium theory, with different filling factors for refractive index of a similar layer (c).

### 2.2.3. Conclusion

We investigated the fabrication possibility and optical characteristics of a polarization insensitive ENZ metamaterial composed of aluminum-doped zinc oxide NPs by the use of an equivalent circuit model that simplifies the random self-assembled structure into

collection of dimers. Considering the coupling of localized surface plasmons, we demonstrated the dominance of parallel dimer orientation to the perpendicular one, and we then applied this model to the whole medium. Subsequent results show polarization insensitivity and also a general redshift in LSPR of the plasmonic ENZ medium. The results could be of major significance for the future fabrication purposes of plasmonic ENZ metamaterials and also for the study and prediction of plasmonic aggregates' properties.

## 2.3. Polarization Dependent Bandwidth in Low-Index Plasmonic Metamaterials

We investigate the visible range, less-than-one index bandwidth, $n_{\text{visible}} < 1$, of an optical metamaterials structure comprised of plasmonic gold nanoparticles, and show that it is highly dependent on the polarization of incident light. Fullwave finite element method is used to obtain the spectral characteristics of the structure. We have found spectral bands over which the structure shows the desired low-index. Further, a possible increase of the bandwidth as large as 270% is demonstrated by a change in the incident polarization that extends the low-index bandwidth range (503nm to 600nm) asymmetrically into a wider range (485nm to 750nm) covering longer wavelengths close to near infrared. This asymmetric overlap might have the potential for new optical applications.

### 2.3.1. Introduction

The exotic properties of metamaterials, such as negative permeability (MNG) or simultaneous negative permittivity and permeability [51,52] (DNG), arise from engineering the geometry of so-called meta-atoms to exhibit a desired response in

interaction with light. Another important property of metamaterials is the capability to provide an index of refraction smaller than unity for which the phase velocity of light advances faster than that of the free space. This epsilon-near-zero (ENZ, $\varepsilon \approx 0$), or low refractive index (low-index, $n < 1$), property can be exploited in different applications ranging from cloaking [59], ultra-narrow waveguiding [60], shaping the phase pattern of radiation sources [61], etc.

RF and microwave metamaterials with ENZ property have been already realized. In the optical and infrared (IR) spectral range, it is possible to fabricate such structures by embedding suitable inclusions, such as nanoparticles, in a host medium. One can use a self-assembly approach for the embedding purpose, in which appropriate ligands are used to keep the nanoparticles in a desired proximity to each other [62-64]. Recently, a self-assembled monolayer of thiolene-functionalized gold nanospheres has been demonstrated to have near-zero index of refraction [65]. Interferometry can then be used for measurement of the resulting optical properties, such as refractive index and extinction coefficient.

While achieving the low-index property might be important, the spectral range over which the optical properties remains less than unity is of importance, too. In addition, some applications might require a wide bandwidth, while others should have a narrower one. Moreover, there could be new applications if an active tuning of low-index bandwidth could be realized. Here, we study the visible range, low-index bandwidth of such structures to investigate the methods for achieving these properties. This sections is aimed to investigate and study the bandwidth of ENZ structure.

### 2.3.2. Approach

As mentioned earlier, utilizing suitable inclusions and host media, the real part of the refractive index can be reduced to values less than 1. To find the size range of inclusions, we note that the particles being included in the host should be subwavelength in size and on the order of approximately λ/10 to fit into the metamaterial definition range. Gold particles with a strong plasmonic resonance in the visible range are suitable. The absorption and scattering of these small particles can be calculated using Mie theory [66]. Assuming spherical NPs, their polarizability is:

$$\alpha = \frac{-6\pi\varepsilon_0\varepsilon_h j}{k\text{^}3} \times \frac{m\psi_1(mx)\psi_1'(x) - \psi_1(x)\psi_1'(mx)}{m\psi_1(mx)\xi_1'(x) - \xi_1(x)\psi_1'(mx)}, \tag{30}$$

$$\psi_1(\rho) = \rho j_1(\rho) = \sin\frac{\rho}{\rho} - \cos\rho \ , \tag{31}$$

$$\xi_1 = \rho h_1^{(2)}(\rho) = \left(\frac{j}{\rho} - 1\right) e^{-jp} \ , \tag{32}$$

$$m = \frac{k_m}{k} = \sqrt{\frac{\varepsilon_m}{\varepsilon_h}} \ , k_m = \omega\sqrt{\varepsilon_m}/c \ , \tag{33}$$

where $\psi$ and $\xi$ are Ricatti-Bessel functions. To get an insight into the contributing effects on the polarizability, $\alpha$ can be extended as a series with respect to the small parameter $x$:

$$\alpha = 4\pi\varepsilon_0\varepsilon_h a^3 \times$$
$$\left[\frac{m^2+1}{m^2-1} - \frac{3}{5}\frac{m^2-2}{m^2-1}x^2 + \frac{j^2 2}{3}x^3 + O(x^4)\right]^{-1}. \tag{34}$$

The first term in Eq. 34 corresponds to the quasi-static polarizability (also Clausius-Mossotti relation), the second term may be identified with a dynamic depolarization, and

the third term is the radiation damping. Then the scattering, absorption, and extinction efficiencies are defined, respectively:

$$Q_{sca} = \frac{k^4}{6(\varepsilon_0 \varepsilon_h \pi a)^2} |\alpha|^2, \tag{35}$$

$$Q_{abs} = -\frac{k}{\varepsilon_0 \varepsilon_h \pi a^2} \mathrm{Im}\{\alpha\}, \tag{36}$$

$$Q_{ext} = Q_{sca} + Q_{abs}. \tag{37}$$

The host medium has a very important effect on the localized surface plasmon resonances of these nanoparticles. For the host medium, air, water, and epoxy for example can be used, which have refractive indices of, respectively, 1, 1.33 and 1.60 at visible wavelengths.

In Figure 21, the extinction efficiencies of different gold nanoparticles are shown. The redshift of the peak extinction with increasing the refractive index of the host medium, and also increase of extinction with the particle size, are clearly seen. When such plasmonic particles are brought together, they develop a collective response to the electromagnetic interactions, as in the bulk. To find the effective refractive index of the bulk structure, we assume a densely packed monolayer of gold nanoparticles. It should be noted that at such close proximity, it is possible to simplify the study of the structure, since a lattice like arrangement of the particles occurs. The spherical nanoparticles can form a hexagonal lattice, shown in Figure 22a. Further, by analyzing the irreducible Brillouin zone of such a lattice (Figure 22b), it is found that we can characterize the structure through the optical responses in two distinct directions; ΓK and ΓM. For this

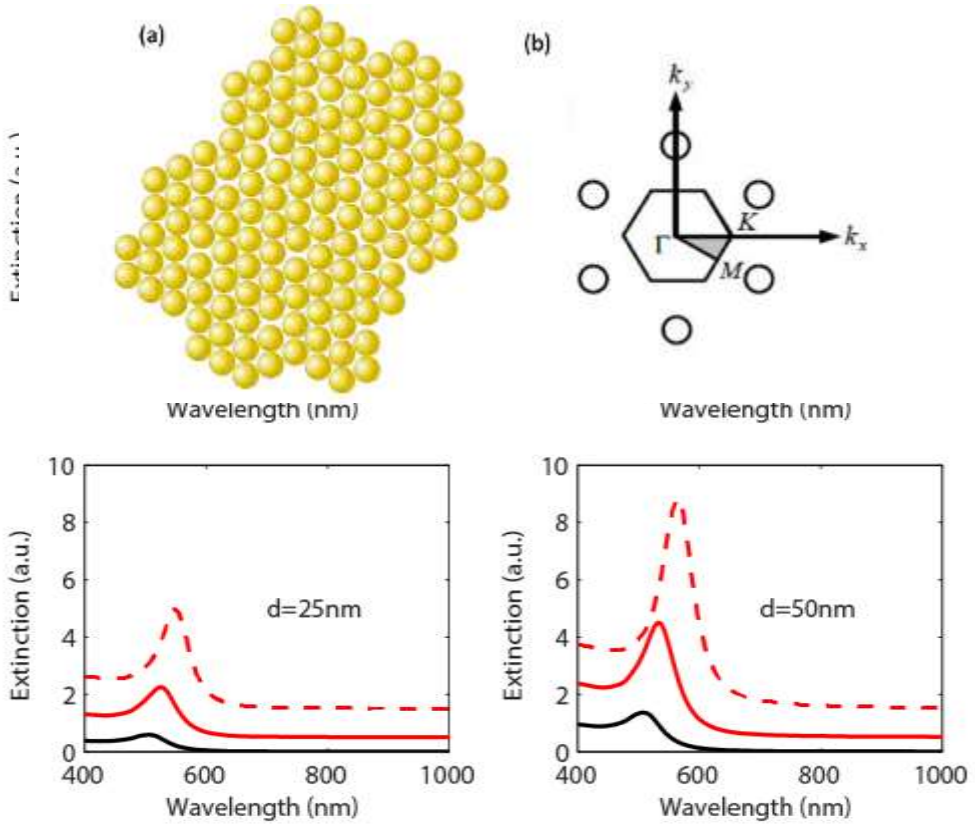


Figure 21: Extinction spectra for nanoparticles of gold in different host media. Single isolated nanoparticles of sizes (diameter) 10nm, 17nm, 25nm, and 50nm are assumed in hosts of air (n=1.00), water (n=1.33) and SU8 epoxy (n=1.66). The spectra are calculated using Mie theory.

purpose, we use a fullwave FEM electromagnetic simulation to study only the unit cell of the lattice.

### 2.3.3. Computation

The three dimensional layout of the fullwave computations are shown in Figure 23. The unit cell is a planar structure in the *y*-*z* plane, and can be extended infinitely into a monolayer, using computational Floquet boundary conditions in both *y* and *z* directions, which account for the periodicity. To explore the optical properties of this structure, we scan over the wavelength range between 400 nm and1000 nm. In order to keep a low computational cost, the step size for the wavelength scan is set for 25nm.

Considering the irreducible Brillouin zone of a hexagonal lattice (Figure 22b), the polarization of the incident light should be along the directions of ΓK and ΓM in order to fully investigate the different responses of the structure. That is, we can distinguish two possible interaction schemes: in one case, the electric field vector of linearly polarized light effectively sees parallel chains of nanoparticles in the ΓM direction, but the other type of interaction happens for nanoparticles in the ΓK direction. In each case, the coupling of surface plasmonic waves would be different, leading to shifts in the spectral response of the whole structure. Utilizing the rotational symmetry of the hexagonal lattice, one can see that *y* and *z* directions can be used as substitutes for ΓM and ΓK, respectively, with the propagation along the *x*-axis. To retrieve the wavelength dependent refractive index, we employ the method that uses scattering (S) parameters [67, 68]. In the method, the elements of the S-matrix are obtained from the computational environment, and then used to calculate the material's properties. That is:

$$n = \frac{1}{kd}\cos^{-1}\left[\frac{1}{2S_{21}}(1 - S_{11}^2 + S_{21}^2)\right], \tag{38}$$

$$z = \sqrt{\frac{(1 + S_{11})^2 - S_{21}^2}{(1 - S_{11})^2 - S_{21}^2}} \tag{39}$$

$$\varepsilon = \frac{n}{z}, \tag{40}$$

$$\mu = zn \tag{41}$$

where $S_{11}$ and $S_{21}$ are the elements of the scattering matrix, $k$ is the wavenumber, and $d$ is the thickness of the layer. Preferably, the condition $kd \ll 1$ should be met to be assured of an accurate estimation. This is a well-established method of retrieving the refractive index, although there have been a few discussions on the physical meaningfulness of the results [69-71].

### 2.3.4. Results and Discussions

On interaction of light with the nanoparticles in the structure depicted in Figure 22a, their close proximity gives rise to coupling between localized surface plasmons which exhibit behaviors unique to each polarization state. We can study the displacement currents in the unit cell to examine the response of the medium and find the coupling schemes (shown in Figure 23c,d). This also allows for analytical intuition when studying the structure using an equivalent circuit model [72]. However, apart from dilute mixtures of particles (e.g. analyzed in [73]), the numerous interactions and couplings between the particles in such a dense structure make it tedious for a straightforward analysis using circuit theory, and directly solving Maxwell's equations using computational methods, although time consuming, has a great advantage.

The details of interactions investigated using FEM are as follows. The electric field amplitude in the particles for a frequency close to the resonance is shown in Figure 23c,d. The “hot spots” (i.e. strong field enhancements due to coupling) where the neighboring particles provide efficient coupling along the direction of the incident electric field of the light are different in each polarization case. There is a weak side coupling in Figure 23c, whereas almost no side coupling can be observed in Figure 23d. Also, for ΓM input polarization, there is a stronger coupling between nanoparticles that are ordered back to back in a chain. For the ΓK polarization, the coupling to the next particle is separated by two particles (Figure 23d), resulting in a weaker response compared to the previous situation.

In Figure 24, we illustrate the components of the electric field throughout the unit cell to examine the nature of local interactions. Also, the *x*-component of magnetic field *H* is shown in Figure 25. The multipole response of the particles is clearly depicted.

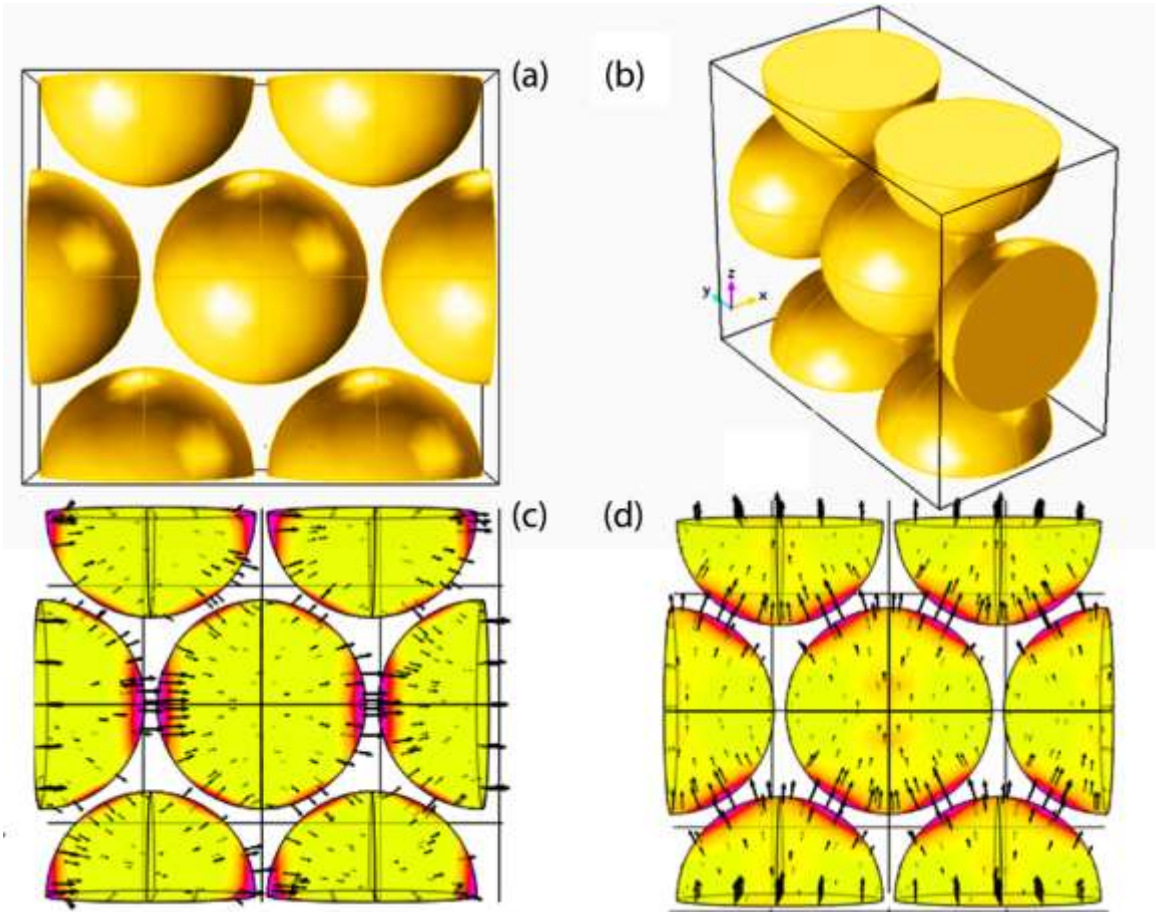


Figure 23: (a,b) Geometry of the unit cell for the fullwave computations in the FEM environment. (c) Maps of electric field amplitude on the nanoparticles of the unit cell together with vectors of displacement current in response to an incident polarization along ΓM, (d) ΓK.

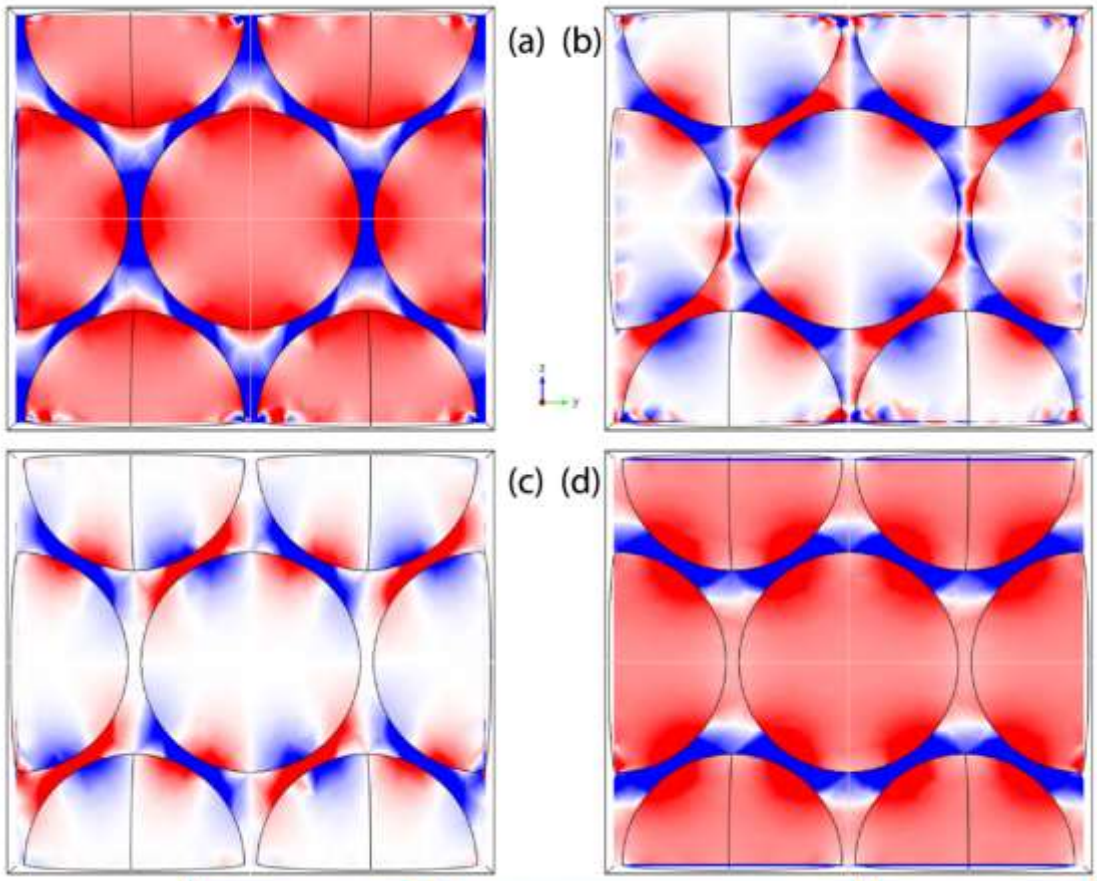


Figure 24: Components of electric field in the unit cell: (a) Ey, (b) Ez in response to input polarization of ΓM, and (c) Ey, (d) Ez in response to input polarization of ΓK. All plots are normalized the same.

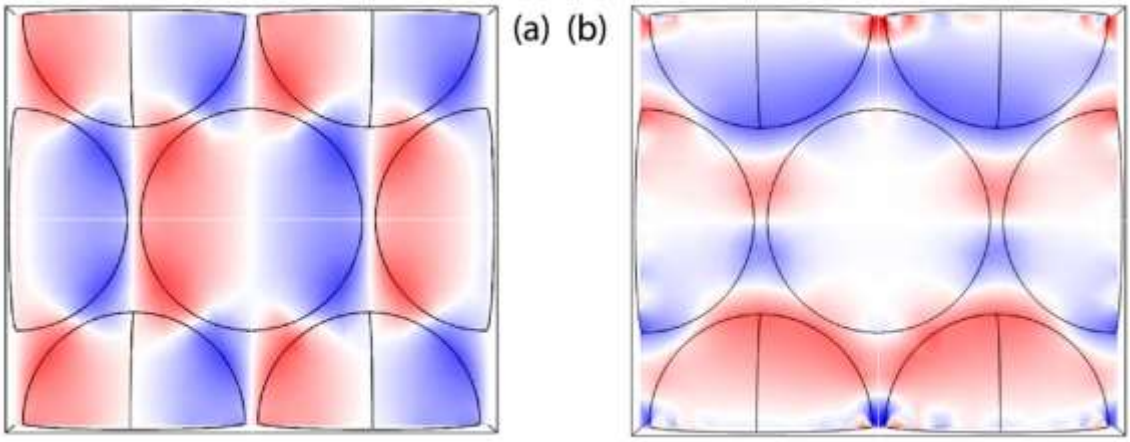


Figure 25: The x component of magnetic field H in the unit cell for input polarization of (a) ΓM, and (b) ΓK.

We then employ the retrieval steps in Eqs. (38) to (41) for calculation of the characteristics of the structure in each polarization excitation. The results are shown in Figure 26 for refractive index, impedance, permittivity and permeability. Insertion loss and return loss of the structure can also be comprehended by use of $S_{21}$ and $S_{11}$, respectively. It is evident that such coupling of plasmons leads to a red-shift of the resonance frequency compared to the isolated state. We found that polarizations along ΓM and ΓK directions result in non-identical red-shifts; the former being larger since the coupling of localized surface plasmon resonances is more effective and stronger in this case. Based on the particle size and the gap size between the particles, the minimum refractive index obtained using 17nm gold nanoparticles is approximately 0.8 for each polarization. We observed that with controlling the gap size (here 4nm), the refractive index can be tuned to lower or higher values, as well. Note that we have used the bulk material's properties from Ref.[74], and also we see from Eqs. (38) to (41) that the plasmonic effects are size-independent. One might consider the size-dependence plasmon behavior which manifests itself as an increase in the plasmon bandwidth with decreasing particle size (inversely proportional to the radius, $r$). To correct for this, it is possible to include a size dependent damping constant (γ) which equals the plasmon bandwidth in the permittivity of the gold nanoparticles as [75]:

$$\gamma(r) = \gamma_0 + \frac{A\nu_F}{r}, \tag{42}$$

$$\varepsilon(\omega) = 1 + \varepsilon_{IB}(\omega) + \frac{\omega_p^2}{\omega^2 + i\gamma\omega}. \tag{43}$$

In Eqs.(42)-(43), $\gamma_0$ is the bulk damping constant, $v_F$ is the velocity of electrons at the Fermi energy, $A$ is a theory-dependent parameter, $\varepsilon_{IB}$ is the interband permittivity term, and $\omega_p$ is the bulk plasmon frequency. There have been experimental results on determination of complex dielectric constant of a single gold nanoparticle [76]. Here, we neglected those effects in order to investigate the overall effects of the particles in this kind of optical metamaterial.

The spectral bands over which the index-less-than-one occurs are 485nm to 750nm and 503nm to 600nm for ΓM and ΓK, respectively, and this translates to bandwidths of 265nm and 97nm for each polarization (Figure 27). That is a 270% increased band-width just by changing the polarization of light. More interesting to note, is that there is an asymmetric overlap of the low index bandwidth which extends to the longer wavelengths as the polarization changes to ΓM direction. This asymmetric overlap can be used in applications, such as for modulators for which a polarization dependent low and high refractive index can be introduced into the device.

In addition, it is also useful to obtain the material characteristics for unpolarized incident light. For this purpose, we should average the two responses and weight them based on their occurrence given the symmetry of the system. For the hexagonal lattice, each of the ΓM and ΓK directions repeat 6 times, hence we can simply weight them 50% and 50% when averaging. The result is shown in Figure 28 for the refractive index. Such averaging might also be useful for practical situations in which some degree of disorder is present in the position of the nanoparticles. The disorder can result in a limited bandwidth as has been explored in Ref.[77].

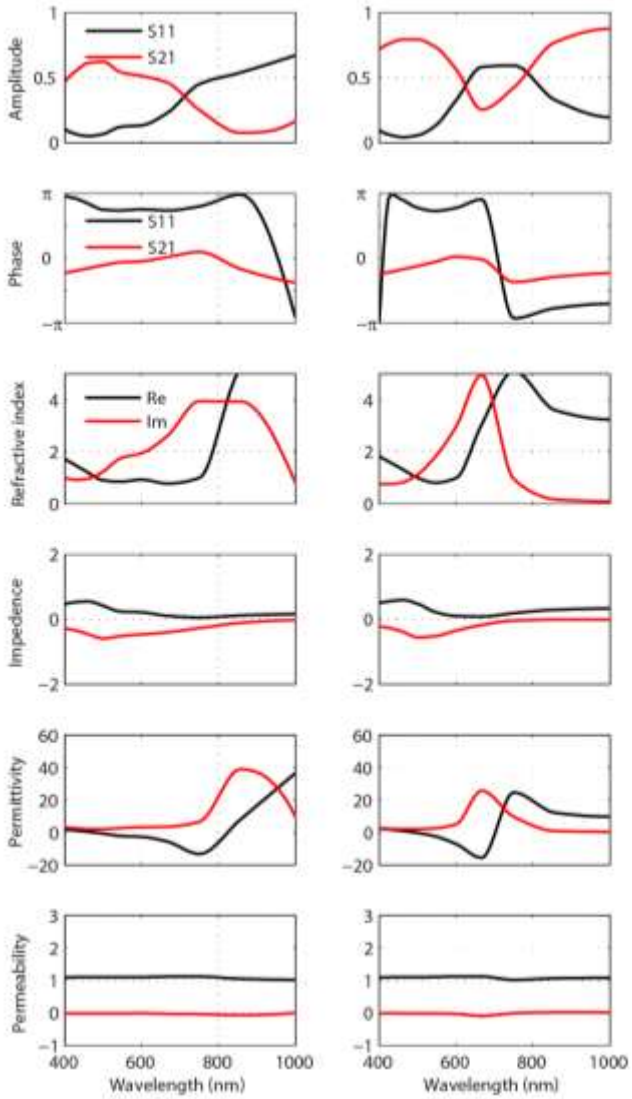


Figure 26: Retrieved spectral properties of the structure from S-parameters; Refractive index, impedance, permittivity and permeability of the ΓM (ΓK) response are shown on the left (right) panel.

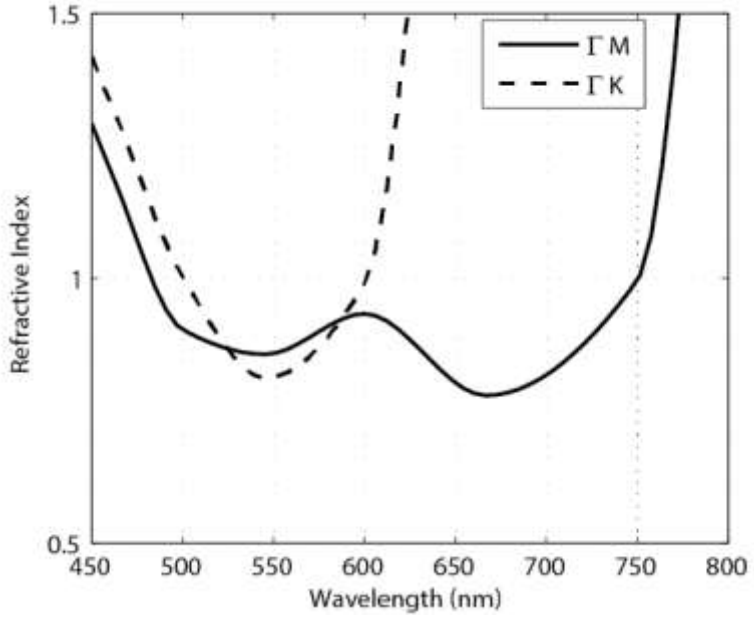


Figure 27: Comparison of index spectra and bandwidth for two input polarizations.

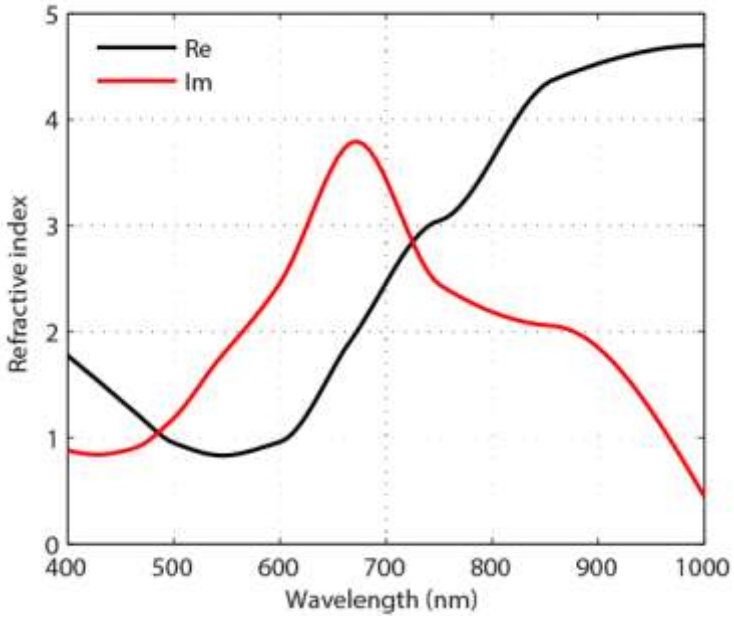


Figure 28: Estimated response of the structure (only the refractive index) with unpolarized incident light.

### 2.3.5. Conclusion

We have investigated the visible spectral range, less-than-one index ($n < 1$) bandwidth of an optical metamaterial comprised of plasmonic gold nanoparticles, using

fullwave FEM and showed its high dependence on the polarization of incident light. We have found spectral bands over which the structure shows the desired low-index and we demonstrated an increased bandwidth of 270% resulting from a change in the incident polarization. The extended low-index bandwidth is asymmetric for longer wavelengths close to near infrared.

# CHAPTER 3: HIGH ABSORPTION OPTICAL METAMATERIALS

In this chapter, in contrast to earlier results, our purpose is to maximize absorption in the optical metamaterial system. This is a desired absorption which can be utilized in the devices for detection and sensing. Again, according to the definition of metamaterials, meta-atoms with sizes much smaller than the wavelength of the incident light are considered. These meta-atoms are made of composite nanowires and plasmonic nanoparticles. In the following sections, the investigation to obtain higher absorption in such structures using subwavelength elements is carried out.

## 3.1. Spectral Properties of Au-ZnTe Plasmonic Nanorods

Coupled plasmonic nanoparticles of Au and nanorods of ZnTe are considered here as the meta-atom element. They are modeled and fabricated. Fullwave simulation is performed to obtain an optimum design for enhanced light absorption and to explain scattering properties of the structure. The fabrication method for such arrays is described. Modeling the spectral properties using equivalent circuit theory is also implemented to provide an intuitive approach regarding the design of optical metamaterials with predetermined properties.

### 3.1.1. Introduction

ZnTe is an interesting II-VI semiconductor material used in optoelectronic devices, such as in photovoltaic elements [78-79], green light-emitting diodes [80], broad frequency field sensors [81-82], waveguides [83-84], and in gain media [85-86] – some

of these devices take advantage of nanoscale effects [87]. ZnTe also has nonlinear optical properties [88]. This material has been widely used because it is relatively easy to p-dope compared to other II-VI materials [89-90].Two wide bandgap materials configured as a type II heterojunction, such as a ZnTe/ZnO core-shell structure, could be used to achieve an ideal effective bandgap for solar cells [91], thereby exploiting both the optical coupling between the two components and unique electrical properties. Moreover, a vertical nanorod array of such core-shell structure improves light trapping and potentially reduces charge diffusion lengths, hence, further increasing photovoltaic efficiency [92-94]. To grow such ZnTe nanorods, it is possible to utilize gold nanoparticles to catalyze the growth via the vapor-liquid-solid (VLS) mechanism [95].

Noble metals such as gold and silver, or transparent conductive oxides, e.g. ITO and AZO, are known to exhibit plasmon oscillations when illuminated by light. During these oscillations, confined conduction electrons can be driven by the electric field of light into a resonant condition that is dependent on different parameters such as material, size, shape, and the host medium properties [96]. In the case of spherical nanoparticles of size $a$ and permittivity $\varepsilon$ in a host medium with permittivity$\varepsilon_h$, light scattering and absorption cross sections are defined by [97]:

$$C_{sca} = \frac{8\pi}{3} k^4 a^6 \left|\frac{\varepsilon - \varepsilon_h}{\varepsilon + 2\varepsilon_h}\right|^2,$$
$$C_{abs} = 4\pi k a^3 \mathrm{Im}\left[\frac{\varepsilon - \varepsilon_h}{\varepsilon + 2\varepsilon_h}\right],$$

where $k$ is the wavenumber of light. At the plasmon resonance condition ($\varepsilon = -2\varepsilon_h$), scattering and absorption maxima occur, assuming the imaginary parts of the permittivities are small. In the case of small particles with a loss term in their

permittivity, the absorption dominates over scattering. A discrete dipole approximation may also be applied to study the interactions in the quasi-static regime, that is, when the wavelength of light is much larger than the size of nanoparticles [98].

The composite plasmonic structures investigated here are ideally vertical arrays of gold nanospheres sitting on top of ZnTe nanorods. We numerically investigate the spectral response of these plasmonic Au-ZnTe nanostructures and find the effects of array structure parameters on the extinction of light. FEM is used to explore the best design for such nanostructure array. This composite structure can also be modeled as a metamaterial comprised of distinct nanocircuit elements [99,100]; which means that each nanostructure element can be represented by a nanoresistor, nanocapacitor or nanoinductor, or also combinations of them. Therefore, one can intuitively study the effect of design parameters, simply by studying the circuit elements. Finally, we explain the method of fabrication of such composite plasmonic structures.

### 3.1.2. Modeling

Using COMSOL as the FEM modeling tool, we designed a unit cell of coupled plasmonic Au-ZnTe structure, where a gold nanosphere sits upon a ZnTe nanorod (see Figure 29 inset). The unit cell includes a gold nanosphere of size 100nm and a nanorod of diameter and length 60nm and 500nm, respectively. A linearly polarized light is assumed incident from above the unit cell. Parallel to the axis of the nanorod shown in Figure 29, and in both directions, we employed Floquet boundary conditions to account for neighboring nanorod structures that can contribute to coupling effects in computation process. In this way, we can simulate an infinite 2-dimensional array of nanostructure

elements which are replicas of the unit cell. Material properties of ZnTe and Au can be found everywhere, e.g. Ref [88] and [101], respectively.

We investigate the spectral properties of this initial design upon change of different parameters to find a suitable set of final parameters in order to guide the fabrication and predict the results of optical experiments. Two of the main parameters that can be controlled in the fabrication process are (1) the spacing between the adjacent plasmonic nanorods and (2) the length of ZnTe rods. The extinction spectra for a variety of reasonable spacing values are calculated and shown in Figure 29. It can be seen that the optical response of the structure is fairly sensitive to the spatial distribution of the nanostructure array, and there is an enhanced extinction in the wavelength range 550nm-700nm at 60nm spacing. Since the extinction is defined as the sum of absorption and scattering, one can expect an enhanced absorption or scattering or even both. Enhanced scattering, when directed toward the absorptive material, can help to increase light-matter interaction, which would eventually lead to an increase in the total absorption. This is a significantly important feature of this structure for use in applications such as solar harvesting or detectors.

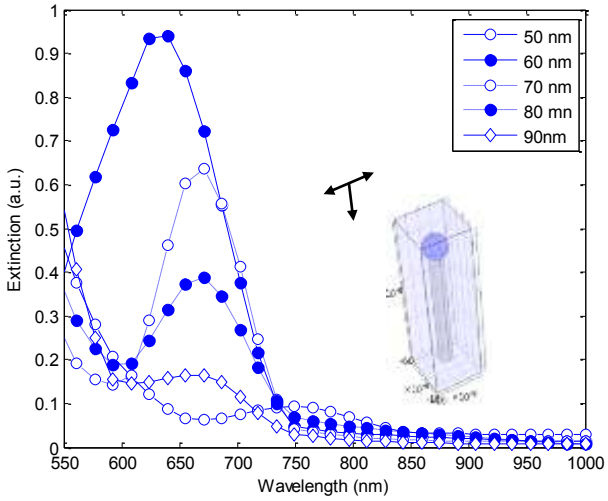


Figure 29: Extinction spectra of incident light as functions of spacing between nanorod structures. Au diameter is 100nm, ZnTe diameter and length are 60nm, and 500nm, respectively. The inset shows the unit cell of simulation.

Regarding the extinction peaks of Figure 29, it can be speculated that one of the main reasons for such an increase of the extinction is due to a reduction in the reflectivity of the structure. Therefore, light scattering and absorption occurs more at some spatial separations. Further, to explain other origins of these peaks at these optimal parameters, different processes could be taken into account. A mechanism that is common in all of the situations and is considerable at wavelengths in the range 550nm - 650nm rather than longer wavelength is the pronounced localized surface plasmon resonance (LSPR) of the gold nanospheres. The LSPR can result in enhanced light-matter interaction through two methods; the first one is the increased forward scattering from the gold sphere to the single nanorod that is attached to it, and the second method is the increased side scattering that adds to the amount of forward scattered light in the adjacent nanorods. This LSPR mechanism is also dependent on the spacing between nanoelements. Another mechanism that affects absorption and dependents on the length of the nanorods is the dielectric resonance due to interference. That is, when the optical length of the nanorod

approximately matches odd multiples of a quarter wavelength ($m\lambda/4n_\lambda$, m=1, 3, 5 …), then one can expect increased field in the structure, and vice versa. For example, with m=8 at $\lambda$=600nm, the optical thickness is 493.5nm, hence a destructive interference is expected resulting in a lower absorption, as can be seen in Figure 29. However, the peak for 60nm spacing is not obeying this rule, which suggests the existence of another dominant mechanism. The last mechanism for such extinction peaks includes both the effects of length and spacing such that the overlap between the scattered light and the neighboring nanorods is effectively higher at some conditions, resulting in an efficient secondary absorption. This could be the main reason behind the large peak at 60nm spacing, after ruling out the forward scattering. Therefore, it is the competition and collaboration between these mechanisms that lead to such different peaks as the length and the spacing parameters of the structure change. Also, as is obvious from extrapolation of all the curves to wavelengths shorter than 550 nm, a high extinction regime exists due to natural absorption in the materials.

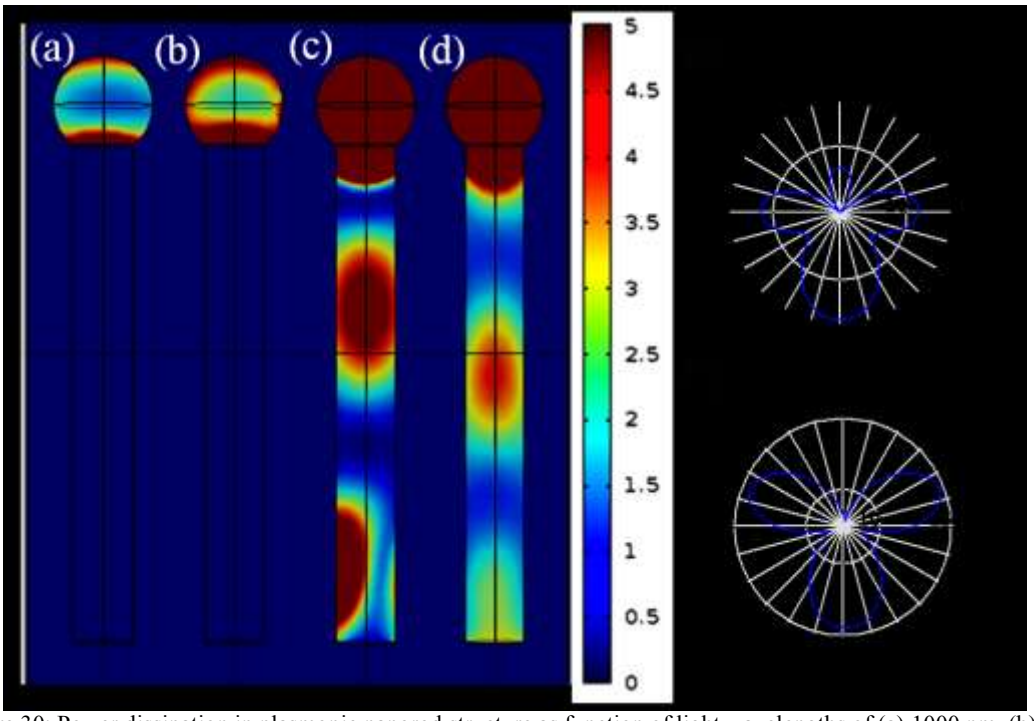


Figure 30: Power dissipation in plasmonic nanorod structure as function of light wavelengths of (a) 1000 nm, (b) 750 nm, (c) 600 nm, (d) 550 nm. The neighboring nanorods are placed with a spacing of 60 nm. Scattering profile of the Au-ZnTe element at λ=600nm for directions perpendicular (e) and parallel (f) to the polarization plane of light.

Figure 30 demonstrates the power dissipation of light in the nanorod structures. Here, the spacing is 60 nm and length is 500 nm. The different spectral response of light absorption both in a gold nanosphere and a ZnTe nanorod is observable from this figure. One can easily spot the high absorption localizations in the ZnTe rods (Figure 30c,d). There is also a high absorption region close to the top of the ZnTe rod. This is from the resonant forward scattering of the gold due to the LSPR effect, which, as mentioned earlier, directly helps the absorption. To confirm this, we computed the scattering profile of nanocomposite element (Figure 30e-f). The forward scattering into the nanorod and also side scattering to the neighboring nanorods can be verified. Also, the effects of coupling between nanostructures in the directions parallel and perpendicular to the polarization plane of light is observable in these patterns. Therefore, it is now clear that

the gold nanospheres can be utilized in a multi-purpose procedure; one is to help the growth of ZnTe nanorods through catalyzing the fabrication process, the second is to control the diameter of nanorods, and the third is to facilitate absorption through forward and side scatterings.

We also considered the effects of nanorod length on the spectral response of our plasmonic structure (Figure 31). The spacing is 60nm. For comparison purposes, since the lengths are different, the extinction values are normalized by dividing them by the volume of the nanorod in order to obtain a measure of effective extinction. The results show spectral sensitivity depending on the length of ZnTe nanorod. The majority of these variations can be due to spatial overlap with the side lobes of the LSPR scattering. It can be seen that the length of 250nm provides the best extinction over the spectral region where the absorption of ZnTe is relatively higher. To investigate the absorption inside the nanorod, we separate the contribution of the gold from the extinction spectra, and study the two main wavelengths where the absorption coefficient of the ZnTe is larger. The results are shown in Figure 32. We have found that a huge increase in the amount of absorption at wavelengths of 550nm and 600nm occurs when the nanorod length is around 250nm. This can be considered the optimal length for our structure. The insets of Figure 32 show the distribution of absorption throughout the nanorods. We can see that an effective absorption can be achieved in all the nanorods by carefully designing the spacing and length of the array structure. We also studied another case, when no gold was attached on top of the ZnTe nanorod. This study helps us understand the important role of gold in the enhancement of absorption. The results for the same two wavelengths are

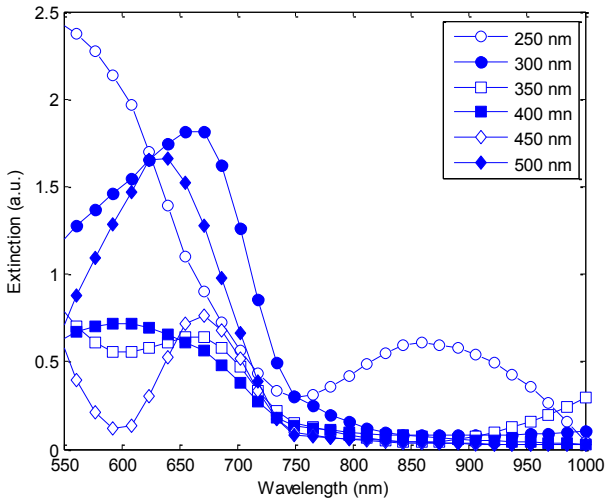


Figure 31: The normalized extinction spectra as a function of nanorod length with constant 60 nm spacing between structures.

plotted in Figure 32. The enhancement factor, which we define as the ratio of the absorption with gold nanosphere present to the absorption without it, rises to 8 for the optimal length we found earlier.

### 3.1.3. LCR Circuit Model

At our wavelength range of interest, the real parts of permittivity of Au and ZnTe are, respectively, negative and positive. They can be modeled as lumped circuit elements having an inductance ($L_s$) and a capacitance ($C_r$) response, respectively. Therefore, we can use an equivalent circuit to model the response of not only a single nanostructure, but also an array of such nanostructures. Figure 33 shows such circuit model. The resistors represent the materials' losses. We assume a square lattice of such structures and add capacitors $C_{ss}$ and $C_{rr}$ to account for the spacing between the spheres and rods, respectively. Since the spacing between the spheres is on the order of their radii, they can be coupled together. But for nanorods, the spacing is about 3 times larger than the radius. Thus, we neglect the coupling between them.

Applying the approach of Ref. [100] to obtain the equivalent values of circuit elements, we find $L_s$=10.1 femtoH (inductance of sphere), $C_{fs}$=2.78 attoF (fringe capacitance of sphere), Cr=293.6 femtoF (capacitance of rod), $C_{fr}$=6.67 attoF (fringe capacitance of rod), and the total values for LCR circuit would be L~10.1femtoH, C~11.1 attoF, R~233.4 Ω. This is a band-pass filter with a Q factor of 7.78 and fractional bandwidth of 0.1288, centered at the frequency corresponding to light of 630nm. The bandwidth of the resonance is about 80 nm. These characteristics approximately match the spectral properties of Figure 29 (60nm spacing). The plot of such a response is shown in Figure 33 together with simulation points of Figure 29. For comparing the results of LCR and FEM, it should be noted that the LCR approach is a quasi-static approximation which is independent of the wavelength. We used the optical properties of the materials at 630nm. Any deviations in the optical properties results in changes in the spectrum, particularly, at longer wavelengths. Another source of error in the use of the LCR method arises from neglecting the retardation effects. The structure we are using here is comparable to the wavelength of the incident light, which dictates that retardation effects should be taken into account.

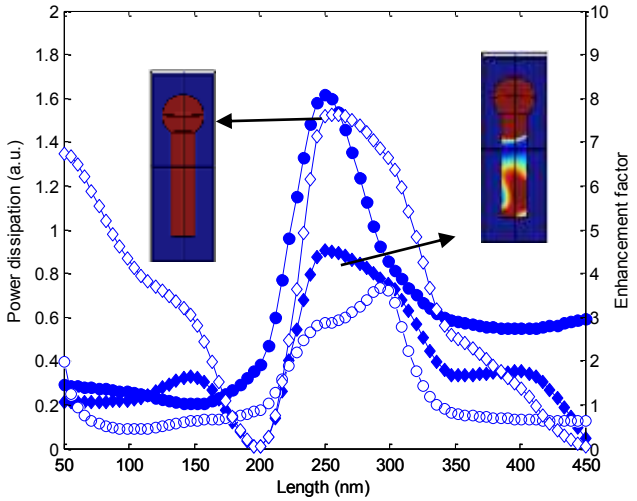


Figure 32: Power dissipation (filled) and enhancement factor (empty) versus ZnTe length at wavelengths of 600nm (diamonds) and 550 nm (circles).Insets: Absorption distribution at 550 nm (left) and 600 nm (right).

We have investigated the coupling of gold spheres using this LCR method, and concluded that only those spheres aligned parallel to the polarization of light can be coupled. The coupling induces a dipole in each sphere whose magnitude is dependent on the distance between the spheres. In Figure 33, we have calculated this dipole moment compared to the local dipole response of the sphere in response to the incident light. As is obvious, the coupling is strong only at close proximity and it can shift the resonance of the LSPR to the red. However, with the geometrical parameters we used for the simulation, it is unlikely to have a red-shift from LSPR coupling, when referring to these calculations. Nevertheless, one can easily and intuitively figure out that both the circuits of the sphere and rod are coupled together and the capacitor response of the rod affects the resonance frequency of the sphere (such that the total capacitance is increased), which turns out to be a red-shift in the resonance of the structure.

### 3.1.4. Fabrication

Here we only report the fabrication procedure and the resulting structures. Au-ZnTe nanostructures have been fabricated in several steps. First, a thin film of gold was sputtered onto Si(111) wafer. Following this, the wafer was thermally annealed to create Au islands. The Au thin films on Si(111) wafers were heated to 600$^{o}$, 625$^{o}$, 650$^{o}$, or 700$^{o}$C over 30 minutes, for one hour and then allowed to cool naturally. Sputtering thicknesses from 1-10 nm were investigated but only thicknesses above 5 nm resulted in measurable Au islands. Based on these capabilities, we were able to create Au islands with a size range of about 100nm that consequently resulted in a narrower diameter for the ZnTe nanorods. We note that the Au dimensions directly control the ZnTe nanorod diameter in the growth. Finally, the Au islands were used to catalyze ZnTe growth in a chemical vapor deposition (CVD) process to create the Au-ZnTe structures. To investigate the sample, we used dark field microscopy to observe the LSPR and spacing between the composite elements, respectively (Figure 34). Characterization of electrical and optical properties of this structure is beyond the scope of this dissertation.

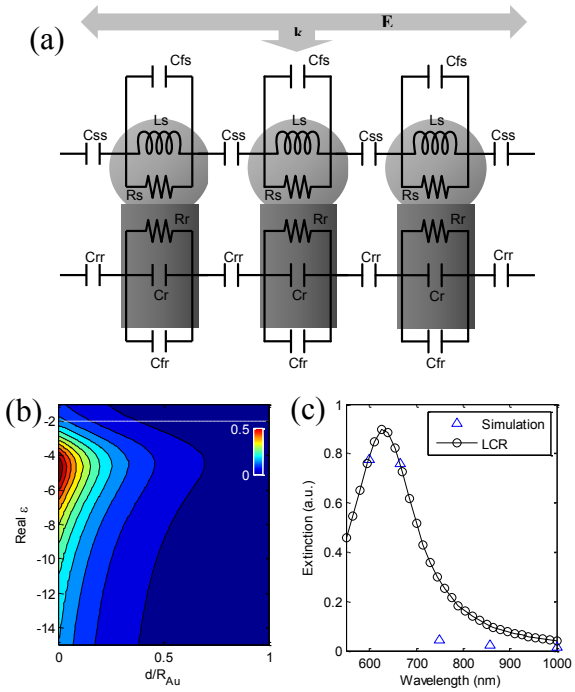


Figure 33: (a) Schematic of Au-ZnTe array with equivalent circuit model elements. (b) Calculation of induced relative dipole moment in gold spheres. The white line is the LSPR in air for an isolated sphere. (c) Comparison of LCR circuit response and simulation data points for 60 nm separated array of Figure 29.

### 3.1.5. Conclusions

We have studied the spectral properties of a composite plasmonic array structure made from gold nanospheres and ZnTe nanorods. For applications in solar harvesting and detectors, we investigated the effects of structural parameters on light absorption and scattering. We found an optimum design for nanorod length and array spacing which can provide enhanced extinction. Moreover, we used an LCR equivalent circuit model to intuitively study the response of our proposed structure. One of the main conclusions of our work is the role of plasmonic gold spheres incorporated into our design. We found that the presence of gold particle can have a few benefits: one is to help in fabrication for the growth of ZnTe nanorods, and another is to provide more absorption in ZnTe nanorod

through LSPR. The results of these studies are of significant importance toward novel devices for solar harvesting and detectors.

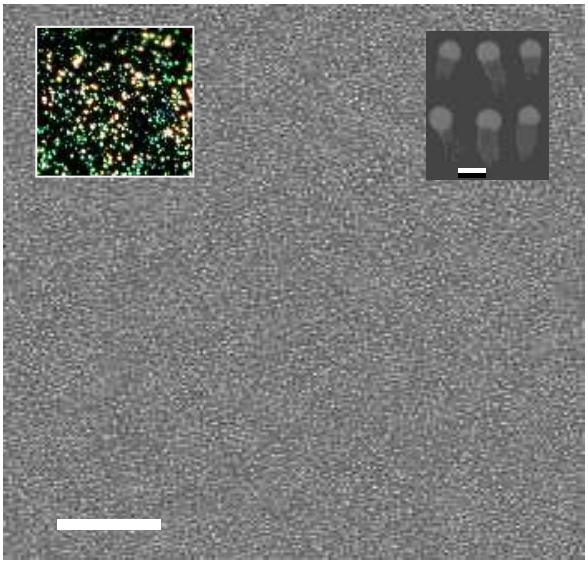

Figure 34: The SEM image of the large scale fabricated composite nanostructure. The scale bar is 10μm. Insets show (left) a dark field image of the Au islands, (right) selected nanostructure elements at 200nm scale.

## 3.2. Nanowire with Nanoantennas

In this section, we develop the previous results further with and an insight on the role of the plasmonic particles. In addition, we consider a more specific form of the input excitation to be the solar spectrum. We investigate a novel light conversion scheme in nanostructures for the highly demanding field of plasmonic solar cells. In our study, we incorporate vertical nanorods made of semiconductor materials, which are coupled optically to plasmonic nanoantennas for optimal absorption of sunlight. Utilizing the unique properties of localized surface plasmon resonances, we create dedicated nanoantenna elements such that the emission pattern is effectively directed toward the absorber material.

As a review, plasmonic nanoparticles [102-104] (NPs) provide an impressive way of light-matter interaction through localized surface plasmon resonances (LSPR) that can be excited, providing new means to manipulate light at scales much smaller than its wavelength. The applications of plasmonic NPs are numerous, including high-resolution microscopy [105], optical nanocircuits [106], nanoscale light transport [107], nonlinear optics [108], optical metamaterials [109,110], metasurfaces [111], electromagnetically induced transparency [112,113], spectroscopy and sensing [114], e.g. surface-enhanced Raman spectroscopy (SERS) [115], and plasmonic solar cells [116-119].

In photovoltaics, particularly, plasmonic NPs have opened a new way to obtain improved performance and achieve cost efficiency by introducing plasmonic mechanisms for enhancing the absorption of light [120-125].The third generation of photovoltaic device design could also benefit from these NPs, as they are being investigated in ultrathin solar cells [126], and microwire arrays [127]. The latter design has demonstrated promising potential to high performance devices, exploiting the increased surface-to-volume ratio of micro-wires and enhanced scattering of plasmonic NPs. Introduced most recently, excellent candidates for high efficiency solar devices are similar single and dual-junction semiconductor wires, but at nanoscales [128].

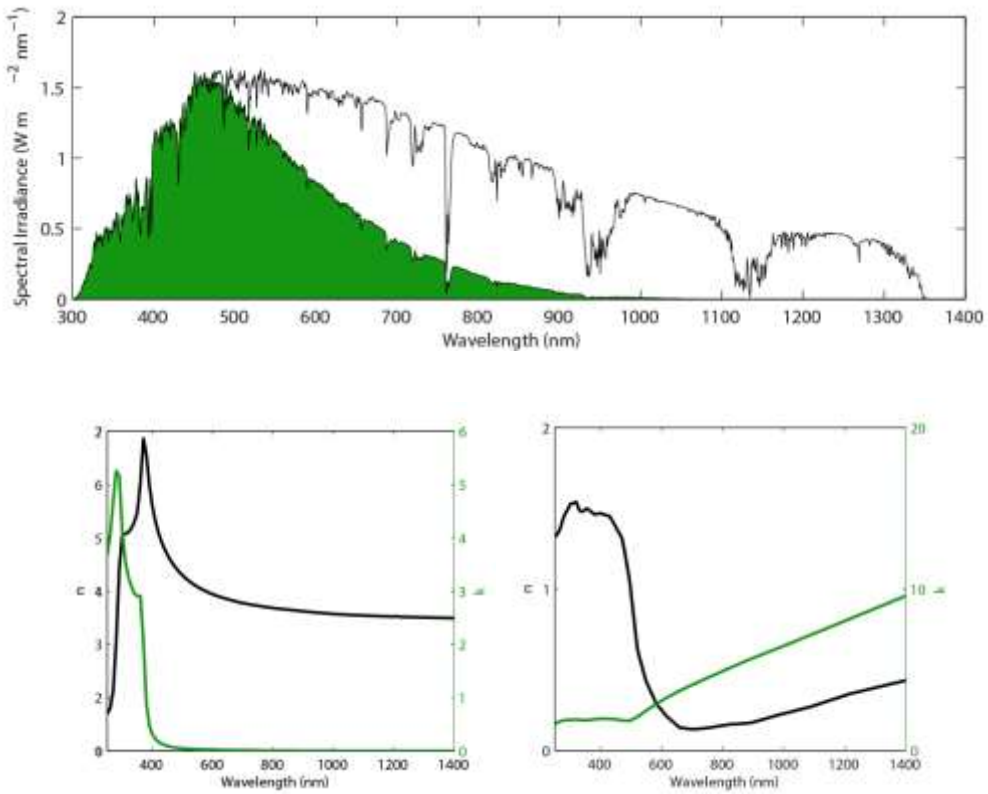


Figure 35: The standard AM1.5G irradiance spectrum of sunlight is plotted along with the absorption spectrum of a 2μm film of silicon with anti-reflection coating (the shaded area). On the bottom, the optical constants of gold (left) and silicon (right) is shown.

Nanowires (NW) provide the highest surface-to-volume ratio for interaction with light, and the minimum of the amount of material used in the device. With incorporation of engineered radial junctions [129], a near unity internal quantum yield can be achieved [128]. Utilizing a proper surface passivation, their performance can be improved since the surface recombination decreases [130]. The crystal phase can be tuned along the length of nanowires, giving the possibility of tuning the electronic properties [131]. When grown as nanowires, lattice mismatched materials can be integrated, enabling strain-free multi-junction solar cells and the utilization of cheap substrates [132,133]. The common method of NW growth is the vapor-liquid-solid (VLS) [134], which uses gold as a stable and non-oxidine catalyst. However, gold-free methods such as Ga-assisted selective area

epitaxy could be employed [135], assuming gold is an unwanted impurity with negative effects on the physical properties of NWs.

Coupling of the incident light in the NW is an important issue and it has been suggested that by effective collecting of light, NWs have the potential to overcome Shockley-Queisser limit [136]. In this regard, we show how to exploit the plasmonic properties of the gold catalyst to fold light into NWs. We investigate the different shapes of such NPs and find their role as dedicated nanoantenna elements serving each NW.

### 3.2.1. Approach

In the progress of studying the interactions and the effects of gold nanoparticles and their LSPR, the electrical and optical properties of the semiconducting nanowire should be taken into account, but for the sake of simplicity, we neglect to study the different materials of interest, and we concentrate more on the fundamentals of such studies.

Therefore, we assume the nanowire to be simply made of silicon. Other materials can of course be considered, as we have studied ZnTe in another work [137].The optical properties of both silicon and gold are shown in Figure 35. The potential candidates for use as the nanoantenna elements are as follows:

1. Sphere, which is the simplest form of nanoparticles. A sphere, however, is restricted by its shape and radius, which means that to tune the frequency of LSPR, it is required to change the radius of the sphere. This will provide limited functionality, yet the simplest and cheapest nanoantenna element.

2. Hemisphere, which has the same limitations of the sphere but with the positive feature that less metal will be used and the unwanted losses of energy due to the antenna material will be reduced.

3. Cylinder is a tunable nanoantenna which provides two parameters to tune; its radius and height. Thus a cylinder will be one of the best choices to be the attached to nanorods. The trade-off, however, is that the fabrication and growth of the nanorods with cylinders on top is more complicated, and costly.

4. Core/shell structure, which can be in the form of a spherical silicon core with gold shell. This nanoantenna can provide excellent tunability and flexibility by providing two radial parameters by which one can determine the size of the nanorod element as well as tune the resonant frequency of the system.

5. Non-plasmonic antenna, in the form of silicon or germanium nanospheres. The nanoantennas of this group can eliminate the attenuation effects present in the use of metallic nanoparticles and also improve the final electrical characteristics of nanorods after using growth methods such as VLS. The scattering of light in this case is caused by magnetic dipoles instead of electric dipoles of plasmonic nanoparticles and takes the form of Kerker scattering. As a reference to all of these nanoantenna elements, refer to Figure 36.

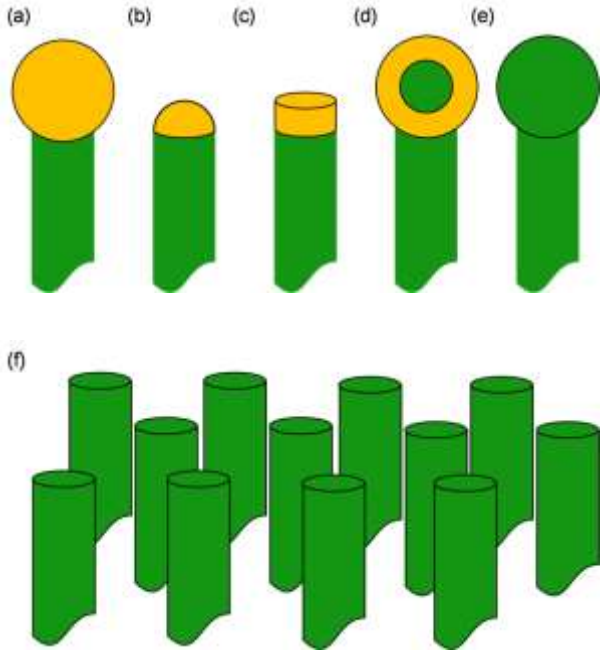


Figure 36: Schematics of single nanorod elements attached to nanoantennas (a) sphere, (b) hemisphere, (c) cylinder, (d) spherical core/shell, (e) non-plasmonic sphere. On the bottom, a drawing of the collection of nanorod elements is shown representing the surface of solar panel. Here the nanoantenna elements are not shown.

### 3.2.2. Results and Discussions

To obtain a measure of the energy absorbed in the semiconductor nanorods, we use frequency domain FEM to compute absorption and scattering cross-sections of nanoparticles as well as the energy lost in the nanorods. For future comparison, we compare the results of the computations of the above parameters with those of exact analytical approaches such as Mie theory for a spherical nanoparticle. That is, we compute the scattering efficiency and absorption efficiency for different sizes of gold nanospheres with both methods (Figure 37).

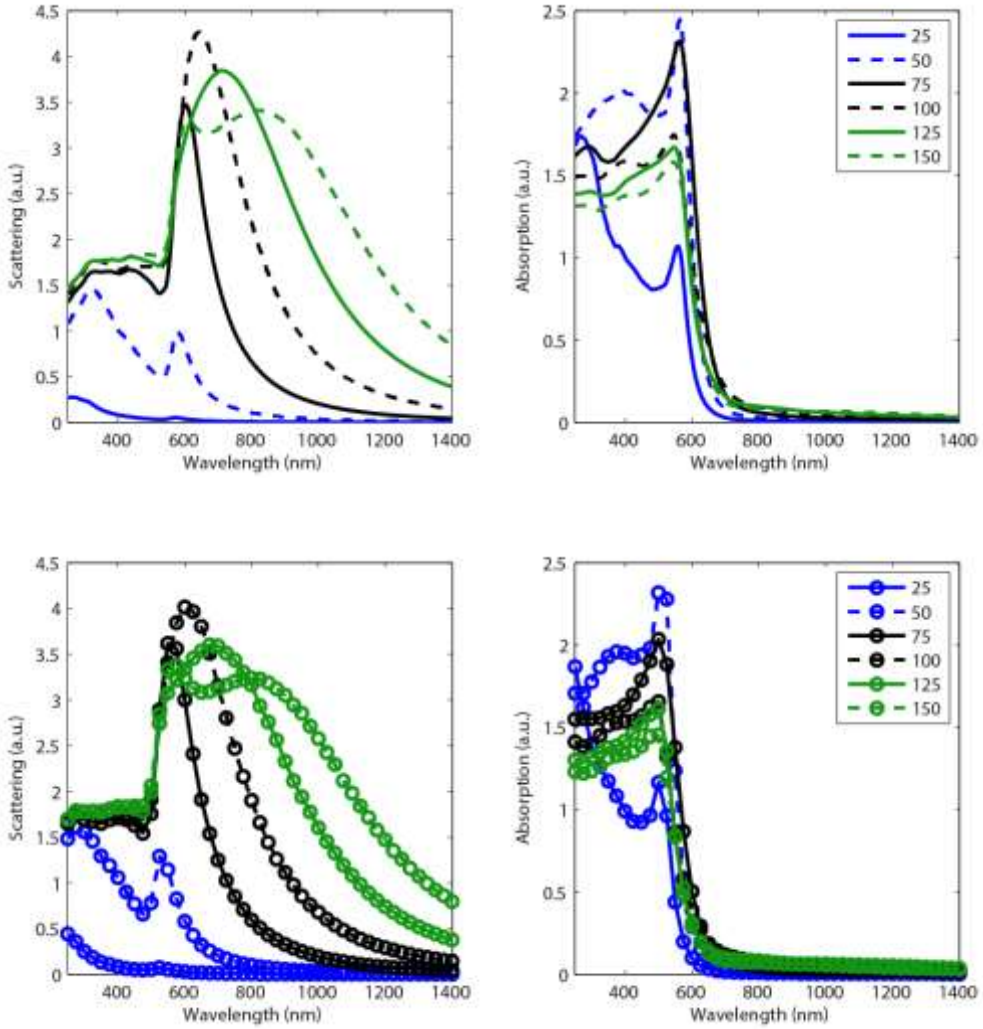


Figure 37: Spectra of scattering and absorption of light by spherical nanoparticles of gold: (top) calculation based on exact analytical Mie theory for 6 different sizes on spheres. The legend shows the radius in the units of nanometers. (bottom) same as (top) but using FEM.

A reasonable range for the size of nanorod elements is around 100nm. We investigate the smaller and larger values as well, limiting the study to the radii of 25nm to 150nm. The results of computations with exact analytical Mie theory and FEM show very good agreement (Figure 37). There is, however, a very slight shift in the peak of FEM computed spectra, which is negligible. But it can be assigned to the meshing of the sphere in the FEM environment, which is not as perfect as a complete sphere. Also, some of the

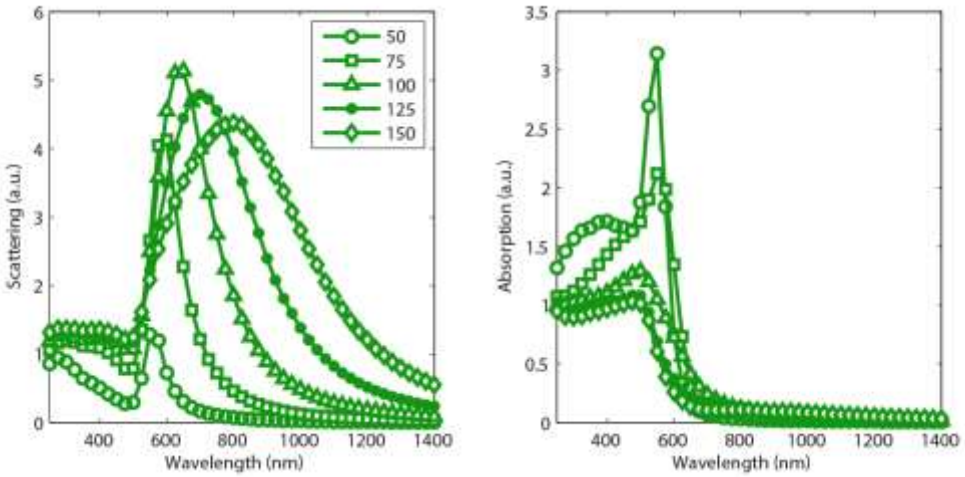


Figure 38: Spectra of scattering and absorption of light by hemispherical nanoparticles of gold using FEM. The legend shows the radius in the units of nanometers.

small features emerging from Mie theory could be missed in the FEM approach, since the frequency step size is larger in comparison to the analytical approach. An example of such issue can be found in the absorption spectrum of 25nm sphere (blue solid curve) as a little bump around 400nm (Figure 37).

In this work, we study the cases of hemisphere and cylinder. We obtain the antenna radiation pattern in both geometrical shapes and investigate its modification when attached to the nanorod structures. We then compute and compare the loss of sunlight in the nanorod prior and after the installation of nanoantenna elements. The optical properties of core/shell nanostructures and non-plasmonic antennas need more detailed studies and will be researched in another work. Further, it should be emphasized that here we only assume single nanorod elements and the interaction and the coupling between them is neglected. The interested reader can refer to our work on the ZnTe nanorods as an example of such studies [137].

For comparison of spectral and radiation characteristics of nanoantenna elements, we start with computing the scattering and absorption efficiencies of them based on different size and shape parameters. We start by studying the case of hemisphere. The hemisphere can be thought of as providing us with reduced attenuation. The results of computing scattering and absorption efficiency are plotted in Figure 38. It is immediately observable that the scattering is reduced at wavelengths shorter than about 500nm. Further, the peaks are slightly narrower, compared to the ones of spheres. Three other differences can be spotted compared to the spheres:

1. The efficiencies of both absorption and scattering are slightly increased.

2. There is also a slight blue-shift in the peak scattering resonance.

3. The secondary scattering resonance of larger spheres is absent in the spectrum of hemispheres with the same size (see the curve for 150nm in Figure 38). This can be the reason why the peaks of hemisphere are larger, since more energy couples only into one scattering mode in the dipole interaction.

Next, in the case of nanocylinder nanoantennas (Figure 36c), the study is more complicated since there is another free parameter in determining the geometrical shape. We have computed the spectral responses in a similar way as to the spheres and hemispheres, and the results are shown in Figure 39. The radii are 50nm, 75nm, and 150nm.

In each case, the height was tuned from 20nm to 100nm. The roles of radius and height of the cylinder in the optical features can be understood by analyzing the properties of each spectrum. One of the results is that the radius of the cylinder is the

main parameter determining the scattering peaks. The polarization of the incident light is along the diameter of cylinder; therefore, it is not surprising that the radius is playing the main role. Also, similar to spheres and hemispheres, a cylinder has the symmetry in its cross-section, but the interaction with light takes places at all the surface at the same time, and this distinguishes the cylinder from the other two. The height of cylinder is helping to fine tune the resonant frequency of the scattering and can be exploited for specific purposes in different applications. It is also found that the cylinder has a larger scattering efficiency compared to hemisphere, hence, larger than the sphere. It is also usual that by increasing the size of these nanoparticles, the absorption efficiency reduces. This can also be observed in all the curves plotted in Figure 39.

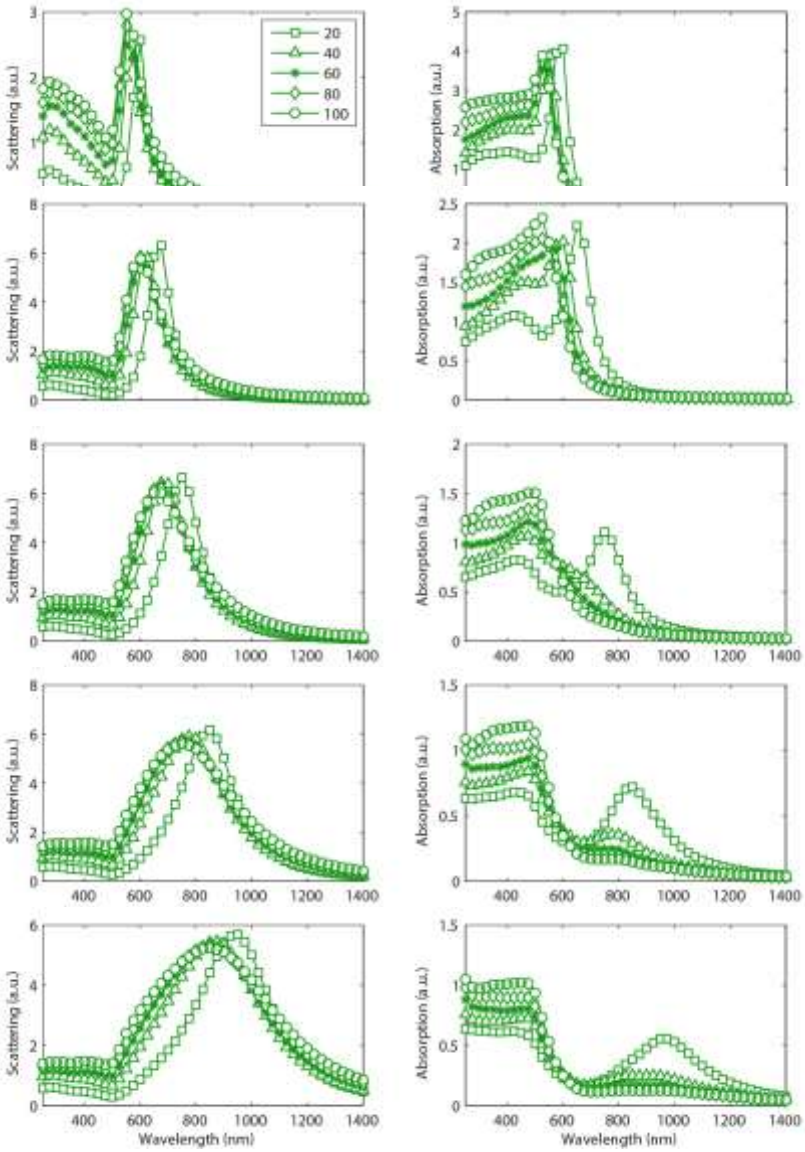


Figure 39: Spectra of scattering and absorption of light by cylindrical nanoparticles of gold using FEM. The radius of the particle is (top) 50nm, (middle) 75nm, (bottom) 150nm. The legend shows the height in units of nanometers.

Now, we attach these nanoantenna elements to Si-nanorods. The rod diameter is identical to the diameter of hemisphere or cylinder. The length of the rod is the same through all the studies and we have found that the effects of rod's length are not significant on the radiated pattern of the nanoantennas, unless the length is too short. We study the pattern radiated around the peak wavelength of scattering and absorption as

well as at the long and the short end of the spectrum. The obtained radiation patterns for a hemisphere of radius 50nm and a cylinder of radius and height 50nm are shown in Figure 40, Figure 41 and Figure 42, respectively. The patterns are plotted assuming the sunlight incident from the top on the nanoantenna element attached to a Si-nanorod underneath. Thus, the more radiation into the downward direction, the better the coupling and interaction of light with semiconductor material, hence leading to a more efficient absorption and performance of the solar cell. Studying all the radiation patterns from these nanoantennas at different wavelengths can help to find the more efficient designs when planning to plant groups of nanorods in the proximity of each other. That is, we can see that at some wavelengths the radiation pattern is not only downward, but also scatters strongly in directions that can be absorbed by another neighbor of the current element; examples of such patterns can be found in Figure 41(f,g), and Figure 42(f,g). The behavior of short wavelength response, which is similar in all two cases studied here is also interesting. At wavelengths shorter than the resonance, the scattered light tends to spread downward and along the polarization of light, but with some small portion of it being back-scattered. Figure 40b is a good example of such behavior.

The next step is to measure the absorption of light in the semiconductor nanorod. This can provide a point of reference to find the coupling effects of nanoantenna elements leading to enhanced near-field or resonant forward scattering. Also, as we have mentioned in the introduction, because of the geometrical shape and size of the nanorod, the absorbed light can be assumed to be converted completely to charge carriers. Therefore, the electrical parameters of a solar cell can be calculated at each frequency. It

should be noted that the total spectral response of the nanorod to the sunlight can also be studied with the use of finite different time domain (FDTD) approaches, in which a broadband incident light will be assumed and the electrical response includes the contribution of all the wavelengths. We will suggest a method to make similar measurements using FEM.

For the last remark of this section, we should emphasize that the absorbed spectra shown here assume a flat spectral input as the incident light. It is more insightful to apply the spectrum corresponding to AM1.5G and observe the results. Also, to better understand the spectral response of the nanoantenna elements to the sunlight, a weighted average over the scattering and absorption spectra is needed. In this way, the dominant antenna pattern, or the averaged equivalent of scattering pattern in response to sunlight will be achieved.

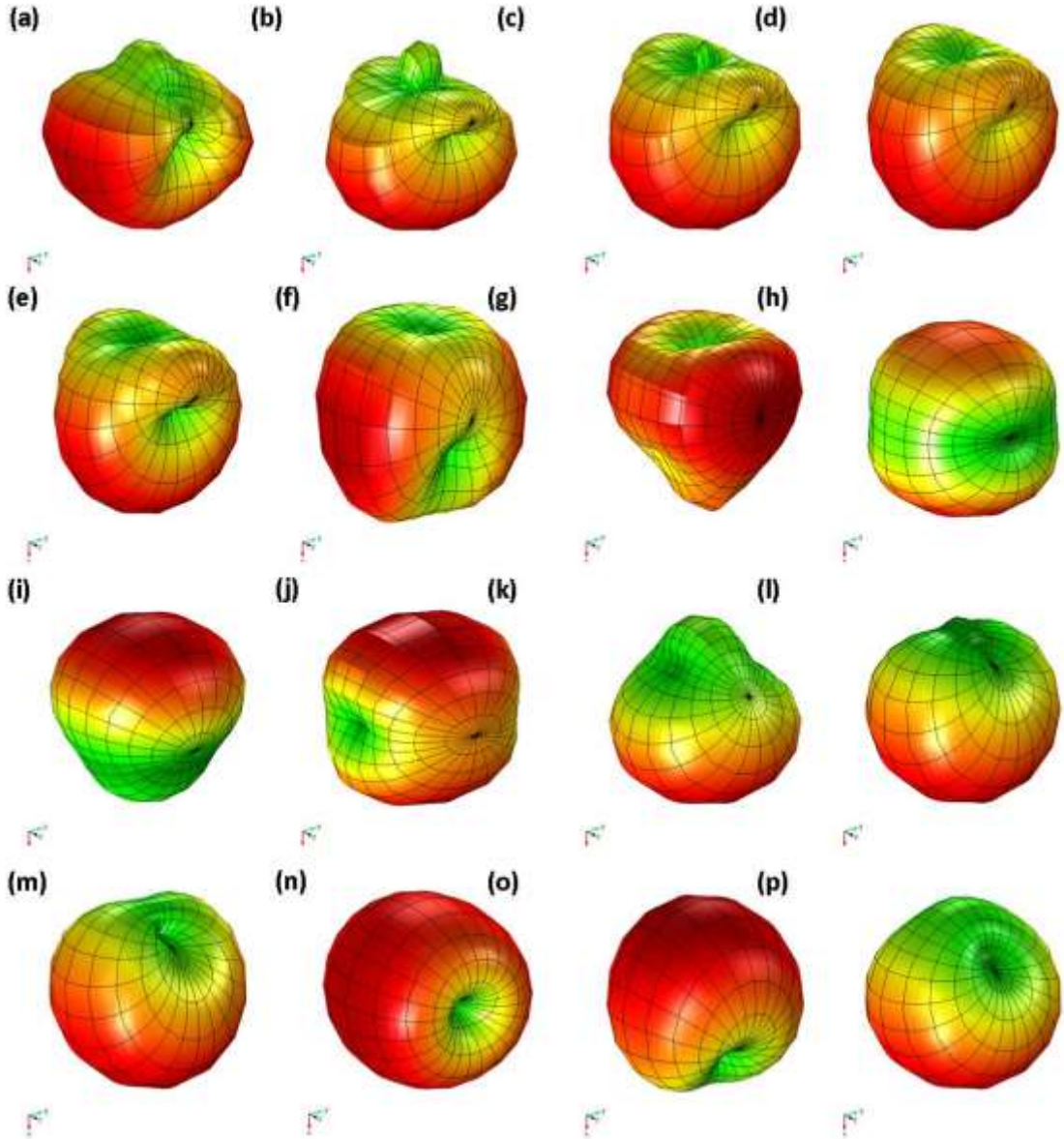


Figure 40: Radiation pattern of hemisphere of 50nm radius at different wavelengths (a) 300nm, (b) 325nm, (c) 350nm, (d) 375nm, (e) 400nm, (f) 425nm, (g) 450nm, (h) 475nm, (i) 500nm, (j) 525nm, (k) 550nm, (l) 575nm, (m) 600nm (n) 700nm, (o) 800nm, (p) 900nm. The axis along the length of the nanorods is parallel to x, and the polarization of light is along z direction.

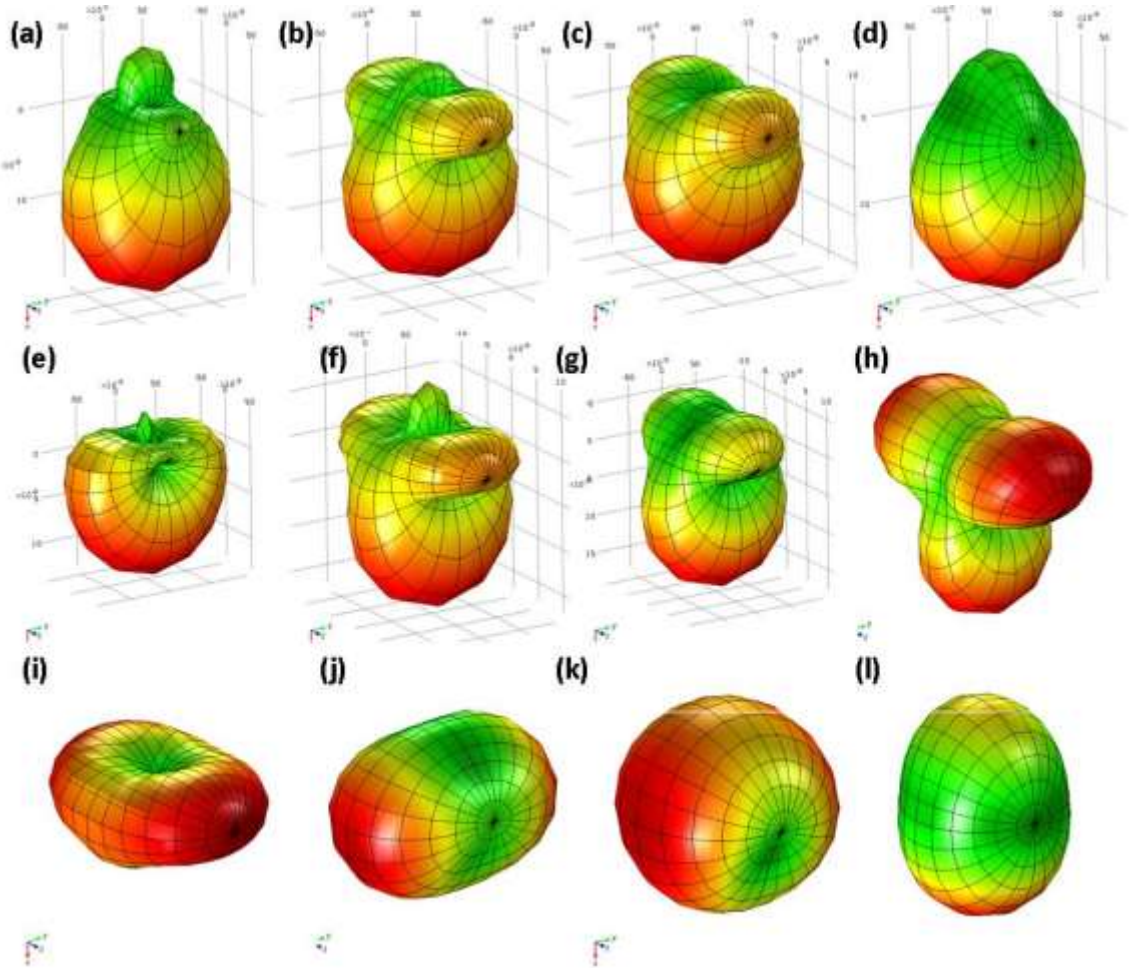


Figure 41: Radiation pattern of hemisphere of 100nm radius at different wavelengths (a) 300nm, (b) 325nm, (c) 350nm, (d) 375nm, (e) 400nm, (f) 425nm, (g) 450nm, (h) 475nm, (i) 500nm, (j) 525nm, (k) 550nm, (l) 575nm, (m) 600nm (n) 700nm, (o) 800nm, (p) 900nm. The axis along the length of the nanorods is parallel to x, and the polarization of light is along z direction.

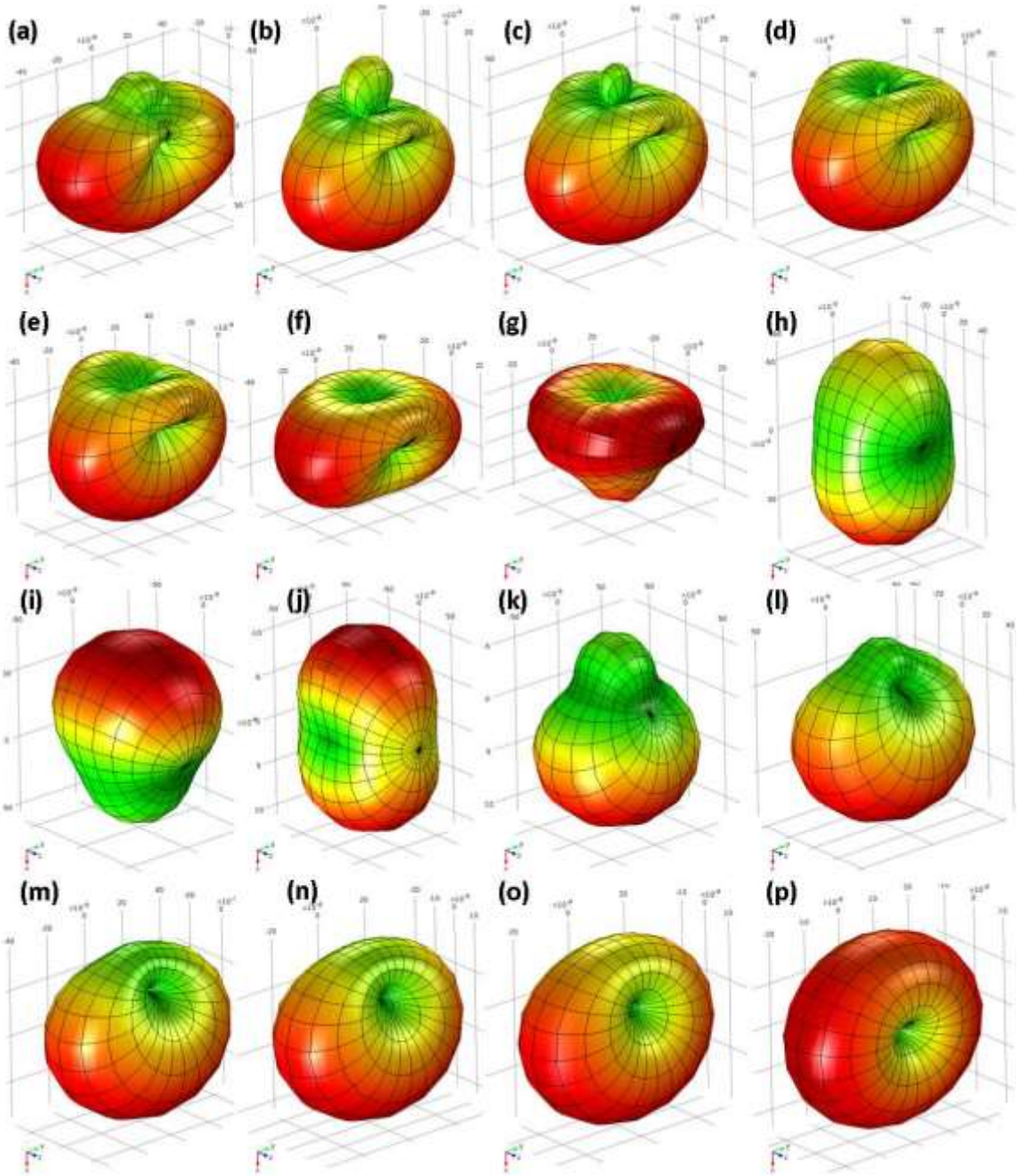


Figure 42: Radiation pattern of cylinder of 50nm radius and 50nm height at different wavelengths (a) 300nm, (b) 325nm, (c) 350nm, (d) 375nm, (e) 400nm, (f) 425nm, (g) 450nm, (h) 475nm, (i) 500nm, (j) 525nm, (k) 550nm, (l) 575nm, (m) 600nm (n) 625nm, (o) 650nm, (p) 700nm. The axis along the length of the nanorods is parallel to x, and the polarization of light is along z direction.

## 3.3. Radiation of Nanoantennas for Nanowire Photovoltaics

In this section, we only consider the use of plasmonic nanoantenna elements, hemispherical and cylindrical, for application in semiconductor nanowire (NW) vertical arrays. Using Mie theory and a finite element method, scattering and absorption efficiencies are obtained for the desired enhancement of interaction with light in the NWs. We find an optimal mixture of nanoantennae for efficient scattering of solar spectrum in the NW array. Spectral radiation patterns of scattered light are computed, and, for representing the total response of the nanoantenna-equipped NWs to the solar AM1.5G spectrum, the weighted average of scattering patterns for unpolarized normal incidence is obtained showing an advantageous overall directivity toward the NWs

As a quick reminder, plasmonic nanoparticles [138,139] (NPs) utilize localized surface plasmon resonances (LSPRs), providing the means to manage the light at scales much smaller than its wavelength. This is why there are many applications for plasmonic NPs, including optical nanocircuits [140], metasurfaces [141], high-resolution microscopy [142], optical metamaterials [143,144], electromagnetically induced transparency [145], surface-enhanced Raman spectroscopy [146], and plasmonic solar cells [147-150].

In the realm of thin-film photovoltaics, these NPs have revealed novel ways for cost efficiency and improved performance through plasmonic mechanisms enhancing the light absorption [151-154]. The design of next generation photovoltaic devices, e.g., ultrathin solar cells [155] and microwire arrays [156], also benefit from NPs. The latter design has a promising potential for higher performances, exploiting, in addition, the increased

surface-area-to-volume ratio (SA:V) of microwires. Very recently, excellent candidates have been introduced for high efficiency photovoltaic devices, which are still wires of semiconductor materials but at nanoscale dimension [157].

Nanowires (NWs) provide a higher SA:V (compared to microwires) for interaction with light, and when grown from semiconductors, lattice mismatched materials can be integrated, enabling strain-free multi-junction solar cells and the utilization of low cost substrates [158]. Other possible advantages of NWs include: control of crystal phase along their length for tuning the electronic properties [158], decreased surface recombination through a proper surface passivation [159], and near unity internal quantum yield by incorporation of engineered radial junctions [160]. Offering advanced light trapping, higher quality and defect-free material, NWs are shown to have the potential to overcome the Shockley-Queisser limit. [161]

In this section, we investigate the use of plasmonic NPs, as nanoantennas, attached to semiconductor NW arrays for application in photovoltaics. General considerations of nanoantennas, regarding their shape, are as follows (see Figure 43):

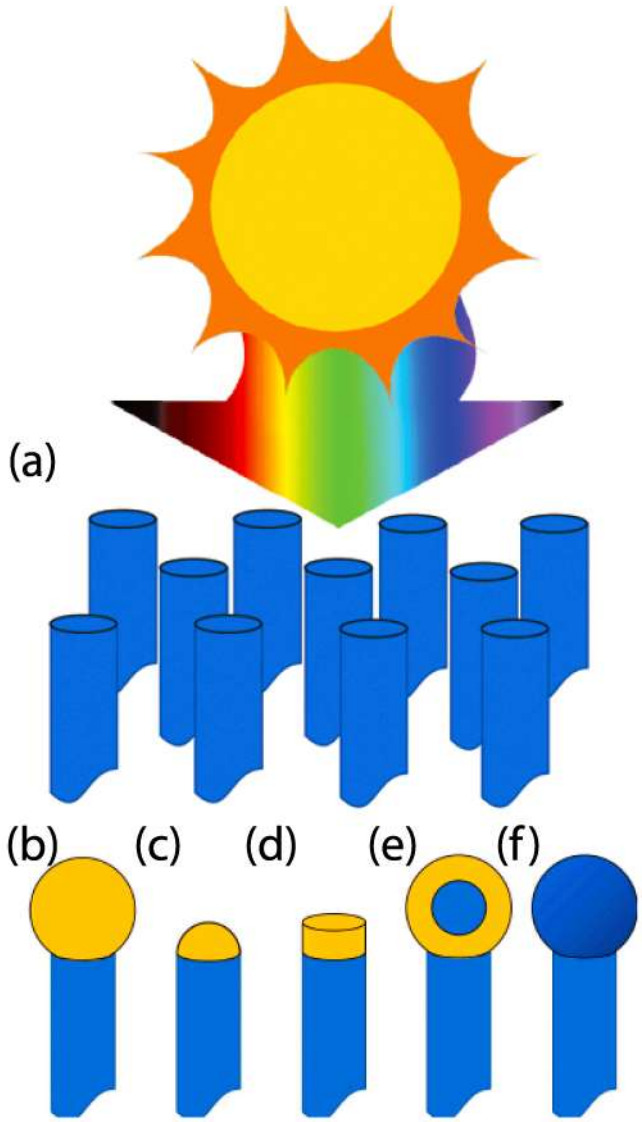


Figure 43: (a) Schematic of a solar device comprised of arrays of vertical NWs. (b)–(f) nanoantenna elements with different shapes and materials attached on top of NWs.

A sphere is probably the easiest to study and fabricate, with its radius as the only control parameter to tune the frequency of LSPR. A hemisphere has the same limitations of the sphere, while less metal is involved to cause losses. A cylinder is a more tunable nanoantenna, providing two control parameters (radius and height), however, the fabrication and growth of the nanorods with cylinders on top might be harder. Core/shell

spherical nanoantennae, e.g., silicon core with gold shell can comparatively provide more tunability with two radial control parameters determining the strength of plasmon coupling and LSPR wavelength. Non-plasmonic nanoantenna equivalents of mentioned geometries are also applicable, with the advantage that absorption losses reduce significantly. Kerker scattering and magnetic dipoles in this case can lead to superdirective nanoantennas [162]. We use exact analytical expressions of Mie theory [163] for calculation of scattering and absorption efficiencies of a spherical plasmonic NP. This provides two advantages. First is to elucidate the different phenomena in the interaction of light with the nanoantenna element with the polarizability α described earlier in the chapter.

The second advantage is the use it as the benchmark for computational purposes of other complex shapes in a fullwave FEM simulation environment. Compared to the analytical solution for the spheres, there is a slight shift in the FEM computed spectra, which might be due to the meshing of the curved surfaces in the FEM environment. The computed scattering and absorption efficiency for different sizes of hemispherical nanoantenna (Figure 43(c)) are plotted in Figure 44. It is immediately evident that the scattering is reduced at wavelengths shorter than about 500 nm. The behavior of these computed plots are in good agreement with our expectation when increasing the size of the NPs.

### 3.3.1. An Effective Mixture

To effectively interact with the solar spectrum, a mixture of nanoantennas can be used such that the total scattering spectrum fits well to the incoming sunlight. For simplicity,

we only consider a mixture of three sizes of hemispherical antennas with radii of 50 nm, 100 nm, and 150 nm, having the mixing percentages of 52.86%, 15.71%, and 31.43%, respectively, and surface coverage of 70%. The resulting spectral coverage is shown in Figure 44(c). This simple mixture leads to an accumulative coverage of 78%, which, from a total sunlight flux of 891W/$m^2$, results in an availability of 692 W/$m^2$. Yet better mixtures with multiple nanoantennas of different sizes and shapes can be obtained using Brent's method [164] or by global optimization methods such as the Genetic Algorithm. For such a purpose, the optical properties of other nanoantennas introduced here should be obtained. Nanoantennas of cylindrical shape (Figure 43(d)) provide more spectral tunability. However, we limit the study to the spectral responses for radii of 50 nm, 100 nm, and 150 nm, shown in Figure 45. In each case, the height is tuned from 10 nm to 100 nm. The radius and height of the cylinder have different effects on the optical features; the former is the main parameter determining the scattering peaks, while the latter acts as a fine tuning control. The underlying reason is that the polarization of incident light is along the diameter of cylinder; therefore, the radius is playing the main role. Also, similar to hemispheres, a cylinder has symmetry in its cross-section, but the interaction with light takes place on the entire surface at the same time, and this distinguishes the cylinder from the other two (hemisphere and sphere), providing reduced retardation effects at larger sizes. The cylinder can offer a larger scattering efficiency compared to a hemisphere which is larger than the sphere too. The scattering bandwidth is increased with the radius of the hemisphere and cylinder, making them fit better to cover the solar spectrum. One example of such fitting is shown in Figure 44(c), for the hemispherical nanoantennas.

The emission patterns of nanoantennas when attached to Si-NW are investigated in the following. The diameter of the NW is identical to the diameter of the attached hemisphere or cylinder. Also, the length of the NW is the same through all the studies, and we have found that the effect of this parameter is not significant on the radiated pattern of the nanoantennas unless it is shorter than half a wavelength. The treatment here obtains the radiation patterns over the solar spectrum; a wavelength range from 250 nm to 1400 nm. In Figure 46a-d, the radiation patterns for a cylindrical nanoantenna of a height 25 nm and radius of 50 nm are shown at four different wavelengths. The patterns are plotted assuming the sunlight incident from the top on the nanoantenna element attached to a Si-nanorod underneath. The difference in the radiated features as the wavelength varies is obvious.

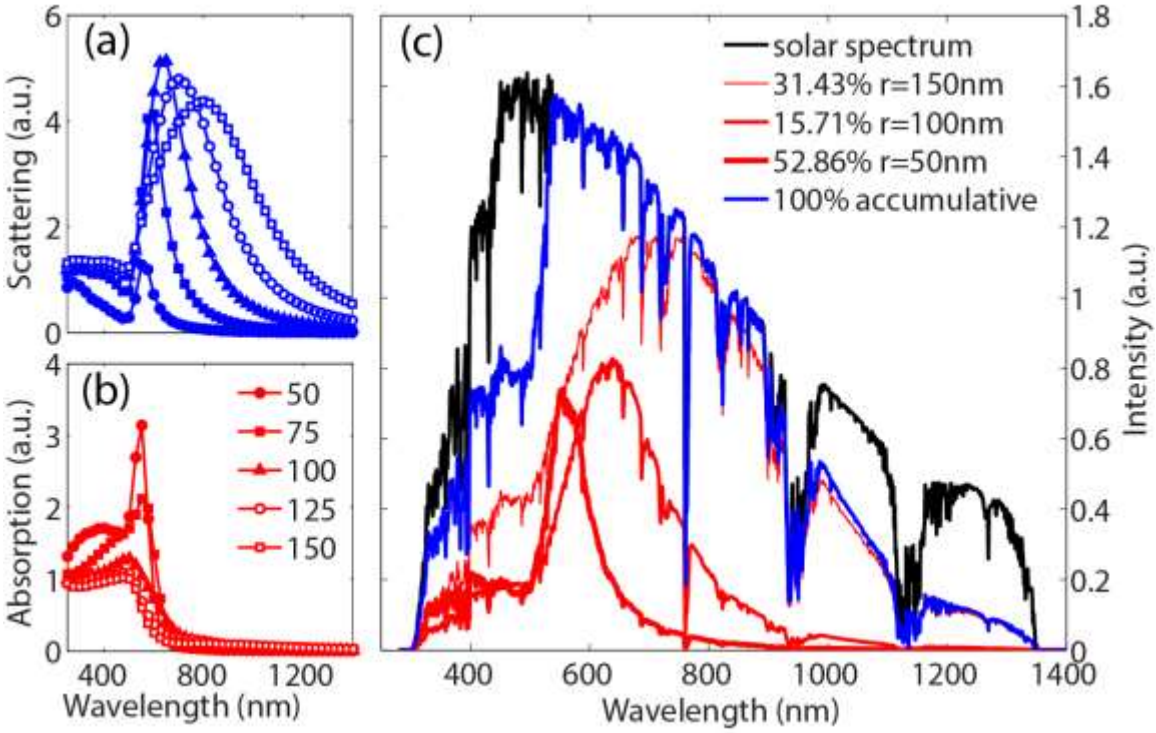


Figure 44: Scattering (a) and absorption (b) efficiency of hemispherical nanoantennas of different radii (in nm scale). (c) Solar spectral irradiance (AM1.5G), and coverage of solar spectrum scattered by mixing three sizes of hemispherical nanoantennas each obtained after multiplying with the NP efficiency.

### 3.3.2. Radiation Pattern Averaging

To be more realistic, one should note that all the wavelengths in the solar spectrum arrive at the nanoantenna simultaneously. An approximate response of the system can be obtained by taking the average over the wavelengths. However, for more accuracy, it should be considered that the wavelengths have different intensities and also the response to each wavelength in the nanoantenna is different.

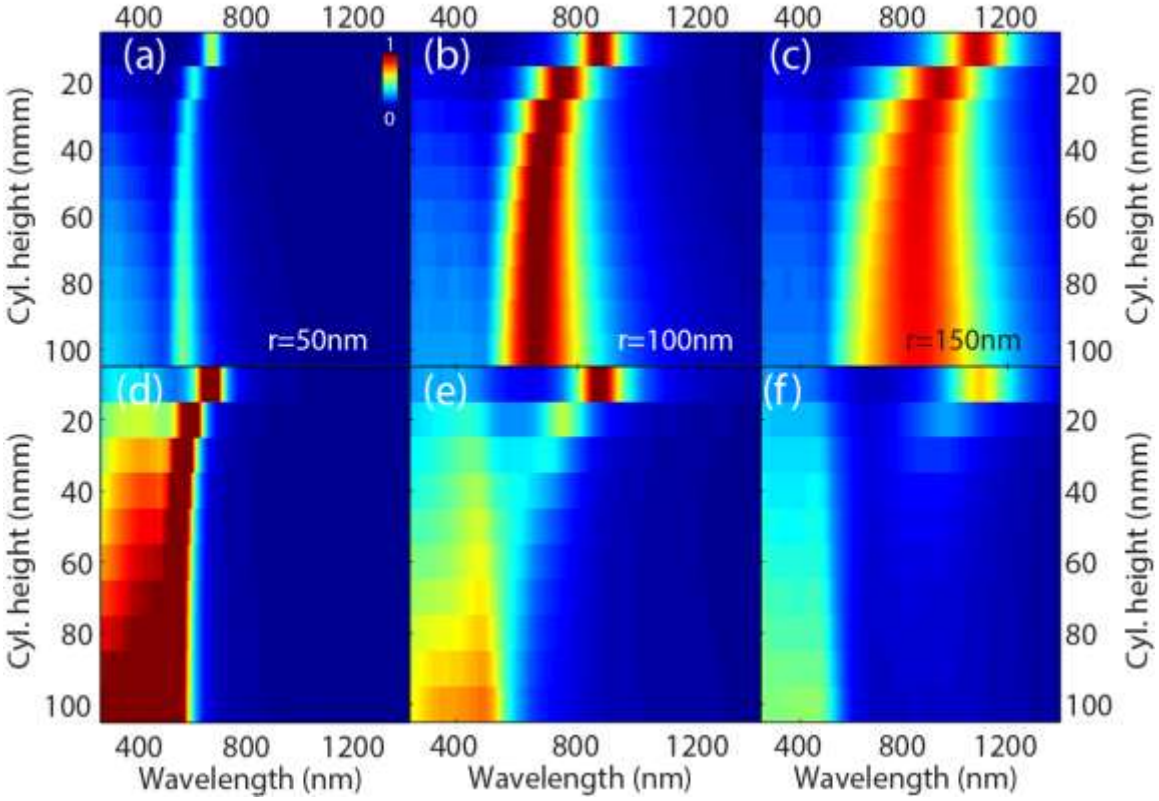


Figure 45: Scattering (a)–(c) and absorption (d)–(f) of cylindrical nanoantenna elements with different radii and height. Scattering plots have been shown scaled identically, and absorption plots are scaled to one-third of scattering scale.

Therefore, the total response is an integration of all responses weighted by the photon flux of sunlight:

$$\iint_{0,\lambda_1}^{4\pi,\lambda_2} d\Omega d\lambda \{\Psi_{NP}(\lambda,\Omega)\Phi_{AM1.5G}(\lambda)Q_{sca}(\lambda)\}, \tag{44}$$

where $\Psi_{NP}$ represents the antenna pattern of the NP, and $\Phi_{AM1.5G}$ is the normalized photon flux of the solar spectrum at AM1.5G. We have multiplied the photon flux by the scattering efficiency of the nanoantenna to obtain a good measure of the increased photon flux due to the presence of the NP. This is the number of photons "efficiently" incident on an attached NW. Besides, note that the emission patterns could be different in the

directions parallel and perpendicular to the plane of polarization, as we have depicted in Figure 46(a) and (c) (for parallel) and Figure 46(b) and (d) (for perpendicular).

Furthermore, since sunlight is generally unpolarized, we should also take the average of both polarizations for a more accurate estimation. We observed that when averaging over the responses using Eq. (44), the final pattern smoothes out in favor of a dominant pattern, which is the pattern with the most overlap between the LSPR and the photon flux spectrum. The results are shown in Figure 46(c) for 100 nm, 75 nm, and 50 nm radii of the cylinder at the height of 25 nm. The inset of Figure 46(c), illustrates the 3-dimensional (3D) averaged pattern for the cylinder of radius 50 nm and height 25 nm. It can be inferred that (i) the smaller cylinder shows more directionality toward the NW, (ii) the larger the cylinder size, the larger its radiation pattern in terms of intensity and angular spread, and (iii) also, the weighted average of the radiation patterns is quite similar to the pattern of the LSPR wavelength.

According to this, it is then straightforward to predict the 3D averaged patterns for other nanoantennas. As two other examples, we have depicted the patterns for a cylindrical nanoantenna (r = 50 nm, height = 50 nm) and a hemispherical nanoantenna (r = 50 nm) in Figure 47(a) and (b), respectively. Comparing the patterns to each other suggests that the radiation patterns of these small nanoantenna elements are similar when averaged over the solar spectrum and their differences lie in their LSPR frequencies, which are dependent on the shape, size, and other parameters. The resulting averaged pattern could be very useful in the design of NW elements when choosing the length of NWs and the spacing in-between.

One might also consider the electrical and optical properties of the semiconducting NWs in Eq. (44), but for the sake of phenomenological study only Si-NWs have been assumed throughout this work. However, note that the absorption coefficients of common semiconductors are similar in the spectral region of interest. As a related remark, it is also worth mentioning NWs of ZnTe (Eg=2.24 eV) attached with spherical gold nanoantennas have been studied in another work [165]. The absorption of light in the NWs has been studied theoretically [166] and experimentally [167], to which the interested reader is referred for further details. Investigations on core/shell NPs for use in absorption and emission of light are also available [168].

On fabrication, vapor-liquid-solid (VLS) deposition[169], which uses gold as a stable catalyst, is commonly used to grow NWs. Gold-free methods, such as Ga-assisted growth [170], for higher quality of material, assuming gold is an unwanted impurity degrading the electrical performance of NWs by creating deep-level traps have been suggested. Selective-area growth method has also been demonstrated for synthesis of GaAs, GaP, InP, and InAs NWs without the use of Au or Ga catalysts [157].

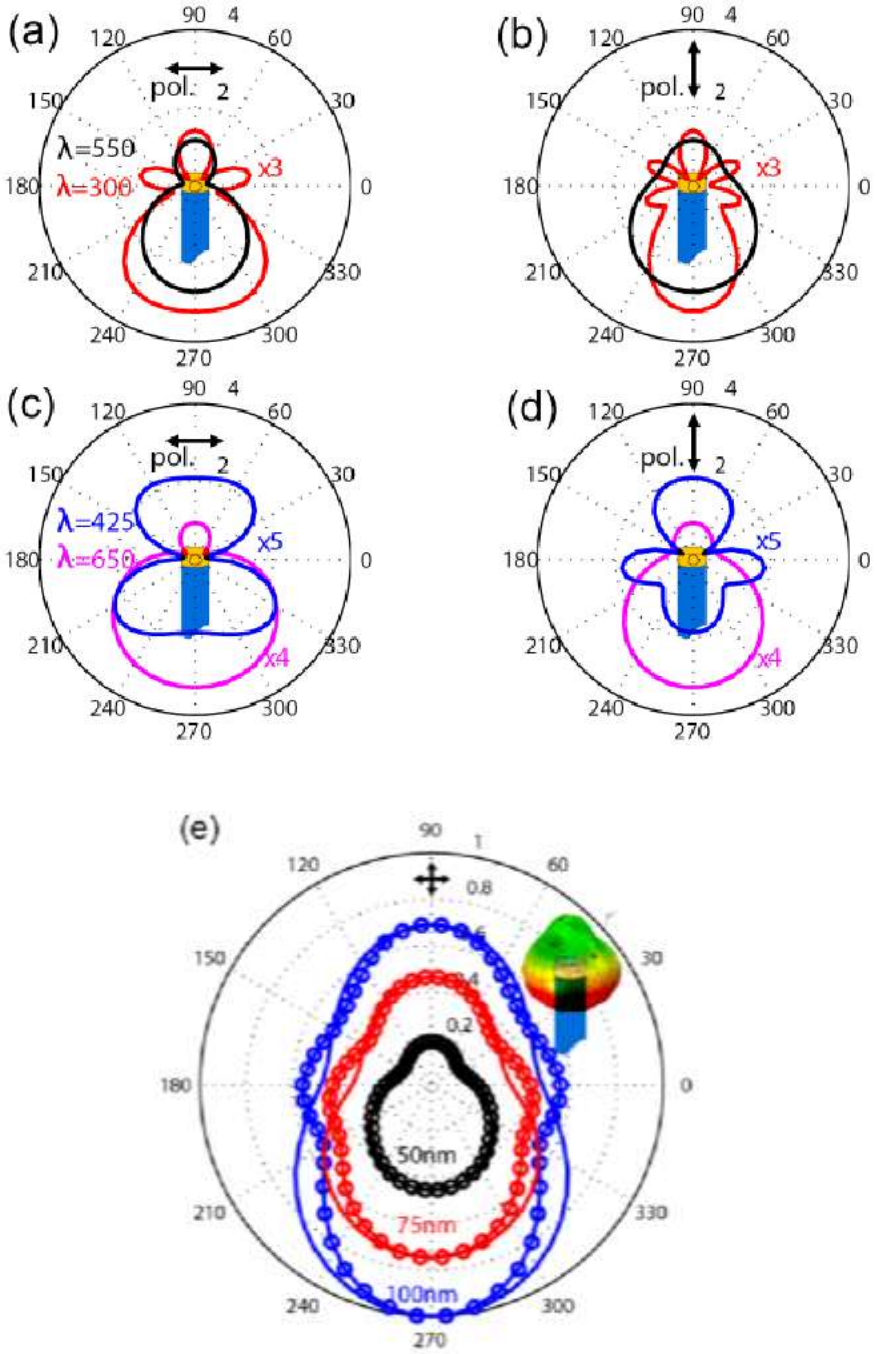


Figure 46: The radiation patterns for a cylindrical nanoantenna of a height 25 nm and radius of 50 nm at four different wavelengths. (a) and (c) Radiation along the polarization of incident light, (b) and (d) radiation perpendicular to the polarization of incident light. (e) Averaged radiation pattern for different sizes (r = 50 nm, 75 m, 100 nm; height = 25 nm) of cylindrical nanoantennas. Solid lines and markers (circles) show the two polarization dependent responses. (inset) 3D illustration of the radiation.

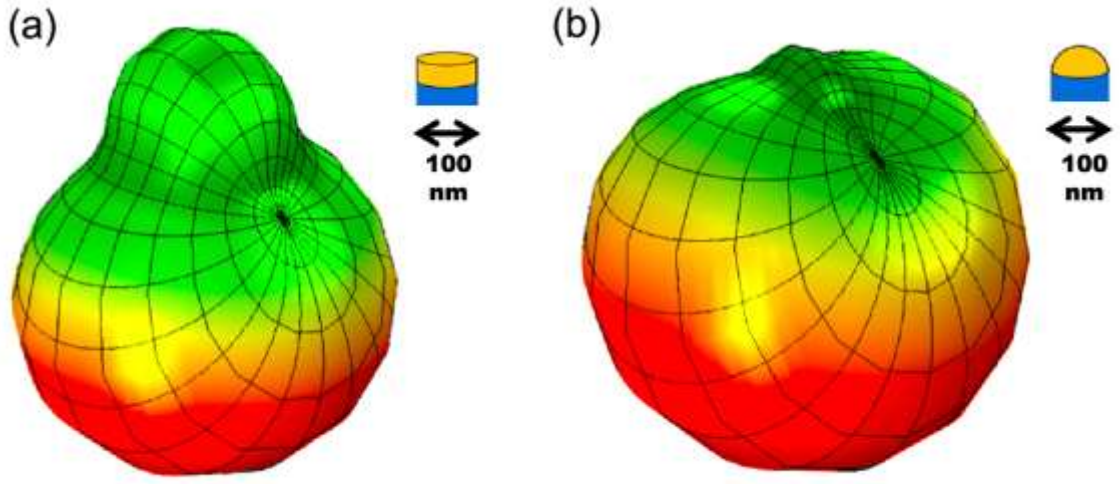


Figure 47: The predicted 3D radiation patterns for (a) cylindrical nanoantenna (r = 50 nm, height = 50 nm), and (b) hemispherical nanoantenna (r = 50 nm).

In conclusion, we have investigated the use of plasmonic hemispherical and cylindrical nanoantennae for vertical arrays of NW, using Mie theory and FEM. We have found an optimal mixture of nanoantennae for efficient scattering of the solar spectrum in the NW array. Other possible mixtures can be obtained from the results presented here. Spectral radiation patterns of scattered light are computed. The total response of the nanoantenna-equipped NWs to the solar AM1.5G spectrum is obtained by the weighted average of scattering patterns for unpolarized light. We observed that the final averaged pattern is smoothed in favor of a dominant pattern, which is the pattern with the most overlap between the LSPR and the photon flux incident spectrum. The result could be very useful in the design of NW elements when choosing the length of NWs and the spacing in-between.

## 3.4. Dielectric Nanoantennas

Next, we are going to find the absorption increase using nanoantennas. Here we only look at the dielectric structure as an example. We investigate photovoltaics incorporating standing nanowire arrays of silicon using a full wave FEM computational approach. The interaction of sunlight with bare nanowires and also with nanowires attached to dielectric nanoantennas is studied. We compute the absorption spectra in each case and compare the results to determine a possible optimal mixture of nanowire-nanoantenna elements for solar applications. We also investigate further the enhancement of absorption by exploiting field intensity patterns within the nanowire arrays. The results illustrate the benefits of using dielectric nanoantennas for applications in nanowire solar cells.

### 3.4.1. Introduction

For conversion of sunlight, there are two important steps to be performed efficiently; absorption of photons and extraction of photocurrent. There have been numerous studies on increasing the effectiveness of these mechanisms. Semiconductors are used extensively as the one type of material for this conversion procedure, among them silicon, being plentiful on earth and also cheap, is the favorite material. We consider how to maximize the aforementioned efficiencies.

The simplest design of a solar cell can be assumed to be a micron-sized silicon layer for which an anti-reflection coating is included to help trap light inside the layer thereby enhancing the absorption. More advanced light trapping techniques can be included to facilitate multi-wavelength light trapping, such as surface patterning. The ideal case is a broadband absorber for wavelengths in the range 250nm to 1500nm, consistent with the

black body emission of 5800K of the solar spectrum at Air Mass 1.5 Global (See Figure 48.a). This design could have a better electrical performance as well if the silicon layer was thinner in order to avoid recombination of generated electrons within the material. But there will be then a trade-off with the light absorption, according to Beer's law, as the thickness decreases. Therefore, other light trapping schemes have been suggested for use with thin-film solar cells, including plasmonic-assisted light trapping for folding light into the semiconductor layer through localized surface plasmon resonances [171-176].

There is however a fundamental barrier in increasing the efficiency of the light conversion. The Shockley-Queisser limit is defined as the maximum theoretical efficiency of a single junction solar cell. It is dictated by the thermodynamics of the solar energy conversion into electrical work and defines a limitation on the open-circuit voltage ($V_{oc}$) of the device:

$$V_{oc} = \frac{E_g}{q}\left(1 - \frac{T}{T_{sun}}\right) - \frac{kT}{q}\left[\ln\frac{\Omega_{emit}}{\Omega_{sun}} + \ln\frac{4n^2}{C} - \ln QE\right] \quad (45)$$

where $E_g$ is the bandgap energy, $q$ is the unit charge, $T$ and $T_{sun}$ are the temperatures of the cell and of the sun respectively, $k$ is Boltzmann's constant, $\Omega_{emit}$ and $\Omega_{sun}$ correspond to the solid angle of emission and collection, $n$ the refractive index of the material, $C$ is the light concentration factor, and $QE$ is the emission quantum efficiency. The first term on the right is related to the Carnot efficiency, which reduces $V_{oc}$ by ~ 5%. Three entropy-related terms are in the brackets. The first term represents the entropy increase through spontaneous emission. Thus, limiting the angle of radiative emission into a solid angle approaching $\Omega_{sun}$ avoids a large fraction of this entropic energy loss. The second

term describes the effect of incomplete light trapping, with $C$=1 for no light trapping and $C$=4$n^2$ as the classical ray optical limit. The last term is the loss due to non-radiative exciton recombination, which occurs because of crystallographic defects, impurities and other carrier traps in the bulk, at interfaces and at the surface.

Two of the approaches to overcome this fundamental restriction include i) tandem solar cells [177], in which multi-junctions of various materials are incorporated into the solar cell, and ii) non-planar solar cells [178,179], which is a form of wire array for the solar material. Tandem solar cells have shown good conversion efficiencies but their cost and fabrication are the current challenges in commercializing them. On the other hand, nanowire arrays have demonstrated promising potential for high-performance devices, exploiting the increased surface-to-volume ratio of micro-wires and enhanced scattering when coupled with plasmonic nanoparticles. More recently, nanowires (NW) have attracted much attention by providing a higher surface-to-volume ratio for interaction with light, while minimizing the amount of material used in the device. With the incorporation of engineered radial junctions, a near unity internal quantum yield can be achieved, therefore their electrical performance is enhanced. Also utilizing a proper surface passivation, their performance can be improved since the surface recombination decreases. The crystal phase can be tuned along the length of nanowires, giving the possibility of tuning the electronic properties. When grown as nanowires, lattice mismatched materials can be integrated, enabling strain-free solar cells and the utilization of cheap substrates. Therefore, using NWs for advanced light trapping, higher quality and

defect-free material will be required. A schematic of such a NW array is shown in Figure 48.b.

Plasmonic [180] nanoparticles have been widely used as the nanoantenna elements for such a NW array. That is, they can be used in conjunction with each NW in order to provide enhanced light-matter interaction with the NW through increased scattering efficiency. The scattering properties of small particles have been studied in detail in the literature. The nature of scattering from plasmonic particles results from their electric dipole moment when illuminated by light. Apart from plasmonic particles, dielectric particles also show resonances in their scattering behavior which is recognized as Kerker scattering. This type of scattering is due to the magnetic dipole in the dielectric nanostructure, which here, in our context, is a dielectric nanoantenna. We now study the effects of such spherical dielectric nanoantennas when attached on top of silicon NW arrays.

We employ a fullwave finite element method to design the geometry of the solar structure. First we design one of the NWs in the design environment and then, after assignment of material properties, we impose the Floquet periodic boundary conditions on the walls of unit cell to mimic an infinite surface filled with NWs (Figure 49b). Light is incident from the top of the unit cell, simulating the sunlight. Here we only consider a flat intensity spectrum as opposed to the real irradiance of the sun (refer to Figure 48a) to be able to observe if there is any interesting phenomenon in the interaction of different wavelengths of light with the nanocomposite structure (i.e. NW + nanoantenna).

(a)

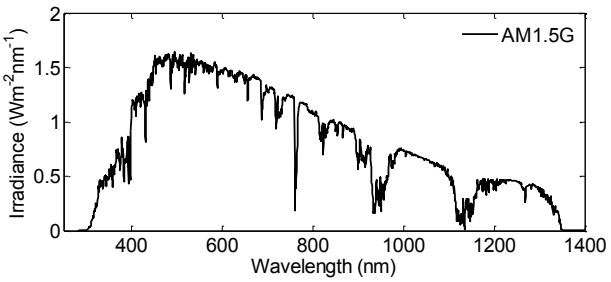


(b) (c)

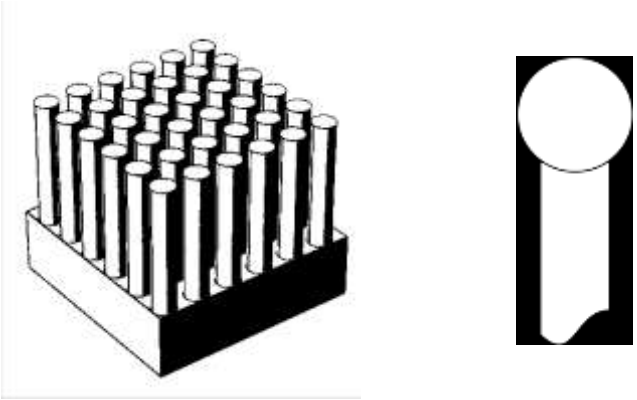

Figure 48: (a) Solar spectrum, (b) nanowire standing array, (c) a single NW with a spherical dielectric nanoantenna on top.

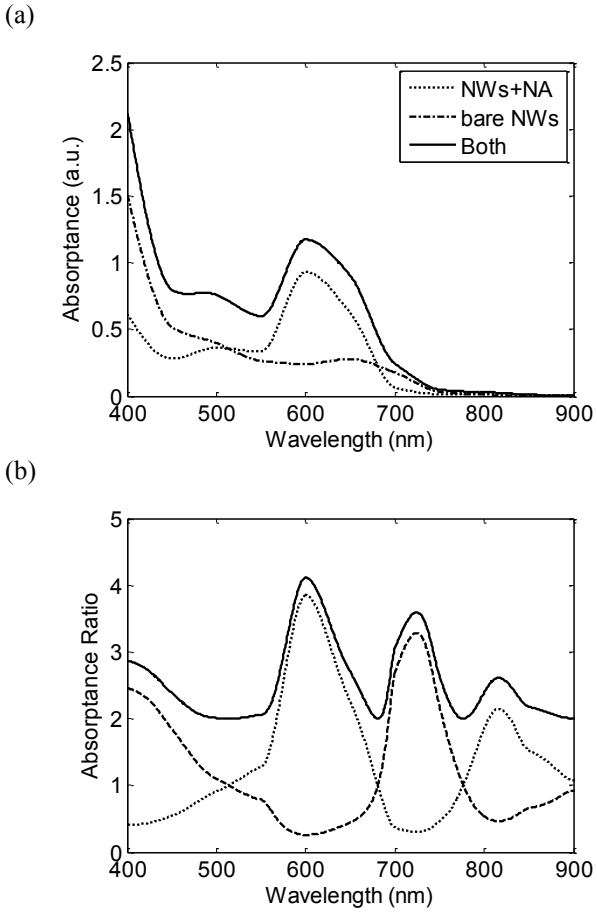


Figure 49: (a) Plots of absorption in the NW arrays with and without nanoantennas (NA) and a mix of both; (b) ratio of the absorptions in (a). The horizontal axis is wavelength in nm.

First to obtain a reference point to quantify the enhancement, we obtain the absorption in the nanowires without nanoantennas attached. It should be noted that the spacing and the length of the NWs will have an effect on the light coupling into the array structure, as we have shown in another publication [182]. Here we consider silicon NWs having a diameter of 130 nm and center-to-center spacing of 260 nm. After computation of this baseline for NW array absorption, spherical dielectric nanoantennas of silicon are considered on top of the NWs. We performed the computation under these new conditions. The results are shown in Fig 2a. Clearly, after attachment of the dielectric

nanoantennas, the absorption of bare NWs is enhanced in the wavelength range 500nm to 700nm, which from the solar spectrum is the peak incident intensity, and because of being in a longer wavelength range more material would be required in the planar solar cell. Therefore, one can see the benefit of using the nanoantenna elements. We have also depicted the absorption ratio of the two cases in Figure 49b. This is useful to find the spectral regions where the dielectric nanoantenna is more efficient than the bare NW. One can use this information for optimizing the mixture of NWs and nanoantennas to be able to have an overall increased absorption in the total structure. The mixture plotted in Figure 49b is 50-50. It should be noted that the short wavelength absorption in the NW array with attached nanoantennas is reduced compared to the bare case. The reason for this could be an enhanced resonant absorption in the nanoantenna itself, or its scattering properties such that the light is scattered off the NW instead of being coupled into.

To better understand the increase in the overall absorption, the absorption maps within the nanowires in each of the two cases are obtained, as shown in Figure 50, for the wavelengths of enhanced absorption. Light is incident from the left side of the NW with vertical polarization, that is to rotate the standing geometry for 90°. The bare NW are on the left panel and those with attached antennas in the right (nanoantennas are not shown here) Increased field intensities inside the NW are clearly observed after attachment of the nanoantennas. The field intensity patterns inside the NW are being effectively fed with the incident light through the nanoantenna element.

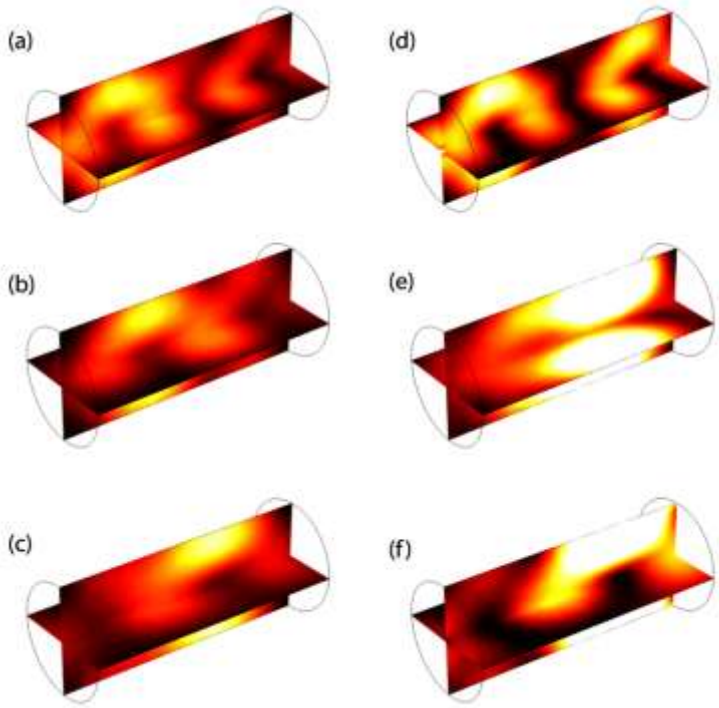


Figure 50: The absorption maps in the nanowire with (right) and without (left) nanoantenna elements at three different wavelengths (a,d) 550nm, (b,e) 600nm, (c,f) 650 nm.

### 3.4.2. Conclusion

Previously [182], we have studied the spectral properties of a nanoantenna array structure made from gold nanospheres and NWs. We found an optimum design for nanorod length and array spacing that can provide enhanced extinction. One of the main conclusions of that work was indicating how the plasmonic gold spheres lead to more absorption in the NWs due to localized surface plasmon resonances. Here, we have studied the role of dielectric elements used as nanoantenna elements and have found similar improvements. The increased absorption is due to the enhanced field intensity within the NW structure that is facilitated by the coupling properties of nanoantenna element. The advantage of using dielectric nanoantenna over plasmonic ones is the reduced material loss.

# CHAPTER 4: CONCLUDING REMARKS

## 4.1. Summary of the Dissertation

Thorough this dissertation, we have been focused on the use of sub-wavelength designs for efficient light-matter interaction in order to manipulate absorption and loss to our benefits, e.g. in applications such as telecom or photovoltaics. In addition, keeping in mind the possible properties of such artificial structures for new applications was a guide to look for exotic properties such as ENZ. We used plasmonic materials in the form of nanoparticles to excite the localized resonances and with that in hand we have been looking for the desired electromagnetic properties.

Most of the successful results have been published in the literature and also some of them are being considered for publication. As a summary, the list below enumerates the results of this work that are new:

1. Modeling the plasmonic response of AZO nanoparticles using equivalent circuit theory for a polarization insensitive low-loss structures at near infrared. This work is published in Journal of Nanophotonics (2014).
2. Bandwidth tuning of a dense gold nanoparticle system based on polarization of incident light at visible wavelength. This work is published in Applied Optics (2014).

3. Modeling and numerical study of optical absorption in composite arrays of Au-ZnTe nanoparticle-nanowire for finding optical length and spacing. This work is published in Photonics Research Journal (2014).
4. Investigation of optical response and radiation characteristics of single silicon nanowire attached to plasmonic gold nanoparticles with different geometries. This work is published in Applied Physics Letters (2014).
5. Study of enhanced absorption in arrays of nanowire and dielectric nanoantennas for solar cell applications. This work is being published in IEEE Xplore (2014).

## 4.2. Future Work

### 4.2.1. Hyperbolic Metamaterials

The metamaterial structures we have been working on by now can be classified as resonant systems. Working on or close to the resonance limits the control over optical properties or the resultant behavior of the system. Therefore, an approach having non-resonant design will be greatly beneficial. Regarding this, hyperbolic metamaterials (HMMs) have been suggested. As in our previous cases, it is also possible to model them with LCR circuits. Moreover, we have been working on optimization of such structures using Genetic Algorithm, which is a global optimization method for problems having many parameters in the design space. Fabrication of such HMMs have been also part of the activities of the group and in the near future the results will be released. The applications of the group have been on thermal management with HMMs.

### 4.2.2. Metasurfaces

Another very interesting category of metamaterials falls into the domain of surfaces. These exotic surfaces are called metasurfaces which can generalize the Snell's law for arbitrary refraction. The loss and absorption of such metasurfaces can also be investigated with the methods we used in this dissertation. In particular, we have suggested the use of metasurfaces for flat-optics elements as in free-form optics applications. Currently, generation of optical beam vortices is one of the main focuses of metasurfaces.

### 4.2.3. 3D Printing Devices

Based on what we investigated in the low-index low-loss section of this dissertation, it is possible to develop a plasmonic ink for use with high quality 3D printers such as Nanoscribe. With that in mind, the fabrication step is tremendously improved and one can rapidly prototype the devices based on plasmonic ink properties, specially the optical components in telecommunication industry can be 3D printed with the use of our AZO-plasmonic ink.

### 4.2.4. Polarization Splitter

One application which can be very interesting regarding the results of our polarization dependent bandwidth structures is the possible polarization splitting for digital signal processing. Currently, for some of the applications such as dispersion compensators in telecommunication networks, use of digital signal processing is the fastest and lowest cost method. However, they require methods of splitting the polarization and with the approach we studied the polarization dependence of bandwidth, it is possible to look for

solutions regarding a sub-wavelength polarization splitter that can be also integrated for photonic circuits.

#### 4.2.5. High Sensitive Broadband Sensors

For further developing the concept of our nanoantenna nanowire structure, one can employ the design method in order to extend the frequency domain of by a proper adjustment of plasmonic particles and shapes to cover more than just the solar spectrum. Thus, a broadband highly sensitive sensor, e.g. for infrared applications 2-10 μm, can be designed with high quantum efficiency that can be developed in low-light conditions as well. The nanoantenna structures can also be used in a segmented hyperspectral designs or also with combination of regular sensors in order to increase the light absorption onto the pixels. Furthermore, one can design three pixels of RGB and form a sub-wavelength color pixel for application in CCD cameras.

# REFERENCES

1- Veselago, V. G. "Electrodynamics of materials both permittivity and permeability being negative." *Uspekhi Fizicheskikh Nauk (in Russian)* 92, 7, 517-526 (1967).

2- Pendry, John B., A. J_ Holden, D. J. Robbins, and W. J. Stewart. "Magnetism from conductors and enhanced nonlinear phenomena." *Microwave Theory and Techniques, IEEE Transactions on* 47, 11, 2075-2084 (1999).

3- Smith, David R., Willie J. Padilla, D. C. Vier, Sc C. Nemat-Nasser, and Seldon Schultz. "Composite medium with simultaneously negative permeability and permittivity." *Physical Review Letters* 84, 18, 4184 (2000).

4-Shelby, Richard A., David R. Smith, and Seldon Schultz. "Experimental verification of a negative index of refraction." *Science* 292, 5514, 77-79 (2001).

5- Ritchie, R. H. "Plasma Losses by Fast Electrons in Thin Films" *Physical Review* 106, 5, 874–881 (1957).

6- Podolskiy, V. A., [Tutorials in Metamaterials], Vol. 1, CRC Press (2010).

7- Engheta, N., Salandrino, A., and Alu, A., "Circuit elements at optical frequencies: nanoinductors, nanocapacitors, and nanoresistors," *Physical Review Letters* 95, 9, 095504 (2005).

8- Alu, A. and Engheta, N., "Optical nanotransmission lines: synthesis of planar left-handed metamaterials in the infrared and visible regimes," *JOSA B* 23, 3, 571–583 (2006).

9- Smith, D., Schultz, S., Markos, P., and Soukoulis, C., "Determination of effective permittivity and permeability of metamaterials from reflection and transmission coefficients," *Physical Review B* 65, 19, 195104 (2002).

10- Smith, D. R., Vier, D., Koschny, T., and Soukoulis, C., "Electromagnetic parameter retrieval from inhomogeneous metamaterials," *Physical Review E* 71, 3, 036617 (2005).

11- Smith, D. R. and Pendry, J. B., "Homogenization of metamaterials by field averaging," *JOSA B* 23, 3, 391–403 (2006).

12- Andryieuski, A., Ha, S., Sukhorukov, A. A., Kivshar, Y. S., and Lavrinenko, A. V., "Bloch-mode analysis for retrieving effective parameters of metamaterials," *Physical Review B* 86, 3, 035127 (2012).

13- Fietz, C. and Shvets, G., "Current-driven metamaterial homogenization," *Physica B: Condensed Matter* 405, 14, 2930–2934 (2010).

14- Pendry, J. B., "Negative refraction makes a perfect lens," *Physical Review Letters* 85, 18, 3966–3969 (2000).

15- Shelby, R. A., Smith, D. R., and Schultz, S., "Experimental verification of a negative index of refraction," *Science* 292, 5514, 77–79 (2001).

16- Shalaev, V. M., "Optical negative-index metamaterials," *Nature Photonics* 1, 1, 41–48 (2007).

17- Smith, D., Pendry, J., and Wiltshire, M., "Metamaterials and negative refractive index," *Science* 305, 5685, 788–792 (2004).

18- Podolskiy, V. A. and Narimanov, E. E., "Near-sighted superlens," *Optics Letters* 30, 1, 75–77 (2005).

19- Jacob, Z., Alekseyev, L. V., and Narimanov, E., "Semiclassical theory of the hyperlens," *JOSA A* 24, 10, A52–A59 (2007).

20- Chen, H., Wu, B.-I., Zhang, B., and Kong, J. A., "Electromagnetic wave interactions with a metamaterials cloak," *Physical Review Letters* 99, 6, 063903 (2007).

21- Kundtz, N., Gaultney, D., and Smith, D. R., "Scattering cross-section of a transformation optics-based metamaterial cloak," *New Journal of Physics* 12, 4, 043039 (2010).

22- Ye, Y. and He, S., "90 polarization rotator using a bilayered chiral metamaterial with giant optical activity," *Applied Physics Letters* 96, 20, 203501–203501 (2010).

23- Plum, E., Zhou, J., Dong, J., Fedotov, V., Koschny, T., Soukoulis, C., and Zheludev, N., "Metamaterial with negative index due to chirality," *Physical Review B* 79, 3, 035407 (2009).

24- Ziolkowski, R. W., "Propagation in and scattering from a matched metamaterial having a zero index of refraction," *Physical Review E* 70, 4, 046608 (2004).

25- Xu, Y. and Chen, H., "Total reflection and transmission by epsilon-near-zero metamaterials with defects," *Applied Physics Letters* 98, 11, 113501–113501 (2011).

26- Silveirinha, M. and Engheta, N., "Tunneling of electromagnetic energy through subwavelength channels and bends using $\varepsilon$ -near-zero materials," *Physical Review Letters* 97, 15, 157403 (2006).

27- Alu, A., Silveirinha, M. G., Salandrino, A., and Engheta, N., "Epsilon-near-zero metamaterials and electromagnetic sources: Tailoring the radiation phase pattern," *Physical Review B* 75, 15, 155410 (2007).

28- Nguyen, V. C., Chen, L., and Halterman, K., "Total transmission and total reflection by zero index metamaterials with defects," *Physical Review Letters* 105, 23, 233908 (2010).

29- Massaouti, M., Basharin, A., Kafesaki, M., Acosta, M., Merino, R., Orera, V., Economou, E., Soukoulis, C., and Tzortzakis, S., "Eutectic epsilon-near-zero metamaterial terahertz waveguides," *Optics Letters* 38, 7, 1140–1142 (2013).

30- Maier, S. A., [Plasmonics: fundamentals and applications], Springer Science+ Business Media (2007).

31- Amendola, V., Bakr, O. M., and Stellacci, F., "A study of the surface plasmon resonance of silver nanoparticles by the discrete dipole approximation method: effect of shape, size, structure, and assembly," *Plasmonics* 5, 1, 85–97 (2010).

32- Johnson, P. B. and Christy, R., "Optical constants of the noble metals," *Physical Review B* 6, 12, 4370 (1972).

33- De Leon, I. and Berini, P., "Amplification of long-range surface plasmons by a dipolar gain medium," *Nature Photonics* 4, 6, 382–387 (2010).

34- West, P. R., Ishii, S., Naik, G. V., Emani, N. K., Shalaev, V. M., and Boltasseva, A., "Searching for better plasmonic materials," *Laser & Photonics Reviews* 4, 6, 795–808 (2010).

35- Naik, G. V. and Boltasseva, A., "A comparative study of semiconductor-based plasmonic metamaterials," *Metamaterials* 5, 1, 1–7 (2011).

36- Naik, G. V. and Boltasseva, A., "Semiconductors for Plasmonics and metamaterials," *Physica Status Solidi (RRL)-Rapid Research Letters* 4, 10, 295–297 (2010).

37- Naik, G. V., Kim, J., and Boltasseva, A., "Oxides and nitrides as alternative plasmonic materials in the optical range," *Optical Materials Express* 1, 6, 1090–1099 (2011).

38- Rhodes, C., Franzen, S., Maria, J.-P., Losego, M., Leonard, D. N., Laughlin, B., Duscher, G., and Weibel, S., "Surface plasmon resonance in conducting metal oxides," *Journal of Applied Physics* 100, 5, 054905–054905 (2006).

39- H. Alisafaee, P. M. Cox, and M. A. Fiddy, "Low-index metamaterials comprised of plasmonic dimers of aluminum-doped zinc oxide," *Proc. SPIE* 8806, 88061L (2013)

40- W. Cai and V. Shalaev, Optical Metamaterials: Fundamentals and Applications, Springer- Verlag, New York (2010).

41- Alu, A. and Engheta, N., “Optical metamaterials based on optical nanocircuits,” *Proceedings of IEEE* 99, 10, 1669–1681 (2011).

42- Salandrino, A., Alu, A., and Engheta, N., “Parallel, series, and intermediate interconnections of optical nanocircuit elements. 1. Analytical solution,” *JOSA B* 24, 12, 3007–3013 (2007).

43- Alu, A., Salandrino, A., and Engheta, N., “Parallel, series, and intermediate interconnections of optical nanocircuit elements. 2. nanocircuit and physical interpretation,” *JOSA B* 24, 12, 3014–3022 (2007).

44- Biagioni, P., Huang, J.-S., and Hecht, B., “Nanoantennas for visible and infrared radiation,” *Reports on Progress in Physics* 75, 2, 024402 (2012).

45- Alu, A., Salandrino, A., and Engheta, N., “Coupling of optical lumped nanocircuit elements and effects of substrates,” *Optics Express* 15, 21, 13865–13876 (2007).

46- Zuloaga, J., Prodan, E., and Nordlander, P., “Quantum description of the plasmon resonances of a nanoparticle dimer,” *Nano Letters* 9, 2, 887–891 (2009).

47- Yoo, S. and Park, Q.-H., “Effective permittivity for resonant plasmonic nanoparticle systems via dressed polarizability,” *Optics Express* 20, 15, 16480–16489 (2012).

48- D. Smith, J. Pendry, and M. Wiltshire, “Metamaterials and negative refractive index," *Science* 305,788-792 (2004).

49- V. M. Shalaev, “Optical negative-index metamaterials," *Nature Photonics* 1, 41-48 (2007).

50- J. B. Pendry, “Negative refraction makes a perfect lens," *Physical Review Letters* 85, 3966 (2000).

51- D. R. Smith, W. J. Padilla, D. Vier, S. C. Nemat-Nasser, and S. Schultz, “Composite medium with simultaneously negative permeability and permittivity," *Physical Review Letters* 84, 4184 (2000).

52- R. W. Ziolkowski and E. Heyman, “Wave propagation in media having negative permittivity and permeability," *Physical Review E* 64, 056625 (2001).

53- V. M. Shalaev, W. Cai, U. K. Chettiar, H.-K. Yuan,A. K. Sarychev, V. P. Drachev, and A. V. Kildishev, ”Negative index of refraction in optical metamaterials," *Optics Letters* 30, 3356-3358 (2005).

54- J. Cong, B. Yun, and Y. Cui, “Negative-index meta-material at visible frequencies based on high order plasmon resonance," *Appl. Opt.* 51, 2469-2476(2012).

55- H. Ma, S. Qu, Z. Xu, and J. Wang, “Using photon funnels based on metamaterial cloaks to compress electromagnetic wave beams," *Appl. Opt.* 47, 4193-4195 (2008).

56- I. Mohamed, G. Pisano, and M. W. Ng, “W-band pancharatnam half-wave plate based on negative refractive index metamaterials," *Appl. Opt.* 53, 2001-2006 (2014).

57- M. A. Escobar, M. Berthome, C. Ma, and Z. Liu, ”Focusing surface waves with an inhomogeneous metamaterial lens," *Appl. Opt.* 49, A18-A22 (2010).

58- X. Ling, H. Luo, C. Zhao, S. Wen, and D. Fan, ”Metamaterial-based polarization control plate for producing incoherent laser irradiation," *Appl. Opt.* 51, 4749-4753 (2012).

59- D. Schurig, J. Mock, B. Justice, S. A. Cummer, J. Pendry, A. Starr, and D. Smith, “Metamaterial electromagnetic cloak at microwave frequencies, " *Science* 314, 977-980 (2006).

60- B. Edwards, A. Alu, M. E. Young, M. Silveirinha, and N. Engheta, “Experimental verification of epsilon-near-zero metamaterial coupling and energy squeezing using a microwave waveguide," *Physical Review Letters* 100, 033903 (2008).

61- A. Alu, M. G. Silveirinha, A. Salandrino, and N. Engheta, “Epsilon-near-zero metamaterials and electromagnetic sources: Tailoring the radiation phase pattern," *Physical Review B* 75, 155410 (2007).

62- J. A. Fan, C. Wu, K. Bao, J. Bao, R. Bardhan, N. J. Halas, V. N. Manoharan, P. Nordlander,G. Shvets, and F. Capasso, “Self-assembled plasmonic nanoparticle clusters," *Science* 328, 1135-1138 (2010).

63- J. H. Lee, Q. Wu, and W. Park, “Metal nanocluster metamaterial fabricated by the colloidal self-assembly," *Optics Letters* 34, 443-445 (2009).

64- K. J. Stebe, E. Lewandowski, and M. Ghosh, “Oriented assembly of metamaterials," *Science* 325,159-160 (2009).

65- J. Fontana, J. Naciri, R. Rendell, and B. R. Ratna, ”Macroscopic self-assembly and optical characterization of nanoparticle-ligand metamaterials," *Advanced Optical Materials* 1, 100-106 (2013).

66- C. F. Bohren and D. R. Huffman, Absorption and scattering of light by small particles (John Wiley &Sons, 2008).

67- D. Smith, D. Vier, T. Koschny, and C. Soukoulis, ”Electromagnetic parameter retrieval from inhomogeneous metamaterials," *Physical Review E* 71,036617 (2005).

68- D. Smith, S. Schultz, P. Markos, and C. Soukoulis, ”Determination of effective permittivity and permeability of metamaterials from reflection and transmission coefficients," *Physical Review B* 65, 195104 (2002).

69- A. Efros, “Comment ii on resonant and antiresonant frequency dependence of the effective parameters of metamaterials," *Physical Review E* 70, 048602 (2004).

70- V. A. Markel, “Can the imaginary part of permeability be negative?" *Physical Review E* 78, 026608 (2008).

71- A. Alu, “Restoring the physical meaning of meta-material constitutive parameters," *Physical Review B* 83, 081102 (2011).

72- N. Engheta, “Circuits with light at nanoscales: optical nanocircuits inspired by metamaterials," *Science* 317, 1698-1702 (2007).

73- H. Alisafaee and M. A. Fiddy, “Polarization insensitivity in epsilon-near-zero metamaterial from plasmonic aluminum-doped zinc oxide nanoparticles," *Journal of Nanophotonics* 8, 083898 (2014).

74- P. B. Johnson and R. W. Christy, “Optical constants of the noble metals," *Phys. Rev. B* 6, 4370-4379 (1972).

75- S. Link and M. A. El-Sayed, “Spectral properties and relaxation dynamics of surface plasmon electronic oscillations in gold and silver nanodots and nanorods," *The Journal of Physical Chemistry B* 103, 8410-8426 (1999).

76- P. Stoller, V. Jacobsen, and V. Sandoghdar, “Measurement of the complex dielectric constant of a single gold nanoparticle," *Opt. Lett.* 31, 2474-2476 (2006).

77- K. Aydin, K. Guven, N. Katsarakis, C. Soukoulis, and E. Ozbay, “Effect of disorder on magnetic resonance band gap of split-ring resonator structures," *Opt. Express* 12, 5896-5901 (2004).

78- S. Wang, D. Ding, X. Liu, X.-B.Zhang, D.J. Smith, J.K. Furdyna, and Y.H. Zhang, “MBE growth of II-VI materials on GaSb substrates for photovoltaic applications,” *J Cryst Growth* 311, 2116-2119 (2009).

79-Y.-H.Zhang, S.-Q.Yu, S.R. Johnson, D. Ding, and S.-N.Wu, “A Proposal of Monolithically Integrated Multijunction Solar Cells using Lattice-matched II/VI and III/V Semiconductors,” *Proceedings of the 33rd IEEE Photovoltaic Energy Specialist Conference*, p. 20, (2008).

80-K. Sato, M. Hanafusa, A. Noda, A. Arakawa, M. Uchida, T. Asahi, and O. Oda, "ZnTe pure green light-emitting diodes fabricated by thermal diffusion," *J Cryst. Growth,* 214, 1080-1084 (2000).

81- Q. Zhang, J. Zhang, M.I.B. Utama, B. Peng, M. de la Mata, J. Arbiol, and Qihua Xiong, "Exciton-phonon coupling in individual ZnTe nanorods studied by resonant Raman spectroscopy," *Phys Rev B* 85, 085418 (2012).

82-Q. Wu, M. Litz, and X.-C.Zhang, "Broadband detection capability of ZnTe electro-optic field detectors," *Appl Phys Lett* 68, 2924-2926 (1996).

83-S. Valette, G. Labrunie, and J. Lizet, "Optical waveguides in ion-implanted ZnTe," *J Appl Phys* 46, 2731-2732 (1975).

84-Y. Kumagai, and M. Kobayashi, "Growth of ZnMgTe/ZnTe Waveguide Structure and Analysis of the Light Polarization with the Electric Field," *Jap J Appl Phys* 51, 2-6 (2012).

85-L.D. DeLoach, R.H. Page, G.D. Wilke, S.A. Payne, and W.F. Krupke, "Transition Metal-Doped Zinc Chalcogenides: Spectroscopy and Laser Determination of a New Class of Gain Media," *IEEE J Quant Elec* 32, 885-895 (1996).

86-F.A. Majumder, C. Klingshirn, R. Westphäling, H. Kalt, A. Naumov, H. Stanzi, and W. Gebhardt, "Grain Processes in ZnTe Epilayers on GaAs," *Physica Stat Sol (b)* 186, 591-599 (1994).

87- M.S. Litz, D.C. Judy, and N. Tesny, "A ZnTe Electro-Optic Electric Field Sensor," *SPIE Conference on Intense Microwave Pulses* VI3702, 30-35 (1999).

88- H.H. Li, "Refractive Index of ZnS, ZnSe, ZnTe and Its Wavelength and Temperature Derivatives," *J Phys Chem Ref Data* 13, 103-150 (1984).

89- W.I. Wang, "The Problem of Doping Wide Gap II-VI Compound Semiconductors and Its Solutions," MRS Proceedings228, 319 (1991).

90- U.V. Desnica, "Doping Limits in II-VI Compunds – Challenges, Problems and Solutions," *Prog Cryst Growth Charact* 36, 291-357 (1998).

91-Y. Zhang, L.-W.Wang, and A.Mascarenhas, "Quantum coaxial cables for solar energy harvesting", *Nano Lett* 7, 1204-1269 (2007).

92- M.M. Adachi, M.P. Anantram, and K.S. Karim, "Core-shell silicon nanowire solar cells," *Scientific Reports* 3, 1-6 (2013).

93- Z. Li, J. Wang, N. Singh, and S. Lee, “Optical and electrical study of core-shell silicon nanowires for solar applications,” *Optics Express* 19, A1057-A1066 (2011).

94- Y. Cao, Z. Wu, J. Ni, W.A. Bhutto, J. Li, S. Li, K. Huang, and J. Kang, “Type-II Core/Shell Nanowire Heterostructures and Their Photovoltaic Applications,” *Nano-Micro Lett* 4, 135-141 (2012).

95- R.S. Wagner, and W.C. Ellis, “Vapor-liquid-solid Mechanism of Single Crystal Growth,” *Appl Phys Lett* 4,89-90 (1964).

96- K.L. Kelly, E. Coronado, L. Zhao, and G. C. Schatz. "The optical properties of metal nanoparticles: the influence of size, shape, and dielectric environment." *The Journal of Physical Chemistry B* 107, 668-677 (2003)

97- Maier, Stefan A., ed. Plasmonics: fundamentals and applications. Springer, 2007.

98- P.J. Flatau, B. T. Draine. "Discrete-dipole approximation for scattering calculations." *J. Opt. Soc. Am. A* 11, 1491 (1994)

99- A. Alú, A. Salandrino, and N. Engheta, "Coupling of optical lumped nanocircuit elements and effects of substrates," *Opt. Express* 15, 13865-13876 (2007).

100- C. Huang, X. Yin, H. Huang, and Y. Zhu, "Study of plasmon resonance in a gold nanorod with an LC circuit model," *Opt. Express* 17, 6407-6413 (2009).

101- P.B. Johnson, R.W. Christy. "Optical constants of the noble metals." *Physical Review B* 6, 12, 4370 (1972)

102- U. Kreibig and M. Vollmer, “Optical properties of metal clusters,” 1995.

103- J. Z. Zhang and C. Noguez, “Plasmonic optical properties and applications of metal nanostructures,” *Plasmonics* 3, 4, 127–150 (2008).

104- K. L. Kelly, E. Coronado, L. L. Zhao, and G. C. Schatz, “The optical properties of metal nanoparticles: the influence of size, shape, and dielectric environment,” *The Journal of Physical Chemistry B* 107, 3, 668–677 (2003).

105- N. Fang, H. Lee, C. Sun, and X. Zhang, “Sub–diffraction-limited optical imaging with a silver superlens,” *Science* 308, 5721, 534–537 (2005).

106- N. Engheta, “Circuits with light at nanoscales: optical nanocircuits inspired by metamaterials,” *Science* 317, 5845, 1698–1702 (2007).

107- S. A. Maier, M. L. Brongersma, P. G. Kik, S. Meltzer, A. A. Requicha, and H. A. Atwater, “Plasmonics a route to nanoscale optical devices,” *Advanced Materials* 13, 19, 1501–1505 (2001).

108- J. B. Pendry, A. J. Holden, D. Robbins, and W. Stewart, "Magnetism from conductors and enhanced nonlinear phenomena," *Microwave Theory and Techniques, IEEE Transactions on* 47, 11, 2075–2084 (1999).

109- V. M. Shalaev, "Optical negative-index metamaterials," *Nature Photonics* 1(1), 41–48 (2007).

110- J. Hao, J. Wang, X. Liu, W. J. Padilla, L. Zhou, and M. Qiu, "High performance optical absorber based on a plasmonic metamaterial," *Applied Physics Letters* 96, 25, 251104–251104 (2010).

111- P. Genevet, N. Yu, F. Aieta, J. Lin, M. A. Kats, R. Blanchard, M. O. Scully, Z. Gaburro, and F. Capasso,"Ultra-thin plasmonic optical vortex plate based on phase discontinuities," *Applied Physics Letters* 100, 1, 013101–013101 (2012).

112- N. Liu, L. Langguth, T. Weiss, J. Kastel, M. Fleischhauer, T. Pfau, and H. Giessen, "Plasmonic analogue of electromagnetically induced transparency at the Drude damping limit," *Nature Materials* 8, 9, 758–762 (2009).

113- N. Liu, T. Weiss, M. Mesch, L. Langguth, U. Eigenthaler, M. Hirscher, C. Sonnichsen, and H. Giessen, "Planar metamaterial analogue of electromagnetically induced transparency for plasmonic sensing," *Nano Letters* 10, 4, 1103–1107 (2009).

114- K. A. Willets and R. P. Van Duyne, "Localized surface plasmon resonance spectroscopy and sensing," *Annu.Rev. Phys. Chem.* 58, 267–297 (2007).

115- A. Otto, I. Mrozek, H. Grabhorn, and W. Akemann, "Surface-enhanced Raman scattering," *Journal of Physics: Condensed Matter* 4, 5, 1143 (1992).

116- K. Catchpole, A. Polman, *et al.*, "Plasmonic solar cells," *Opt. Express* 16, 26, 21793–21800 (2008).

117- K. Nakayama, K. Tanabe, and H. A. Atwater, "Plasmonic nanoparticle enhanced light absorption in GaAs solar cells," *Applied Physics Letters* 93, 12, 121904–121904, (2008).

118- A. J. Morfa, K. L. Rowlen, T. H. Reilly, M. J. Romero, and J. van de Lagemaat, "Plasmon-enhanced solar energy conversion in organic bulk heterojunction photovoltaics," *Applied Physics Letters* 92, 1, 013504–013504, (2008).

119- S.-S. Kim, S.-I.Na, J. Jo, D.-Y.Kim, and Y.-C. Nah, "Plasmon enhanced performance of organic solar cells using electrodeposited Ag nanoparticles," *Applied Physics Letters* 93, 073307 (2008).

120- H. R. Stuart and D. G. Hall, “Absorption enhancement in silicon-on-insulator waveguides using metal island films,” *Applied Physics Letters* 69, 16, 2327–2329 (1996).

121- H. R. Stuart and D. G. Hall, “Island size effects in nanoparticle-enhanced photodetectors,” *Applied Physics Letters* 73, 26, 3815–3817 (1998).

122- H. A. Atwater and A. Polman, “Plasmonics for improved photovoltaic devices,” *Nature Materials* 9, 3, 205–213, (2010).

123- V. E. Ferry, J. N.Munday, and H. A. Atwater, “Design considerations for plasmonic photovoltaics,” *Advanced Materials* 22, 43, 4794–4808 (2010).

124- I.M. Pryce, D. D. Koleske, A. J. Fischer, and H. A. Atwater, “Plasmonic nanoparticle enhanced photocurrentin Gan/InGan/Gan quantum well solar cells,” *Applied Physics Letters* 96, 15, 153501–153501 (2010).

125- P. Spinelli, V. Ferry, J. Van de Groep, M. Van Lare, M. Verschuuren, R. Schropp, H. Atwater, and A. Polman, “Plasmonic light trapping in thin-film Si solar cells,” *Journal of Optics* 14, 2, 024002 (2012).

126- V. E. Ferry, M. A. Verschuuren, H. B. Li, E. Verhagen, R. J. Walters, R. E. Schropp, H. A. Atwater, and A. Polman, “Light trapping in ultrathin plasmonic solar cells,” *Optics Express* 18, S2, A237–A245 (2010).

127- M. D. Kelzenberg, D. B. Turner-Evans, M. C. Putnam, S. W. Boettcher, R. M. Briggs, J. Y. Baek, N. S.Lewis, and H. A. Atwater, “High-performance Si microwire photovoltaics,” *Energy & Environmental Science* 4, 3, 866–871 (2011).

128- S. Hu, C.-Y. Chi, K. T. Fountaine, M. Yao, H. A. Atwater, P. D. Dapkus, N. S. Lewis, and C. Zhou, “Optical, electrical, and solar energy-conversion properties of gallium arsenide nanowire-array photoanodes,” *Energy & Environmental Science* 6, 6, 1879-1890 (2013).

129- A. Dalmau Mallorqu´ı, F. Epple, D. Fan, O. Demichel, and A. Fontcuberta i Morral, “Effect of the PN junction engineering on Si microwire-array solar cells,” *physica status solidi (a)* 209, 8, 1588–1591 (2012).

130- D. R. Kim, C. H. Lee, P. M. Rao, I. S. Cho, and X. Zheng, “Hybrid Si microwire and planar solar cells: passivation and characterization,” *Nano Letters* 11, 7, 2704–2708 (2011).

131- P. Corfdir, B. Van Hattem, E. Uccelli, A. Fontcuberta i Morral, and R. Phillips, “Charge carrier generation, relaxation, and recombination in polytypic GaAs nanowires studied by photoluminescence excitation spectroscopy,” *Applied Physics Letters* 103, 13, 133109–133109 (2013).

132- E. Uccelli, J. Arbiol, C. Magen, P. Krogstrup, E. Russo-Averchi, M. Heiss, G. Mugny, F. Morier-Genoud,J. Nygard, J. R. Morante, *et al.*, "Three-dimensional multiple-order twinning of self-catalyzed GaAs nanowires on Si substrates," *Nano Letters* 11, 9, 3827–3832 (2011).

133- M. Heiss, C. Colombo, and A. F. i Morral, "Nanowire based heterostructures: fundamental properties and applications," in *SPIE NanoScience+ Engineering*, 810603–810603 (2011).

134- R. Wagner and W. Ellis, "Vapor-liquid-solid mechanism of single crystal growth," *Applied Physics Letters* 4, 5, 89–90 (1964).

135- A. Morral, "Gold-free GaAs nanowire synthesis and optical properties," *Selected Topics in Quantum Electronics, IEEE Journal of* 17, 4, 819–828,= (2011).

136- P. Krogstrup, H. I. Jørgensen, M. Heiss, O. Demichel, J. V. Holm, M. Aagesen, J. Nygard, and A. F.i Morral, "Single-nanowire solar cells beyond the Shockley-Queisser limit," *Nature Photonics* 7, 306-310 (2013).

137- H. Alisafaee, J. Marmon, and M. Fiddy, "Spectral properties of Au–ZnTe plasmonic nanorods," *Photonics Research* 2, 1, 10–14 (2014).

138- J. Z. Zhang and C. Noguez, "Plasmonic Optical Properties and Applications of Metal Nanostructures" *Plasmonics* 3, 4, 127-150 (2008).

139- K. L. Kelly, E. Coronado, L. L. Zhao, and G. C. Schatz, "The Optical Properties of Metal Nanoparticles: The Influence of Size, Shape, and Dielectric Environment" *J. Phys. Chem. B* 107, 668 (2003).

140- N. Engheta, "Circuits with light at nanoscales: optical nanocircuits inspired by metamaterials" *Science* 317, 1698 (2007).

141-P. Genevet, N. Yu, F. Aieta, J. Lin, M. A. Kats, R. Blanchard, M. O.Scully, Z. Gaburro, and F. Capasso, "Ultra-thin plasmonic optical vortex plate based on phase discontinuities" *Appl. Phys. Lett.* 100, 013101 (2012).

142- N. Fang, H. Lee, C. Sun, and X. Zhang, "Sub–diffraction-limited optical imaging with a silver superlens" *Science* 308, 534 (2005).

143- J. Hao, J. Wang, X. Liu, W. J. Padilla, L. Zhou, and M. Qiu, "High performance optical absorber based on a plasmonic metamaterial" *Appl. Phys. Lett.* 96, 251104 (2010).

144- V. M. Shalaev, "Optical negative-index metamaterials" *Nat. Photonics* 1, 41 (2007).

145- N. Liu, L. Langguth, T. Weiss, J. Kastel, M. Fleischhauer, T. Pfau, and H. Giessen, "Plasmonic analogue of electromagnetically induced transparency at the Drude damping limit." *Nat. Mater.* 8, 758 (2009).

146- A. Otto, I. Mrozek, H. Grabhorn, and W. Akemann, "Surface-enhanced Raman scattering" *J. Phys.: Condens. Matter* 4, 1143 (1992).

147- A. J. Morfa, K. L. Rowlen, T. H. Reilly, M. J. Romero, and J. van de Lagemaat, "Plasmon-enhanced solar energy conversion in organic bulk heterojunction photovoltaics" *Appl. Phys. Lett.* 92, 013504 (2008).

148- K. Nakayama, K. Tanabe, and H. A. Atwater, "Plasmonic nanoparticle enhanced light absorption in GaAs solar cells." *Appl. Phys. Lett.* 93,121904 (2008).

149- K. Catchpole and A. Polman, "Plasmonic solar cells" *Opt. Express* 16, 21793 (2008).

150- S.-S. Kim, S.-I. Na, J. Jo, D.-Y. Kim, and Y.-C. Nah, "Plasmon enhanced performance of organic solar cells using electrodeposited Ag nanoparticles" *Appl. Phys. Lett*. 93, 073307 (2008).

151- H. R. Stuart and D. G. Hall, "Absorption enhancement in silicon-on-insulator waveguides using metal island films" *Appl. Phys. Lett. 69*, 2327 (1996).

152- H. A. Atwater and A. Polman, "Plasmonics for improved photovoltaic devices" *Nat. Mater.* 9, 205 (2010).

153- I. M. Pryce, D. D. Koleske, A. J. Fischer, and H. A. Atwater, "Plasmonic nanoparticle enhanced photocurrent in GaN/InGaN/GaN quantum well solar cells" *Appl. Phys. Lett.* 96, 153501 (2010).

154- V. E. Ferry, J. N. Munday, and H. A. Atwater, "Design considerations for plasmonic photovoltaics" *Adv. Mater.* 22, 4794 (2010).

155- V. E. Ferry, M. A. Verschuuren, H. B. Li, E. Verhagen, R. J. Walters, R. E. Schropp, H. A. Atwater, and A. Polman, "Light trapping in ultrathin plasmonic solar cells" *Opt. Express* 18, A237 (2010).

156-M. D. Kelzenberg, D. B. Turner-Evans, M. C. Putnam, S. W. Boettcher, R. M. Briggs, J. Y. Baek, N. S. Lewis, and H. A. Atwater, "High-performance Si microwire photovoltaics" *Energy Environ. Sci.* 4, 866 (2011).

157- S. Hu, C.-Y. Chi, K. T. Fountaine, M. Yao, H. A. Atwater, P. D. Dapkus, N. S. Lewis, and C. Zhou, "Optical, electrical, and solar energy-conversion properties of gallium arsenide nanowire-array photoanodes" *Energy Environ. Sci.* 6, 1879 (2013).

158- P. Corfdir, B. Van Hattem, E. Uccelli, A. Fontcuberta i Morral, and R. Phillips, "Charge carrier generation, relaxation, and recombination in polytypic GaAs nanowires studied by photoluminescence excitation spectroscopy" *Appl. Phys. Lett.* 103, 133109 (2013).

159- D. R. Kim, C. H. Lee, P. M. Rao, I. S. Cho, and X. Zheng, "Hybrid Si microwire and planar solar cells: passivation and characterization" *Nano Lett.* 11, 2704 (2011).

160- A. Dalmau Mallorqui, F. Epple, D. Fan, O. Demichel, and A. Fontcuberta i Morral, "Effect of the pn junction engineering on Si microwire-array solar cells" *Phys. Status Solidi A* 209, 1588 (2012).

161- P. Krogstrup, H. I. Jørgensen, M. Heiss, O. Demichel, J. V. Holm, M. Aagesen, J. Nygard, and A. F. i Morral, "Single-nanowire solar cells beyond the Shockley-Queisser limit" Nat. Photonics 7, 306-310 (2013).

162- A. Krasnok, C. Simovski, P. Belov, and Y. S. Kivshar, "Superdirective dielectric nanoantennas" Nanoscale 6, 7354 (2014).

163- S. Steshenko and F. Capolino, Single Dipole Approximation for Modeling Collections of Nanoscatterers (CRC Press, 2009), Vol. 8.

164- J. R. Cole and N. J. Halas, "Optimized plasmonic nanoparticle distributions for solar spectrum harvesting" *Appl. Phys. Lett.* 89, 153120 (2006).

165- H. Alisafaee, J. Marmon, and M. A. Fiddy, "Spectral properties of Au–ZnTe plasmonic nanorods" *Photon. Res. J.* 2, 10 (2014).

166- C. Lin and M. L. Povinelli, "The effect of plasmonic particles on solar absorption in vertically aligned silicon nanowire arrays" *Appl. Phys. Lett.* 97, 071110 (2010).

167- S. Brittman, H. Gao, E. C. Garnett, and P. Yang, "Absorption of light in a single-nanowire silicon solar cell decorated with an octahedral silver nanocrystal" *Nano Lett.* 11, 5189 (2011).

168- S. Mokkapati, D. Saxena, N. Jiang, P. Parkinson, J. Wong-Leung, Q. Gao,H. H. Tan, and C. Jagadish, "Polarization tunable, multicolor emission from core–shell photonic III–V semiconductor nanowires" *Nano Lett.* 12, 6428 (2012).

169- R. Wagner and W. Ellis, "Vapor-Liquid-Solid mechanism of single crystal growth" *Appl. Phys. Lett.* 4, 89 (1964).

170- A. Morral, "Gold-Free GaAs Nanowire Syn- thesis and Optical Properties" *IEEE J. Sel. Top. Quantum Electron.* 17, 819 (2011).

171- Atwater, Harry A., and Albert Polman. "Plasmonics for improved photovoltaic devices." *Nature Materials* 9, 3, 205-213 (2010).

172- Kelzenberg, Michael D., Shannon W. Boettcher, Jan A. Petykiewicz, Daniel B. Turner-Evans, Morgan C. Putnam, Emily L. Warren, Joshua M. Spurgeon, Ryan M. Briggs, Nathan S. Lewis, and Harry A. Atwater. "Enhanced absorption and carrier collection in Si wire arrays for photovoltaic applications." *Nature Materials* 9, 3, 239-244 (2010).

173- Ferry, Vivian E., Jeremy N. Munday, and Harry A. Atwater. "Design considerations for plasmonic photovoltaics." *Advanced Materials* 22, 43, 4794-4808 (2010).

174- Polman, Albert, and Harry A. Atwater. "Photonic design principles for ultrahigh-efficiency photovoltaics." *Nature Materials* 11, 3, 174-177 (2012).

175- Ferry, Vivian E., Marc A. Verschuuren, Hongbo BT Li, Ewold Verhagen, Robert J. Walters, Ruud EI Schropp, Harry A. Atwater, and Albert Polman. "Light trapping in ultrathin plasmonic solar cells." *Optics Express* 18, 102, A237-A245 (2010).

176- Warren, Emily L., Harry A. Atwater, and Nathan S. Lewis. "Silicon Microwire Arrays for Solar Energy-Conversion Applications." *The Journal of Physical Chemistry C* 118, 2, 747-759 (2013).

177- Kim, Jin Young, Kwanghee Lee, Nelson E. Coates, Daniel Moses, Thuc-Quyen Nguyen, Mark Dante, and Alan J. Heeger. "Efficient tandem polymer solar cells fabricated by all-solution processing." *Science* 317, 5835, 222-225 (2007).

178- Kelzenberg, Michael D., Daniel B. Turner-Evans, Morgan C. Putnam, Shannon W. Boettcher, Ryan M. Briggs, Jae Yeon Baek, Nathan S. Lewis, and Harry A. Atwater. "High-performance Si microwire photovoltaics." *Energy & Environmental Science* 4, 3, 866-871 (2011).

179- Law, Matt, Lori E. Greene, Justin C. Johnson, Richard Saykally, and Peidong Yang. "Nanowire dye-sensitized solar cells." Nature Materials 4, 6, 455-459 (2005).

180- Maier, Stefan Alexander. Plasmonics: Fundamentals and Applications: Fundamentals and Applications. Springer, 2007.

181- Bohren, Craig F., and Donald R. Huffman. Absorption and scattering of light by small particles. John Wiley & Sons, 2008.

182- Alisafaee, H., J. Marmon, and M. A. Fiddy. "Spectral properties of Au–ZnTe plasmonic nanorods." Photonics Research 2, 1, 10-14 (2014).

Publications: Journal Papers

1. **H.Alisafaee**, M.A.Fiddy "Nanoantennas for Nanowire Photovoltaics" *Appl. Phys. Lett.* 105, 113107 (2014)
2. **H.Alisafaee**, J.Marmon, M.A.Fiddy, "Spectral properties of Au–ZnTe plasmonic nanorods" *Photonics Research Journal*, 2, 1, 10-14 (2014)
3. **H.Alisafaee**, M.A.Fiddy, "Hybrid Optical Nanoantennas", in preparation for *Physical Review Letters (2014)*.
4. **H.Alisafaee**, M.A.Fiddy, "Polarization insensitivity in epsilon-near-zero metamaterial from plasmonic aluminum-doped zinc oxide nanoparticles*"* *Journal of Nanophotonics*, 8, 1, 083898 (2014)
5. **H.Alisafaee**, M.A.Fiddy, "Polarization dependent bandwidth in low-index plasmonic metamaterials", (under revise), *Applied Optics (2014).*
6. **H.Alisafaee**, M.A.Fiddy, "Photovoltaics with Dielectric Nanoantennas" Submitted to *IEEE Xplore (2014)*.
7. J. S. D. Roberts, **H.Alisafaee**, M.A. Fiddy, "Selective field localization in random structured media" *Applied Optics*, 52, 4, (2013) 742-9

Conference Papers

1. **H.Alisafaee**, M.A.Fiddy, "Absorption and Scattering Efficiency of Core/Shell Plasmonic Nanowire Structures", (invited) META14 conf., Singapore (20-23 May 2014)
2. I.A.Goforth, **H.Alisafaee**, D.B.Fullager, C.Rosenbury, M.A. Fiddy, "Design of hyperbolic metamaterials by genetic algorithm" SPIE O+P, 2014

3. M.A.Fiddy, **H.Alisafaee**, R.Tsu, “Designing low index metamaterials and the random phase”, The ICEAA - IEEE APWC (2014)
4. **H.Alisafaee**, M.A.Fiddy, “Dedicated Nanoantenna Element for Vertical Nanorods in Photovoltaics” SPIE Photonics West, San Francisco, CA (2014)
5. **H.Alisafaee**, D.B.Fullager, M.A.Fiddy, “ENZ waveguide of Al-doped ZnO for Telecom Applications” SPIE Photonics West, San Francisco, CA (1-6 Feb 2014)
6. **H.Alisafaee**, D.B.Fullager, M.A.Fiddy, “Tuning of low-index bandwidth in metamaterials”, Frontier in Optics, Orlando, FL (6-10 October 2013)(Oral)
7. M.A.Fiddy, D.Fullager, **H.Alisafaee**, "Fundamentals of Engineering Plasmonic Optical Materials", Workshop Optical Plasmonic Materials, Berlin, Germany (19/3/2014)
8. **H.Alisafaee**, P. M. Cox, M.A. Fiddy, “Low-index metamaterials comprised of plasmonic dimers of aluminum doped zinc oxide”, Proc. SPIE 8806, Metamaterials: Fundamentals and Applications VI, 88061L (Sep. 11, 2013)
9. D.Fullager, **H.Alisafaee**, M.A.Fiddy, “Epitaxial thin films for hyperbolic metamaterials” Accepted in OPTO conference at SPIE Photonics West, San Francisco, CA (1-6 Feb 2014)
10. **H.Alisafaee**, J.Marmon, M.A.Fiddy, “Spectral Properties of Au-ZnTe Plasmonic Nanorods”, ICNP/AOM, Hong Kong, China (19-23 May 2013)

Patents

**H.Alisafaee**, M.A.Fiddy, U. S. Patent Pending #61/736,178 (12/12/12)

**H.Alisafaee**, M.A.Fiddy, U. S. Patent application #61/843,123 (7/5/13)

**H.Alisafaee**, M.A.Fiddy, U. S. Patent application #61/868,714 (8/22/13)